

## 5. RESEARCH ACTIVITIES

### 5.1 NUCLEAR PHYSICS

During 2010, the recently commissioned neutron detector array (NAND) combined with the augmented energy from the LINAC has been extensively used for reaction dynamics studies. There was a major emphasis on studying the role of nuclear shell closure on fusion-fission dynamics. It has been observed that the system  $^{19}\text{F}+^{194}\text{Pt}$  with  $N_c=126$  has significantly lower pre-scission neutron multiplicity compared to other platinum isotopes. Similar reduction at neutron shell closure has also been observed in the neutron multiplicity for  $^{16,18}\text{O} + \text{Pt}$  and  $^{12}\text{C} + \text{Pt}$  systems. Simultaneous measurements of fission fragment mass distribution, evaporation residue excitation function and ER-gated CN angular momentum ( $J$ ) distribution for  $^{19}\text{F}+^{184}\text{W}$  indicates the onset of instability in the CN ( $^{203}_{83}\text{Bi}$ ) after crossing of the  $Z = 82$  shell.

In a multi-institutional collaborative project, the  $4\pi$  Spin Spectrometer from TIFR has been installed at the HYRA beam line at IUAC in order to carry out a series of experiments for the study of  $\gamma$ -multiplicity distribution. Exclusive measurement of GDR decay from hot excited  $^{196}\text{Hg}$  has been carried out using this facility. For the system  $^{30}\text{Si} + ^{170}\text{Er}$ , the measured  $\gamma$ -multiplicity distribution shows saturation effects at higher entrance channel angular momenta.

Evaporation residue yields from incomplete fusion processes have been measured for  $^{12}\text{C}$  and  $^{14}\text{N}$  induced reactions. Comparison with earlier work with  $^{16}\text{O}$  projectiles indicates a progressive increase in reaction yield for heavier projectiles at the same relative velocity. From a comparison of a large number of projectile-target combinations, it is inferred that the Morgenstern's systematics for incomplete fusion yields as a function of entrance channel mass asymmetry does not explain the observed yields for different projectiles as a whole.

The first series of experiments with the Indian National Gamma Array (INGA), set up at IUAC in 2008, have come to an end and the detectors shifted to TIFR. The results from some of the work carried out earlier are presented in this year's report.

In an interesting experiment, neutrons from the bombardment of 50 keV deuterons on CaO-Pd-CaO multilayer samples were measured by four large area NE213 neutron detectors. There is an indication of high energy neutrons, (i.e. 2.45 MeV neutrons expected from d+d reaction) produced during the irradiation.

### 5.1.1 Role of shell closure on nuclear dissipation using neutron as a probe

Varinderjit Singh<sup>1</sup>, B.R. Behera<sup>1</sup>, D.Siwal<sup>2</sup>, Maninder Kaur<sup>1</sup>, S.Goyal<sup>2</sup>, P. Sugathan,  
K.S. Golda<sup>3</sup>, A. Jhingan<sup>3</sup>, A.Kumar<sup>1</sup>, A. Saxena<sup>4</sup>, R.K. Bhowmik<sup>3</sup>, S. Kailas<sup>4</sup>

<sup>1</sup>Department of Physics, Panjab University, Chandigarh

<sup>2</sup>Department of Physics and Astrophysics, University of Delhi

<sup>3</sup>Inter University Accelerator Centre, Aruna Asaf Ali Marg, New Delhi

<sup>4</sup>Nuclear Physics Division, Bhabha Atomic Research Centre, Mumbai

In the last century, the development of nuclear accelerator for the production of heavy ion beams opened an opportunity to study the heavy-ion induced fusion-fission reactions. The importance of dissipation in fusion-fission dynamics is well established from the study of light particle emission during heavy-ion induced fusion-fission reaction. Experimental signature of large dissipation is observed through large excess in pre-fission neutrons, gamma ray multiplicities from compound nucleus giant dipole resonance (GDR), light charged particles and evaporation residue [1]. Mainly, dissipation is observed at nuclear temperature between 1 and 2 MeV. It is also found that dissipation effect increases with excitation energy.

In the current scenario, one of the major objectives of nuclear reaction study is to explore the predicted Island of Super-Heavy elements and to find what will be the next Proton and Neutron magic nucleus beyond 82 and 126 respectively. However, different theoretical models predict proton and neutron shell closure at  $Z = 114, 120, 122, 124, 126$  and  $N = 172, 184$ .

Back *et al.* [2] have reported that in order to reproduce evaporation residue cross-sections for  $^{224}\text{Th}$  and  $^{216}\text{Th}$  nuclei, a larger dissipation strength was required for  $^{224}\text{Th}$ . It was concluded that nuclear dissipation has possible relation with neutron closed shell  $N_c=126$ . To explore the effect of shell closure on nuclear dissipation, we have decided to perform a simultaneous analysis of neutron multiplicity, fission cross-section and evaporation residue cross-section for  $^{19}\text{F}+^{194,196,198}\text{Pt}$  resulting in formation of CN  $^{213}\text{Fr}$  ( $N_c=126$ ),  $^{215}\text{Fr}$  ( $N_c=128$ ) and  $^{217}\text{Fr}$  ( $N_c=130$ ) systems. Here we are presenting the results of neutron multiplicity measurement for reactions of  $^{19}\text{F} + ^{194,196,198}\text{Pt}$  at excitation energy range 52-67.5 MeV.

The experiment was performed using 15UD pelletron and National array of Neutron Detectors (NAND) at IUAC, New Delhi. Pulsed beam  $^{19}\text{F}$  (Energy Range = 98 – 115 MeV) at repetition rate of 250 ns with pulse width of 1.1 ns, was bombarded on targets of  $^{194}\text{Pt}$ ,  $^{196}\text{Pt}$  and  $^{198}\text{Pt}$  of thickness 1.75 mg/cm<sup>2</sup>, 1.8mg/cm<sup>2</sup> and 2.15 mg/cm<sup>2</sup> respectively. Targets were located at the centre of a thin walled spherical scattering

chamber of 60 cm diameter. Fission fragments were detected by a pair of Multi-wire proportional counter (MWPC) (5" x 3") kept at fission fragment folding angle at distance of 17.7 cm and 17.0 cm from target position. Two silicon surface barrier detectors were also placed inside the chamber at  $\pm 16^\circ$  to beam direction out of reaction plane for the normalization purpose.

Out of 16 Neutron detectors (5" x 5"), 12 were kept at 2 meter distance and remaining 4 were kept at 1 meter distance from the target. These detectors were placed at different angles ranging from  $30^\circ$  to  $315^\circ$  around the target chamber in reaction plane. Hardware threshold of 0.5 MeV of neutron energy was applied using  $^{137}\text{Cs}$  and  $^{60}\text{Co}$  sources. In order to reduce gamma background beam dump was extended 3m downstream from target and beam line was shielded with paraffin and lead bricks.

The trigger of data acquisition was generated by Logical OR of cathode signal of the two MWPC gated with the RF of the beam pulse. Neutron gamma discrimination was done using IUAC made Pulse Shape Discrimination module.

In the analysis it was assumed that neutrons detected in coincidence with fission fragments were originated from three moving sources compound nucleus evaporation (pre-scission) and fission fragments (post-scission). The compound nucleus contribution (pre-scission) and contribution from fission fragments (post-scission) were assumed to be isotropic. Further, post-scission neutron multiplicity and temperatures are assumed to be same for both fragments. Hence the total neutron multiplicity  $M_{\text{total}} = M_{\text{pre}} + 2 * M_{\text{post}}$ . The raw neutron TOF spectra are converted to energy spectra for all 16 in plane detectors. Data has been corrected for efficiency of neutron detectors. This efficiency was measured using  $^{252}\text{Cf}$  source. In order to obtain pre-scission and post-scission contributions spectra of 16 detectors are fitted simultaneously for 32 different neutron-fission angle ( $\Phi_{\text{nf}}$ ) combinations, using watt expression:

$$Y(E_n) = \sum_{i=1}^3 \frac{M_n^i \sqrt{E_n}}{2(\pi T_i)^{3/2}} \times \exp\left[-\frac{(E_n - 2\sqrt{\varepsilon_i E_n} \cos \Phi_i + \varepsilon_i)}{T_i}\right]$$

where  $\varepsilon_j$ ,  $T_j$  and  $M_n^j$  are energy per nucleon, temperature and multiplicity of neutron source  $i$ .  $E_n$  is lab energy of neutrons and  $\phi_j$  is neutron detection angle with respect to source  $i$ . Neutron multiplicities obtained from fitting for decay of  $^{217}\text{Fr}$ ,  $^{215}\text{Fr}$  and  $^{213}\text{Fr}$  are given and fitting plots are shown in figure 1.

Statistical model calculation PACE2 was performed with a value of parameters obtained by fitting the measured fission and ER cross sections [3]. At the lowest excitation energy (52 MeV) PACE2 calculation could reproduce the experimental results for pre-scission neutron multiplicity. However, at higher excitation energy the measured neutron

multiplicity values deviate considerably from the calculation. This is precisely due to the fact that delay is not included in the PACE2 calculation. However the deviation for the system  $^{19}\text{F}+^{194}\text{Pt}$  is much less compared to other two systems. It may be perhaps due to the presence of neutron shell closure ( $N_c=126$ ) in the former system. This also indicates that the threshold for dissipative effects is higher for  $^{19}\text{F}+^{194}\text{Pt}$  system which is having  $N_c=126$ . Back et al. [2] has indicated that systems with  $N_c=126$  may have higher excitation energy threshold, where fission delay effects are more pronounced.

Experimental results obtained were fitted using Bohr-Wheeler model and Kramer's model for the  $^{16}\text{O}+^{198}\text{Pt}$  system. It has been observed that Bohr-Wheeler model under predicts the experimental results as dissipation effects were not included. In Kramer's model [4] excitation energy dependent dissipation coefficient was used to fit the experimental data as shown in figure 2. The calculations for other systems are in progress.

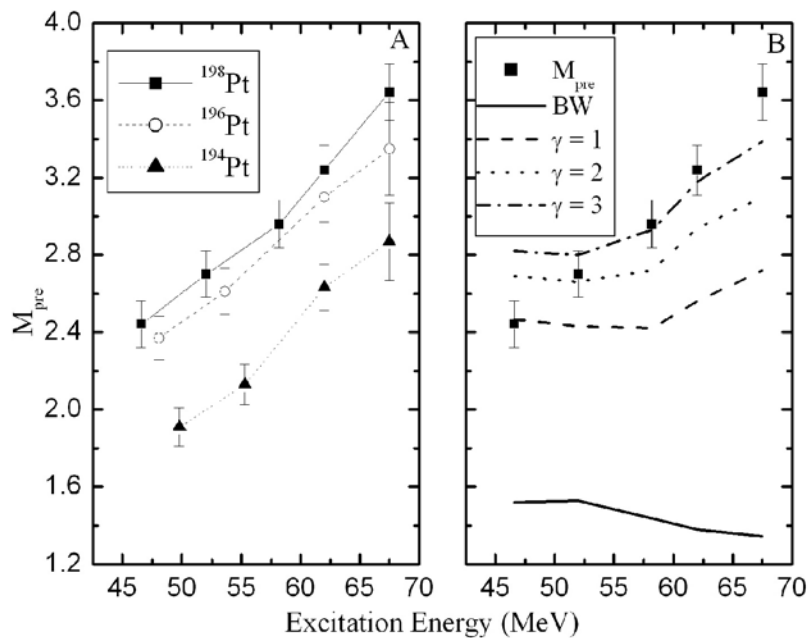


**Fig. 1(A). Variation of  $M_{pre}$  with excitation energy for different systems.**

**Fig. 1(B). Comparison of experimental and theoretical pre-scission neutron multiplicity value predicted by BW and Kramer's model for  $^{19}\text{F} + ^{198}\text{Pt}$  system**

## REFERENCES

- [1] D. Hilscher et al. Ann. Phys. Fr.17, 471 (1992).
- [2] B.B. Back et al. Phys. Rev. C60, 044602 (1999).
- [3] K. Mahata et al. Phys. Rev C65, 034613 (2002).
- [4] H. A. Kramers, Physica (Amsterdam) 7, 284 (1940).

### 5.1.2 Measurements of one and two proton transfer reactions for $^{28}\text{Si}+^{90,94}\text{Zr}$ systems

Sunil Kalkal<sup>1</sup>, S. Mandal<sup>1</sup>, A. Jhingan<sup>2</sup>, J. Gehlot<sup>2</sup>, P. Sugathan<sup>2</sup>, K. S. Golda<sup>2</sup>, N. Madhavan<sup>2</sup>, Ritika Garg<sup>1</sup>, Savi Goyal<sup>1</sup>, Gayatri Mohanto<sup>2</sup>, S. Verma<sup>1</sup>, Rohit Sandal<sup>3</sup>, B. R. Behera<sup>3</sup>, G. Eleonora<sup>4</sup>, H. J. Wollersheim<sup>4</sup>, R. Singh<sup>1,5</sup>

<sup>1</sup>Department of Physics & Astrophysics, University of Delhi, New Delhi.

<sup>2</sup>Inter University Accelerator Centre, Aruna Asaf Ali Marg, New Delhi.

<sup>4</sup>Department of Physics, Panjab University, Chandigarh.

<sup>4</sup>GSI, Darmstadt, Germany.

<sup>5</sup>AINST Noida, U. P.

Heavy ion collisions around the Coulomb barrier offer a very rich variety of phenomena and their coupling effects on each other [1, 2]. The study of transfer reactions serves a wide range of objectives like estimation of relative and absolute spectroscopic factors of nuclear levels [3], understanding the correlations between nucleons [4] and the transition from the quasi elastic to deep inelastic regime [1] etc. These reactions are also a very useful tool to study exotic nuclei far from the stability line [5, 6]. Multinucleon transfer can take place either simultaneously or sequentially indicating the interplay of reactions and nuclear structure. But unfortunately, the mechanism and many features of multinucleon transfer reactions are still not very well understood [3, 4, 7, 8]. In addition to the simultaneous transfer as a cluster, multinucleon transfer is a multistep process in which the colliding nuclei can be inelastically excited before or after the transfer.

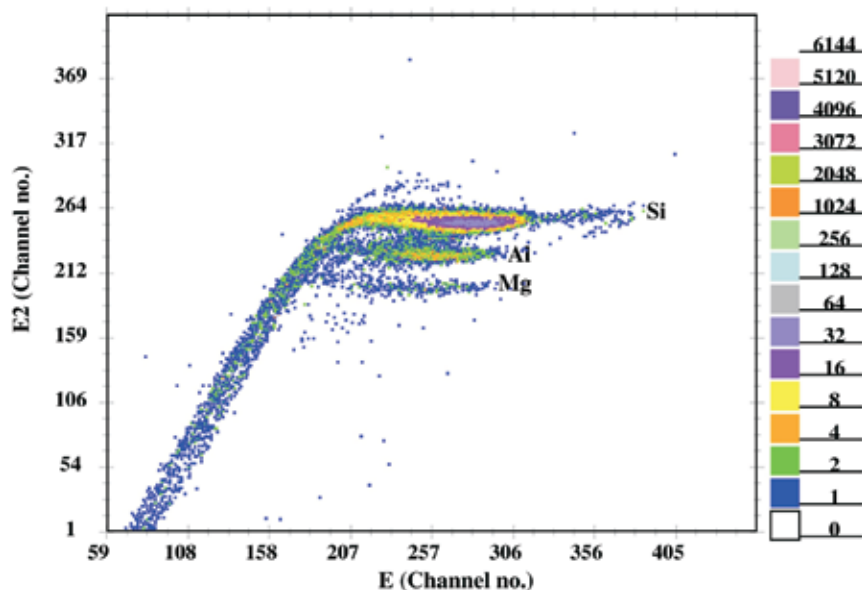
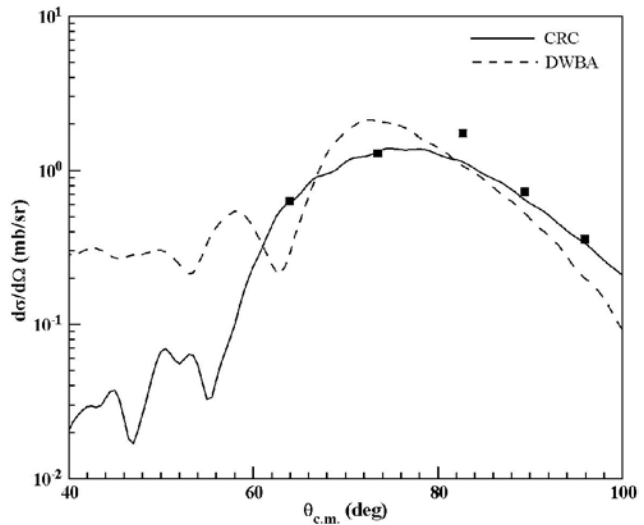


Fig. 1. Particle identification spectrum for  $^{28}\text{Si}+^{94}\text{Zr}$  at  $78^\circ$

The experiment was performed with  $^{28}\text{Si}$  DC beam from 15 UD Pelletron accelerator using General Purpose Scattering Chamber (GPSC) at 120 MeV ( $E_{\text{lab}}$ ). The targets used were isotopically enriched  $^{90,94}\text{Zr}$  (97.65% and 96.07% respectively)  $280 \mu\text{g}/\text{cm}^2$  foils prepared on  $45 \mu\text{g}/\text{cm}^2$  carbon backings in the target lab of IUAC. The timing information (TOF) was obtained with the arrival of projectile-like particles in one MWPC as start signal and of MWPC placed on other arm used for target-like particles as the stop. A kinematic coincidence was set up between the MWPC detectors on the two arms. The angular distribution measurements of the transfer reaction products were performed around the grazing angle at  $42^\circ$ ,  $50^\circ$ ,  $58^\circ$ ,  $66^\circ$ ,  $72^\circ$ ,  $78^\circ$  for the projectile-like transfer products. The other arm was rotated to the corresponding angles for the detection of target-like particles at each angle. The transfer of up to two proton pick-up and two proton stripping could be detected. We could clearly resolve different  $Z$  by using Ionization Chamber. Figure 1 shows a two dimensional spectrum of  $\Delta E_2$  (energy lost by the particles in second segment of IC) vs. total energy ( $E$ ) deposited in IC for  $^{28}\text{Si}+^{94}\text{Zr}$  system at  $78^\circ$ . The angular distribution of the one and two proton stripping channels were extracted for both the systems and the theoretical calculations were performed using quantum mechanical coupled channels code FRESKO [9]. The Akyuz Winther parameterization [10] of the optical model parameters was used in these calculations. To take absorption into account, an imaginary part of the optical potential was used with the following values of the parameters,  $W_0=50$  MeV,  $r_w=1.0$  fm,  $a_w=0.4$  fm. It is to be mentioned that in the transfer CRC calculations, we have used finite range approximation in the prior interaction taking into account the full remnant terms. The higher order multistep transfer processes involving inelastic excitations of the target and the projectile before/after reaction were also included while performing the coupled channels calculations. The Coulomb radius parameter was assumed to be  $r_{\text{oc}}=1.25$  fm. Same values of the AW parameters were used in the calculations for the fusion excitation functions [11] using CCFULL, and the transfer reactions using FRESKO. For one and two proton transfer calculations, the Woods Saxon shape of the potentials were used between  $^{27}\text{Al}+1\text{p}$ ,  $^{26}\text{Mg}+2\text{p}$ ,  $^{90}\text{Zr}+1\text{p}$ ,  $^{90}\text{Zr}+2\text{p}$ ,  $^{94}\text{Zr}+1\text{p}$ ,  $^{94}\text{Zr}+2\text{p}$  with realistic diffuseness and radius parameters. The strength of potential was adjusted to reproduce one and two proton separation energies for both the systems.



**Fig. 2. The experimental angular distribution of one proton stripping channel for  $^{28}\text{Si}+^{90}\text{Zr}$  system along with the theoretical calculations using FRESKO**

Figure 2 shows the experimental results of the one proton stripping channel along with the FRESKO calculations for  $^{28}\text{Si}+^{90}\text{Zr}$  system. As expected, the differential transfer cross section was peaking around the grazing angle. An oscillatory behavior was observed at the forward angles in theoretical calculations which might be due to the interference effects as for a certain angle, there might be scattering from the different impact parameters giving the same deflection angle [7]. Quantum mechanically, the oscillations may be attributed to the diffraction phenomenon. A reasonably good agreement was observed between the theoretically calculated and the experimentally observed angular distributions. It might be mentioned that one step DWBA calculations were also performed which could reproduce the trend well.

In Figure 3, the experimental differential cross sections, the full CRC calculations and the one step DWBA calculations are shown for two proton stripping channel in the case of  $^{28}\text{Si}+^{94}\text{Zr}$  system at 120 MeV. In this case one step DWBA gave a better prediction of the angular distribution as compared to the  $^{28}\text{Si}+^{90}\text{Zr}$  system. It is to be noted that the angular distributions of the two proton stripping were much broader than the one proton stripping in both the systems which may be due to the dominance of the sequential transfer at the much above the barrier energy. No sharp peaking was observed at the grazing angle in the two proton stripping channel which was very well observed experimentally and predicted theoretically by both full coupled reaction channels calculations and one step DWBA in the case of one proton stripping for both the systems.

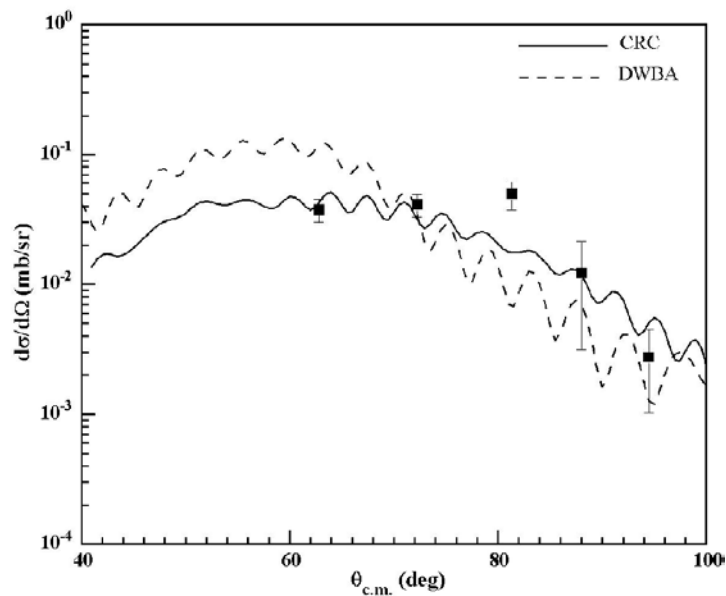


**Fig. 3. The experimental angular distribution of two proton stripping channel for  $^{28}\text{Si}+^{94}\text{Zr}$  system along with theoretical calculations using FRESKO**

## REFERENCES

- [1] K. E. Rehm, *Annu. Rev. Nucl. Part. Sci.* 41, 429 (1991).
- [2] W. Reisdorf, *J. Phys. G* 20, 1297 (1994).
- [3] C. Y. Wu, W. Von Oertzen, D. Cline, M. W. Guidry, *Annu. Rev. Nucl. Part. Sci.* 40, 285 (1990).
- [4] W. Von Oertzen, A. Vitturi, *Rep. Prog. Phys.* 64, 1247 (2001).
- [5] H. Lenske, G. Schrieder, *Eur. Phys. J. A* 2, 41 (1998).
- [6] Yu. E. Penionzhkevich, G. G. Adamian, N. V. Antonenko, *Phys. Lett. B* 621, 119 (2005).
- [7] W. R. Philips, *Rep. Prog. Phys.* 40, 345 (1977).
- [8] L. Corradi, G. Pollarolo, S. Szilner, *J. Phys. G* 36, 113101 (2009).
- [9] Ian J. Thompson, *Comput. Phys. Commun.* 7, 167 (1988).
- [10] R. A. Broglia and A. Winther, *Heavy Ion Reaction Lecture Notes, Volume 1: Elastic and Inelastic Reactions* (Benjamin/Cummings, Reading, 1981).
- [11] Sunil Kalkal et. al, *Phys. Rev. C* 81, 044610 (2010).

### 5.1.3 Fission fragment mass distribution measurement for the reaction $^{19}\text{F}+^{184}\text{W}$

S. Nath<sup>1</sup>, K.S. Golda<sup>1</sup>, A. Jhingan<sup>1</sup>, J. Gehlot<sup>1</sup>, E. Prasad<sup>2</sup>, Sunil Kalkal<sup>3</sup>, M.B. Naik<sup>4</sup>, P. Sugathan<sup>1</sup>, N. Madhavan<sup>1</sup> and P.V. Madhusudhana Rao<sup>5</sup>

<sup>1</sup>Inter University Accelerator Centre, Aruna Asaf Ali Marg, New Delhi

<sup>2</sup>Department of Physics, Calicut University, Calicut

<sup>3</sup>Department of Physics and Astrophysics, Delhi University, Delhi

<sup>4</sup>Department of Physics, Karnatak University, Dharwad

<sup>5</sup>Department of Nuclear Physics, Andhra University, Visakhapatnam

Extending the limit of the periodic table of elements has been an area of intense theoretical and experimental investigation for the last few decades. Quasi-fission [1], in which the composite system formed after capture of projectile and target disintegrates before forming a compound nucleus (CN), is a major roadblock towards that goal. Experimental evidences are increasingly becoming available for the onset of quasifission in comparatively lighter systems [2]. It is interesting to pursue a systematic study of the factors that affect quasi-fission. Broadened mass distribution of the fission fragments (FFs) is one of the experimental signatures of quasifission. We report here measurement of FF mass distribution in the reaction  $^{19}\text{F}+^{184}\text{W}$ .

The experiment was performed at the 15UD Pelletron accelerator facility of the IUAC, New Delhi. A pulsed beam of  $^{19}\text{F}$  with 250 ns pulse separation and 1 ns pulse width was bombarded onto a  $210\ \mu\text{g}/\text{cm}^2$   $^{184}\text{W}$  target [3] with a  $110\ \text{mg}/\text{cm}^2$  carbon

backing. Beam energy was changed from 90 to 125 MeV, in steps of 5 MeV to measure the energy dependence of FF mass distribution. Two multi-wire proportional counters (MWPCs) [4] of active area  $20 \times 10 \text{ cm}^2$  were used to detect the FFs in coincidence. The MWPCs were mounted on the two rotatable arms of the scattering chamber: the forward detector ( $\text{MWPC}_{\text{left}}$ ) centered at polar angle ( $\theta$ ) =  $60.8^\circ$  (azimuthal angle,  $\phi = 90^\circ$ ) and the backward detector ( $\text{MWPC}_{\text{right}}$ ) centered at  $\theta = 88^\circ$  ( $\phi = 270^\circ$ ). The nearest distance to  $\text{MWPC}_{\text{left}}$  from the target was 55.9 cm and that to  $\text{MWPC}_{\text{right}}$  was 39.3 cm. The MWPCs were operated with isobutane gas at a pressure of 3.0 mbar and provided very good separation between FFs and direct reaction products.

The masses of the fission fragments were determined from precise measurements of flight paths and flight time difference between the complimentary fragments [5] entering the two MWPCs. The electronic delay between the two anode pulses was estimated from the condition of identity of the mass distributions measured with the two detectors. The width of the mass distribution was obtained by fitting the experimental mass distribution with a Gaussian. The standard deviation ( $\sigma_m$ ) from the fits is plotted against the centre of mass energy ( $E_{\text{c.m.}}$ ) in Fig. 1. We observe that  $\sigma_m$  varies slowly with energy and there is no anomalous increase in the width, which is often interpreted as the signature of deviation from CN behavior [6], in the energy range studied. Therefore, we conclude that the present system proceeds towards the formation of CN after capture, and quasi-fission is not observed.

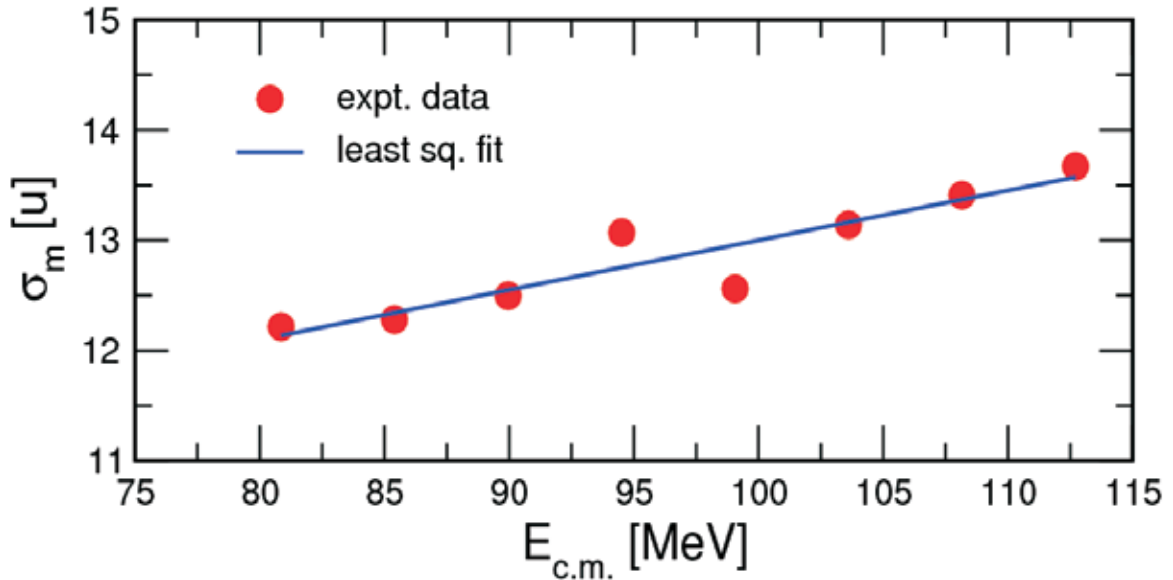


Fig. 1. Variation of  $\sigma_m$  for the fission fragment mass distribution with c.m.energy

Our earlier measurements of evaporation residue (ER) excitation function [7] and ER-gated CN angular momentum ( $l$ ) distribution [8] for  $^{19}\text{F}+^{184}\text{W}$  hinted at the onset of instability in the CN ( $^{203}_{83}\text{Bi}$ ) after crossing of the  $Z = 82$  shell. We interpreted the reduction of ER cross section and the depletion of higher  $l$ -values in terms of lowered fission barrier ( $B_f(0)$ ), assuming that non-compound nucleus processes (e.g. quasi-fission) was not significant. The present observation thus endorses the conclusions made in our earlier work.

We thank the Pelletron staff of IUAC for providing pulsed beam of excellent quality and Dr. A. Roy for useful discussions.

## REFERENCES

- [1] W.J. Swiatecki, Phys. Scr. 24, 113 (1981).
- [2] E. Prasad et al., Phys. Rev. C 81, 054608 (2010).
- [3] P.D. Shidling et al., Nucl. Instr. Meth. A 590, 79 (2008).
- [4] A. Jhingan et al., Rev. Sci. Instrum. 80, 123502 (2009).
- [5] R.K. Choudhury et al., Phys. Rev. C 60, 064609 (1999).
- [6] T.K. Ghosh et al., Phys. Lett. B 627, 26 (2005).
- [7] S. Nath et al., Phys. Rev. C 81, 064601 (2010).
- [8] S. Nath et al., Nucl. Phys. A 850, 22 (2011).

### 5.1.4 Investigation of fission reaction dynamics and neutron multiplicity for the $^{16}\text{O}+^{204,206,208}\text{Pb}$ systems

Savi Goyal<sup>1</sup>, S. Mandal<sup>1</sup>, P.Sugathan<sup>2</sup>, K.S.Golda<sup>2</sup>, Akhil Jhingan<sup>2</sup>, Sunil Kalkal<sup>1</sup>, Varinderjit Singh<sup>3</sup>, Davinder Siwal<sup>1</sup>, Ritika Garg<sup>1</sup>, Maninder Kaur<sup>3</sup>, Mansi Saxena<sup>1</sup>, S.Verma<sup>1</sup>, Suresh Kumar<sup>1</sup>, Mohini Gupta<sup>4</sup>, Subinit Roy<sup>5</sup>, B.R.Behera<sup>3</sup>, R.Singh<sup>6</sup>

<sup>1</sup>Department of Physics & Astrophysics, University of Delhi.

<sup>2</sup>Inter University Accelerator Centre, Aruna Asaf Ali Marg, New Delhi.

<sup>3</sup>Department of Physics, Panjab University, Chandigarh.

<sup>4</sup>Manipal University, Karnatka.

<sup>5</sup>Saha Institute of Nuclear Physics, Kolkata.

<sup>6</sup>AINST, Noida.

The fission of highly excited compound nuclei formed in heavy-ion-induced fusion reactions has been a topic of great interest, both theoretically and experimentally

since the discovery of fission. The experimental probes to understand the fusion-fission reaction dynamics are the measurement of  $n$ ,  $p$ ,  $\alpha$ , giant dipole resonance (GDR)  $\gamma$ , evaporation residues (ERs) and fission fragments (FFs). These probes characterize the fission process. Amongst all the probes mentioned, pre scission neutrons are the most commonly used probe to understand the heavy ion induced fusion-fission reaction dynamics. Since neutron emission is the fastest process, it is the most sensitive probe to the small differences in the lifetime of different compound systems. Another advantage of using this probe is the absence of the coulomb barrier. Experimentally measured pre-scission neutron yield is compared with the statistical model prediction and the excess yield, if any, is interpreted to be due to the damping of the fission process. Shell effects play an important role in determining the nuclear structure, and the related information of the shell effects [1] in the fission process is valuable. Nuclear dissipation has a relation with neutron closure shell.

The experiment was conducted at Inter University Accelerator Centre, New Delhi (IUAC) using the National Array of Neutron Detectors (NAND).  $^{16}\text{O}$  pulsed beam of various lab energies having a repetition rate of 250 nsec was delivered by IUAC Pelletron and the first module of the superconducting linear accelerator facility (LINAC). The targets used were isotopically enriched  $^{204,206,208}\text{Pb}$  of thickness  $\sim 1.5 \text{ mg/cm}^2$  (self-supporting), prepared at target lab of IUAC. For the detection of fission fragments, two Multi-Wire Proportional Counters [2] (MWPC) of active area  $20 \times 10 \text{ cm}^2$  were placed at the folding angles ( $70^\circ$  and  $80^\circ$ ) were placed inside the target chamber of NAND. The distance of these detectors from the target was 19.7 cm. Two silicon surface barrier detectors were also placed at  $\pm 16^\circ$  with respect to beam direction for monitoring purposes. Inside view of the chamber is shown in fig.1

The neutrons were detected in coincidence with fission events by twenty four liquid scintillator (NE213 and BC501) detectors, out of which 16 were in reaction plane and 8 were placed at  $\pm 15^\circ$  with respect to the reaction plane. Among the detectors which were placed in plane, eight were at a distance of 2 meters and remaining eight were at a distance of 1 meter from the target. The angular coverage is from  $30^\circ$  -  $150^\circ$ . Because of the requirement of minimum gamma background in the neutron spectra, the beam dump was extended about 3m downstream from the target and the beam pipe was shielded with lead and borated paraffin. Discrimination between neutrons and gammas was made by using pulse shape discrimination (PSD) based on zero cross technique and TOF. The threshold and gain settings of pulse shape discrimination modules [3] were done by using  $^{137}\text{Cs}$  source. The timing information (TOF) was obtained with arrival of particles at MWPC gated with RF as start and neutrons as stop. The time width of the LINAC was continuously measured and it was found to be approximately 800ps. The measurements were performed for the systems  $^{16}\text{O} + ^{204,206,208}\text{Pb}$  from 90 MeV to 120 MeV (in lab) in steps of 6 MeV ( $E_{\text{CN}}^* = 40$  to 64 MeV).



**Fig.1. Inside view of the chamber**

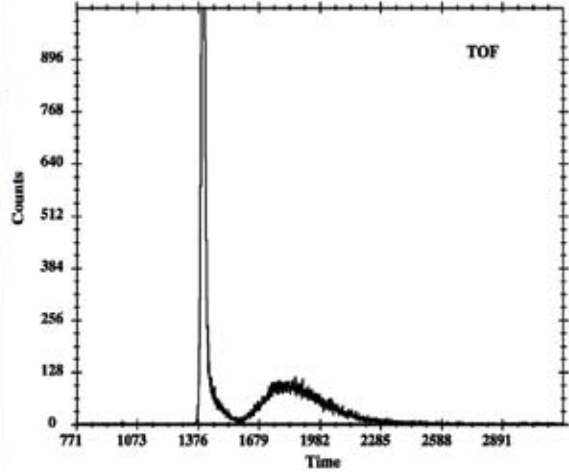


**Fig. 2. TOF spectrum for n- $\gamma$  separation**

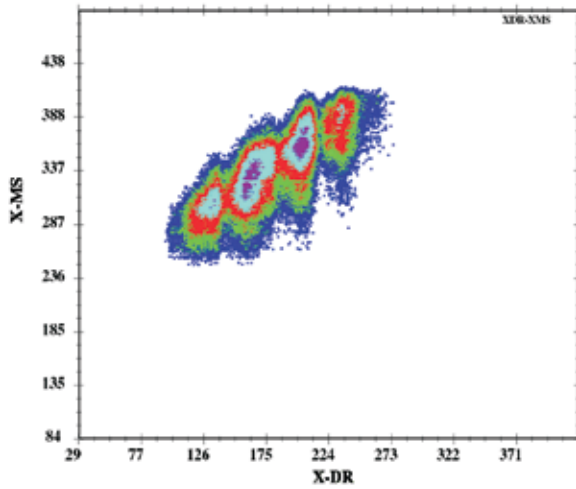


**Fig. 3. Two dimensional spectrum of X-position of both MWPC's**

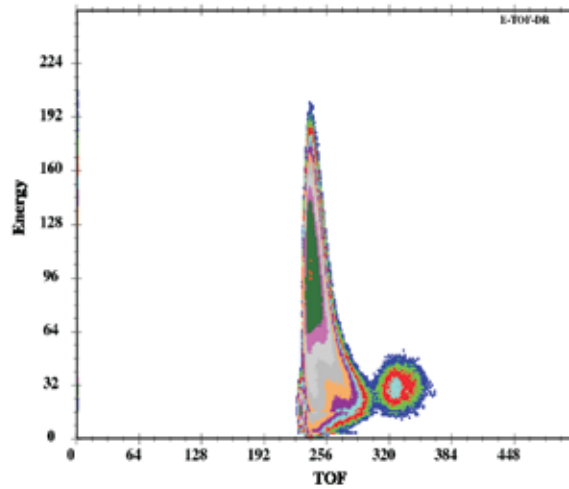


**Fig. 4. Two dimensional plot between energy and time of flight of MWPC**

Fig. 2 shows the one dimensional spectra of time of flight (TOF) for  $^{16}\text{O} + ^{208}\text{Pb}$  at 119.3 MeV. This neutron detector was placed at a distance of 2 meters from the target, and it clearly shows the well separated peak for neutron and gamma particles. Fig. 3 shows a two dimensional plot between the X-positions of both the MWPC's placed at folding angles. A two dimensional plot was generated from the energy and the timing signal of the MWPC which helps to separate the fission fragments from the elastic and target like particles (fig.4).

## REFERENCES

- [1] A.Kelic et al, Europhys. Lett., 47 (5) (1999) 552
- [2] Akhil Jhingan et.al. Review of scientific Instruments 80 (2009) 123502
- [3] S. Venkataramanan et al. Nucl. Instr. and Meth. A 596 (2008) 248

### 5.1.5 Effect of projectile breakup on fission in ${}^6,7\text{Li}+{}^{238}\text{U}$

S. Santra<sup>1</sup>, P. K. Rath<sup>2</sup>, N. L. Singh<sup>2</sup>, B. R. Behera<sup>3</sup>, B. K. Nayak<sup>1</sup>, R. K. Choudhury<sup>1</sup>, A. Jhingan<sup>4</sup>, P. Sugathan<sup>4</sup>, K. S. Golda<sup>4</sup>, S. Sodaye<sup>5</sup>, S. Appannababu<sup>2</sup>, E. Prasad<sup>4</sup>, Amit Kumar<sup>5</sup>, D. Patel<sup>2</sup>

<sup>1</sup>Nuclear Physics Division, Bhabha Atomic Research Centre, Mumbai

<sup>2</sup>Physics Department, The M. S. University of Baroda, Vadodara

<sup>3</sup>Department of Physics, Panjab University, Chandigarh

<sup>4</sup>Inter University Accelerator Centre, Aruna Asaf Ali Marg, New Delhi

<sup>5</sup>Radiochemistry Division, Bhabha Atomic Research Centre, Mumbai

Measurements by Freiesleben et al.[1] show that the fission cross sections for  ${}^6\text{Li}+{}^{238}\text{U}$  at energies around the Coulomb barrier is systematically higher than  ${}^7\text{Li}+{}^{238}\text{U}$ . Although this observation has been attributed to the higher probability of transfer induced fission for the former with respect to the latter, detailed explanations were not provided. To understand this phenomenon, we have performed coincidence measurements to detect both the fission fragments as well as projectile breakup fragments.

The experiment was performed using  ${}^6,7\text{Li}$  beams from the 15-UD Pelletron facility at Inter University Accelerator Centre, New Delhi. The  ${}^{238}\text{U}$  target of thickness  $\sim 100 \mu\text{g}/\text{cm}^2$  sandwiched between two layers of  ${}^{12}\text{C}$  of thickness  $\sim 15 \mu\text{g}/\text{cm}^2$  was used. Two multi-wire proportional counter (MWPC) detectors were used to detect fission fragments. Both the MWPCs have an active area of  $20 \times 10 \text{ cm}^2$  and provide position signals in horizontal (X) and vertical (Y) planes, timing signal for time of flight measurements and energy signal giving the differential energy loss in the active volume. The start of the timing was taken from a small area ( $3.7 \times 3.7 \text{ cm}^2$ ) transmission type fast timing multi-wire proportional counter and the stop was taken from the large area MWPCs. The combination of small MWPC and any one of the large MWPCs provide absolute timing of the fission fragments. Time of flight signal in combination with differential energy loss signal gives a clean separation of fission fragments from projectile and target like particles. Fig.1 shows typical fission fragment folding angles distributions (FFFAD) in the reaction plane  $\theta_{\text{c.m.}}$  versus out of the plane  $\phi_{\text{c.m.}}$  for  ${}^6\text{Li}$  at two energies and their respective projections on reaction plane.

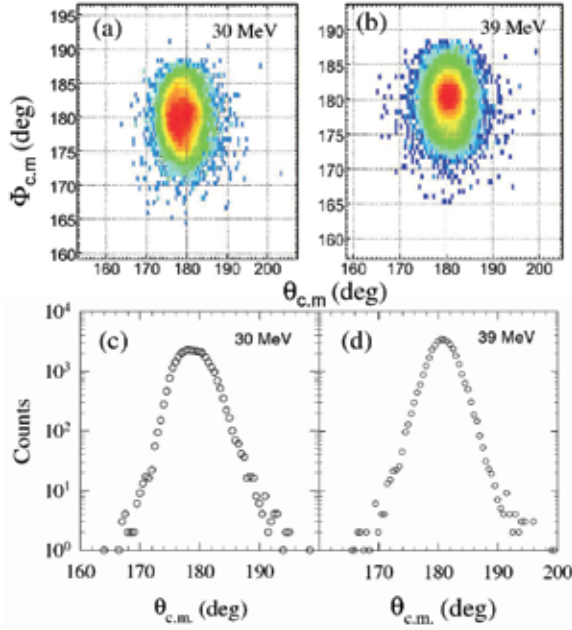


**Fig.1. Fission fragment folding angles distributions (FFFAD) in the reaction plane  $\theta_{c.m.}$  versus out of the plane  $\phi_{c.m.}$  for  ${}^6\text{Li}$  beam energies of (a) 30 MeV and (b) 39 MeV. Respective projections on reaction plane are shown in (c) and (d) showing the difference in FWHM of the FFFAD.**

In Fig.2, full width at half maximum (FWHM) of FFFADs for  ${}^{6,7}\text{Li}+{}^{238}\text{U}$  systems have been compared with the ones with tightly bound projectiles. It can be observed that the FWHM at energies above the Coulomb barrier for  ${}^{16}\text{O}+{}^{232}\text{Th}$ [2] and  ${}^{14}\text{N}+{}^{232}\text{Th}$ [3] systematically decreases with lowering the beam energy. But the energy dependence behavior of the FWHM for present systems is quite different. It first decreases and then increases with energy. The increase in the FWHM at lower energies is possibly due to the large contribution of breakup fragment induced fission compared to complete fusion-fission.

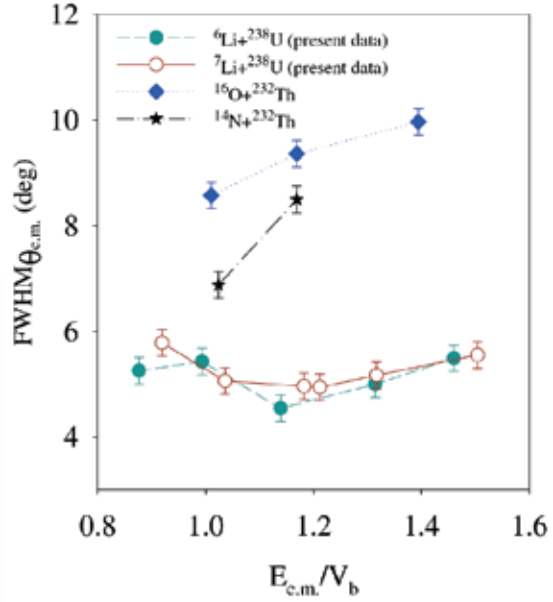


**Fig.2. Full width at half maximum (FWHM) of FFFAD as a function of energy normalized to Coulomb barrier ( $E_{c.m.}/V_b$ ).**

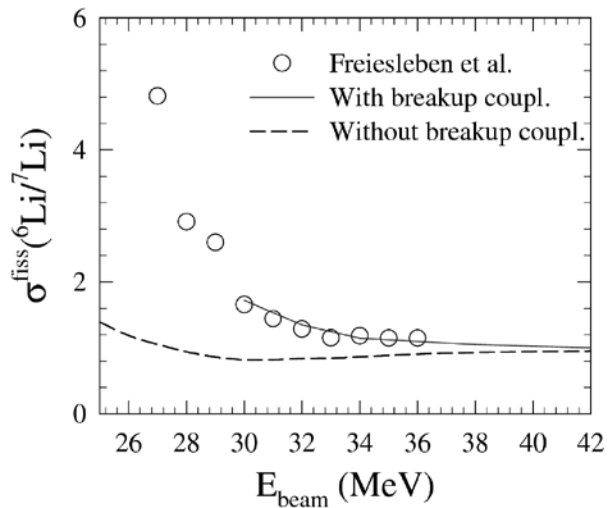


**Fig.3. Ratio of fusion excitation function data [1] of  ${}^6\text{Li}+{}^{238}\text{U}$  to  ${}^7\text{Li}+{}^{238}\text{U}$ . Results of FRESKO calculations for fusion cross sections are shown as a solid line (see text for details).**

Ratio of fusion excitation function data [1] of  ${}^6\text{Li}+{}^{238}\text{U}$  to  ${}^7\text{Li}+{}^{238}\text{U}$  at near barrier energies is shown as open circles in Fig.3. It can be observed that the ratio increases with the decrease in energy, which can be understood in terms of low breakup threshold of  ${}^6\text{Li}$  compared to  ${}^7\text{Li}$  due to which the contribution from breakup fragments induced fusion/fission for the former is much higher than the latter. To estimate the total (=complete + incomplete) fusion for the above system, continuum discretized coupled channels (CDCC) calculations are performed using cluster-folded potentials. Coupling scheme used in the calculations for breakup states is similar to Ref. [4] for  ${}^6\text{Li}$  and Ref.[5] for  ${}^7\text{Li}$ . Assuming the breakup to be the most dominant direct reaction channel, the cumulative absorption cross section due to long ranged imaginary potential calculated in the CDCC calculations equals to total fusion cross section. The ratio of the total fusion cross section thus calculated for  ${}^6\text{Li}+{}^{238}\text{U}$  to  ${}^7\text{Li}+{}^{238}\text{U}$  is shown as a solid line in Fig.3, which shows similar trend in the observed energy dependence as the ratio of fission cross sections for the two systems. Dashed line represents the results without breakup coupling. This corroborates with our understanding that the increase in FWHM of the FFFADs at sub-barrier energies is due to the presence of breakup fusion that dominates over complete fusion.

## REFERENCES

- [1] H. Freiesleben *et al.*, Phys. Rev. C 12 (1975) 42.
- [2] R.K. Choudhury *et al.*, Phys. Rev. C 60 (1999) 054609.
- [3] B.R. Behera *et al.*, Phys. Rev. C 69 (2004) 064603.
- [4] S. Santra *et al.*, Phys. Lett. B 677 (2009) 139.
- [5] V. V. Parkar *et al.*, Phys. Rev. C 78 (2008) 021601(R).

### 5.1.6 Role of N/Z in the Pre-Scission Neutron Multiplicities for the ${}^{16,18}\text{O}+{}^{194,198}\text{Pt}$ Systems

Rohit Sandal<sup>1</sup>, B.R. Behera<sup>1</sup>, Varinderjit Singh<sup>1</sup>, A. Kumar<sup>1</sup>, G. Singh<sup>1</sup>, K.P. Singh<sup>1</sup>, M. Kaur<sup>1</sup>, S. Mandal<sup>2</sup>, S. Kalkal<sup>2</sup>, D. Siwal<sup>2</sup>, M. Saxena<sup>2</sup>, S. Goyal<sup>2</sup>, E. Prasad<sup>3</sup>, P. Sugathan<sup>4</sup>, A. Jhingan<sup>4</sup>, K.S. Golda<sup>4</sup>, R.P. Singh<sup>4</sup>, R.K. Bhowmik<sup>4</sup>, M.B. Chatterjee<sup>4</sup>, R.K.Choudhury<sup>5</sup>, K. Mahata<sup>5</sup>, S. Santra<sup>5</sup>, S.Kailas<sup>5</sup>, A. Saxena<sup>5</sup>

<sup>1</sup>Department of Physics, Panjab University, Chandigarh

<sup>2</sup>Department of Physics and Astrophysics, University of Delhi

<sup>3</sup>Department of physics, University of Calicut, Calicut

<sup>4</sup>Inter University Accelerator Centre, Aruna Asaf Ali Marg, New Delhi

<sup>5</sup>Nuclear Physics Division, Bhabha Atomic Research Centre, Mumbai.

The fission dynamics of hot compound nuclei continues to be a subject of considerable interest due to the fact that the fission life time determined from the

argument of Bohr and Wheeler turns out to be too small to allow for the rather large number of experimentally observed light particles evaporated prior to fission [1]. It was therefore felt necessary to look beyond the statistical model and this gave rise to a revival of interest in the original work of Kramers who considered fission as a diffusive probability flow over the fission barrier. Extensive studies have been carried out in the past to determine the dynamical time scales from the measurements of the multiplicity of pre-scission neutrons, protons, alpha particles and electric dipole  $\gamma$ -rays, in heavy-ion induced fusion–fission reactions [1–3]. For instance, calculations of the lifetimes of the excess pre-scission neutrons have been used to estimate the fission delay time, which depends directly on the magnitude of the viscosity. To obtain the information of the dissipation strength beyond the saddle point, i.e., the saddle-to-scission friction strength, it is necessary to employ those observables that can be affected by the saddle-to-scission friction effects. The fission dynamics as a function of  $(N-Z)/A$  (i.e. the effect of the neutron excess from the reaction system chosen) and the contribution coming from near scission configuration is not yet studied systematically. Keeping this in mind, we have measured neutron multiplicities from fission fragments for a number of heavy nuclei by populating compound nucleus with same  $Z$  (proton number) but with different  $N$  (neutron number). We report here the results of neutron multiplicity measurements for  $^{16,18}\text{O} + ^{194,198}\text{Pt}$  reactions at different set of excitation energies which populate the compound nuclei with the same  $Z$  ( $Z=86$ , Rn) but different value of  $N$ . The fission dynamics as a function of  $(N/Z)$ , the effect of the neutron excess from the reaction system chosen is studied systematically here.

The experiments were carried out at IUAC(New Delhi), using pulsed beams of  $^{16}\text{O}(E_{\text{lab}}=118,110,100$  and  $88$  MeV) and  $^{18}\text{O}(120,116,108,112.5,102,97.5,90$  and  $85.5$  MeV) from the 15UD Pelletron plus first module of super-conducting linear accelerator (LINAC). The experiment was performed by populating the compound nuclei at 79,71.7,61 and 50 MeV excitation energies. Targets used for this experiment are  $^{194}\text{Pt}$  ( $1.75\text{mg}/\text{cm}^2$ ) and  $^{198}\text{Pt}$  ( $2.15\text{mg}/\text{cm}^2$ ). Fission fragments were detected by a pair of large area Multi-wire proportional counter (MWPC) ( $5''\times 3''$ ) kept at the fission fragment folding angle. Two silicon surface barrier detectors were placed at  $\pm 16^\circ$  out of plane for the normalization purpose. 16 neutron detectors (NE213 and BC501A), of  $5''$  diameter and  $5''$  depth, were kept at 2 meter away from the target at different angles. The neutron detector array threshold was kept at about 0.5 MeV by calibrating it with standard  $\gamma$  source ( $^{137}\text{Cs}$ ). The efficiency correction for the neutron detectors was performed using the Monte Carlo computer code MODEFF. Discrimination between neutrons and gamma rays was made by using both neutron time of flight (TOF) and pulse shape discrimination (PSD) techniques. For minimizing gamma background in the neutron spectra, the beam dump was extended about 4 m downstream from the target and the beam pipe was well shielded with lead and borated paraffin. The trigger of the data acquisition was generated by logic OR of the two fission fragments (Cathode of the two MWPC) and it further ANDED with the RF of the beam.

Sixteen laboratory neutron energy spectra, selecting various fission fragment-neutron correlation angles, were constructed. The neutron spectra corrected for the detector efficiency, were simultaneously fitted by assuming three moving sources corresponding to a pre-scission composite nucleus and post-scission (two fission fragments). To determine the pre and post-scission parameters the Watt expression [2] was used for the neutron emission spectra. The pre-scission neutron multiplicity  $M^{\text{pre}}$  post-scission fragment neutron multiplicity and temperature  $M^{\text{post}}$ ,  $T^{\text{post}}$  (here  $M^{\text{post}}$  refers to the neutron multiplicity from both fragments) were determined from the fits. The temperatures  $T^{\text{pre}}$  was calculated as  $T = \sqrt{E^*/a}$ , where  $E^*$  is the excitation energy and  $a$  is the level density parameter, taken as  $A/10$  for compound nucleus. Minimum value of  $\chi^2/(\text{degrees of freedom})$  are in range of 0.001-0.003. PACE2 calculations were performed taking acceptable parameters tested for a wide range of target projectile systems in this mass region. The experimentally measured value for the same system at this excitation energy is quite large as compare to statistical model calculations. The variation of  $M^{\text{pre}}$  with  $N/Z$  is shown in Fig. 1. We see an increasing tendency of  $M^{\text{pre}}$  value with the increase of  $N/Z$ . The total neutron multiplicity ( $M^{\text{tot}}$ ) also represents total available excitation energy, which is given by  $E_{\text{ex}} + Q_{\text{fiss}} - \text{TKE}$ . Here,  $Q_{\text{fiss}}$  is the fission Q value. It is seen from the Fig. 2, the average number of evaporated neutrons per MeV increases with the increase in  $N/Z$  ratio. The increasing tendency for the system  $^{18}\text{O}+^{194}\text{Pt}$  at the lowest excitation energy is less and it might be perhaps due to the shell closure ( $N_{\text{C}}=126$ ) of the compound nucleus  $^{212}\text{Rn}_{86}$  formed by the above reaction. The dynamical time  $\tau_{\text{fission}}$  of the fissioning system can be deduced from the number of excess neutrons  $M^{\text{pre}}(\text{excess})$  using PACE2. The  $\tau_{\text{fission}}$  values calculated from these calculations for  $^{16}\text{O}+^{194}\text{Pt}$ ,  $^{18}\text{O}+^{194}\text{Pt}$ ,  $^{16}\text{O}+^{198}\text{Pt}$ ,  $^{18}\text{O}+^{198}\text{Pt}$  are  $32 \pm 7 * 10^{-21}$ ,  $39 \pm 3 * 10^{-21}$ ,  $26 \pm 2 * 10^{-21}$ ,  $19 \pm 2 * 10^{-21}$  Sec respectively.

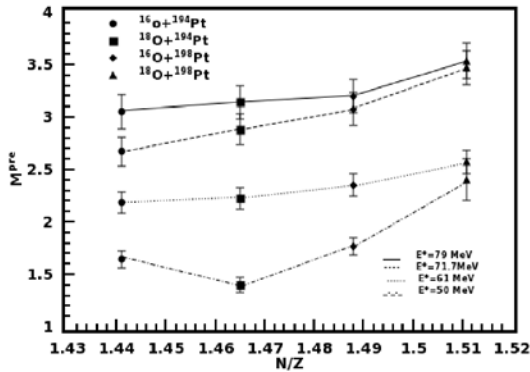


**Fig. 1** Variation of  $M^{\text{pre}}$  with  $N/Z$  for  $^{16,18}\text{O}+^{194,198}\text{Pt}$ .

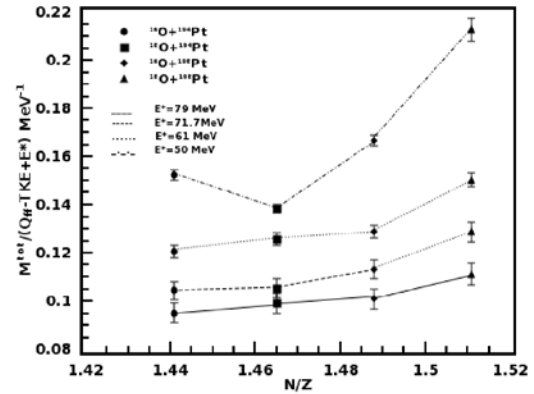


**Fig. 2** Ratio of total neutron multiplicity and available excitation energy for the various systems under study.

## REFERENCES

- [1] D.J. Hinde, R.J. Charity, G.S. Foote, J.R. Leigh and J.O. Newton, Phys. Rev. Lett. 52 986 (1984); 53 2275(E) (1984)
- [2] A. Saxena, A. Chatterjee, R.K.Choudhury,S.S. Kapoor, D.M. Nadkarni, Phys. Rev. C 49 932 (1994).
- [3] J.P. Lestone et al.Phys.Rev.Lett. 67, 1078 (1991).

### 5.1.7 Enhanced $0^+_{gs} \rightarrow 2^+_1$ transition strength in $^{112,114}\text{Sn}$

R. Kumar<sup>1</sup>, P. Doornenbal<sup>2</sup>, A. Jhingan<sup>1</sup>, R.K. Bhowmik<sup>1</sup>, S. Appannababu<sup>3</sup>, P. Bednarczyk<sup>4,5</sup>, L. Caceres<sup>6</sup>, J. Cederkall<sup>7,8</sup>, A. Ekstrom<sup>8</sup>, R. Garg<sup>9</sup>, J. Gerl<sup>4</sup>, M. Gorska<sup>4</sup>, H. Grawe<sup>4</sup>, J. Kaur<sup>10</sup>, I. Kojouharov<sup>4</sup>, S. Mandal<sup>9</sup>, S. Mukherjee<sup>3</sup>, S. Muralithar<sup>1</sup>, W. Prokopowicz<sup>4</sup>, P. P. Singh<sup>11</sup>, P. Reiter<sup>12</sup>, H. Schaffner<sup>4</sup>, A. Sharma<sup>13</sup>, R.P. Singh<sup>1</sup>, D. Siwal<sup>9</sup>, H.J. Wollersheim<sup>4</sup>

<sup>1</sup> Inter-University Accelerator Centre, Aruna Asaf Ali Marg, New Delhi

<sup>2</sup> RIKEN Nishina Center for Accelerator-Based Science, Wako, Saitama, Japan

<sup>3</sup> Department of Physics, M.S. University of Baroda, Vadodara

<sup>4</sup> Helmholtzzentrum für Schwerionenforschung, 64291 Darmstadt, Germany,

<sup>5</sup> The Niewondniczanski Institute of Nuclear Physics, Polish Academy of Sciences, Poland

<sup>6</sup> GANIL, B.P. 5027, 14076 CAEN CEDEX 5, France

<sup>7</sup> PH Department, CERN 1211, Geneva, Switzerland

<sup>8</sup> Department of Physics, Lund University, Lund, Sweden

<sup>9</sup> Department of Physics & Astrophysics, University of Delhi, Delhi

<sup>10</sup> Department of Physics, Panjab University, Chandigarh

<sup>11</sup> INFN-Laboratori Nazionali di Legnaro (LNL), Legnaro (PD), Italy

<sup>12</sup> Institut für Kernphysik, Universität zu Köln, Germany

<sup>13</sup> Department of Physics, Bareilly College, Bareilly

In recent years, tin isotopes, which have the longest shell-to-shell chain of semi-magic nuclei, have been intensively investigated both from experimental and theoretical perspectives. In particular, the excitation energies and the reduced transition probabilities across the  $Z=50$  chain have been examined in detail. Radioactive ion beams yield new experimental results close to the doubly-magic  $^{100}\text{Sn}$  and  $^{132}\text{Sn}$ , but very accurate data of the stable mid-shell nuclei are also of great relevance for our understanding.

In the series of two experiments [1, 2], the second experiment was carried out at IUAC where targets of  $^{112}\text{Sn}$  and  $^{116}\text{Sn}$  were bombarded with a  $^{58}\text{Ni}$  beam at 175 MeV using a tandem Van de Graaf accelerator. Both targets were of thickness  $0.53\text{mg}/\text{cm}^2$  with enrichments of 99.5% and 98%, respectively. The scattered beam particles and recoils were detected in an annular gas-filled parallel plate avalanche counter PPAC. The PPAC was position-sensitive in both the azimuthal  $\phi$  and the polar  $\vartheta$  angles. In this experiment Clover Germanium (Ge) detectors were used to measure the de-excited gamma rays. At IUAC four Clover detectors (distance to target  $22\pm 2$  cm) were mounted at  $\vartheta_\gamma \sim 135^\circ$  with respect to the beam direction.

The particle identification and the particle position measurement allowed a precise Doppler correction of the measured  $\gamma$ -ray energies. A Doppler shift correction was performed for each Clover detector ( $\Theta_\gamma$ ,  $\varphi_\gamma$ ) event-by-event. Figure 1 shows the Doppler corrected spectra for  $^{112}\text{Sn}$  excitation (top) and  $^{58}\text{Ni}$  excitation (bottom) with the dominating  $2^+_{1\rightarrow 0_{g.s.}}$  transitions. From the observation of the Doppler corrected  $\gamma$ -ray lines, the relative intensities of transitions in Ni and Sn isotopes can be extracted. The  $B(E2\uparrow)$  value of  $^{112}\text{Sn}$  relative to that of  $^{116}\text{Sn}$  was obtained from the experimental  $\gamma$ -ray decay intensity ratios. At forward scattering angles one is insensitive to the diagonal matrix elements. The experimental data were compared with Coulomb excitation calculations which were performed with the Winther - de Boer COULEX code [3]. The slowing down of the projectiles in the target, the uncertainty of the PPAC boundaries and the adopted  $^{116}\text{Sn}$   $B(E2\uparrow)$  value (3%) were considered for the error calculation in both the cases. A

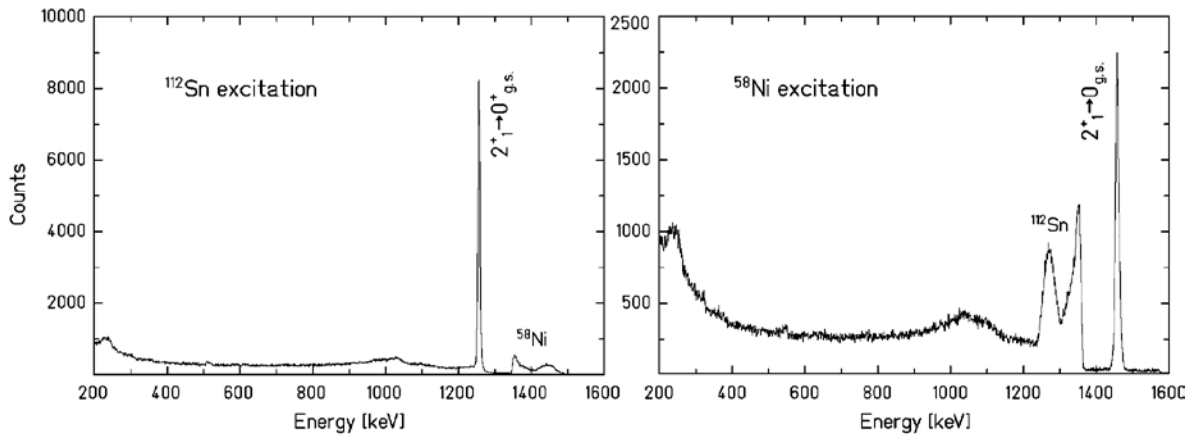


**Fig. 1.** Doppler corrected  $\gamma$ -ray spectra emitted from the  $^{112}\text{Sn}$  target nuclei (left) and the  $^{58}\text{Ni}$  projectiles (right).

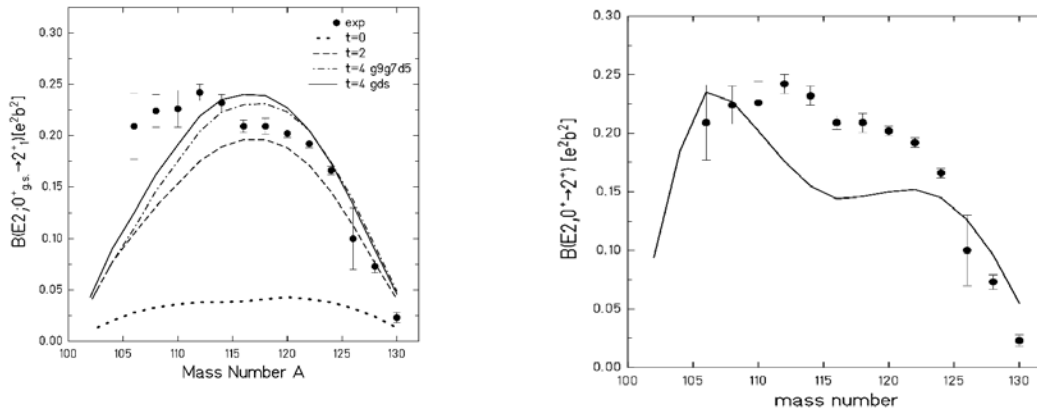


**Fig. 2.** Experimental  $B(E2)$  values are compared to LSSM calculations (left) and RQRPA calculations (right). For the LSSM calculations a  $^{90}\text{Zr}$  core was considered which allows for different proton core excitations ( $t = 0, 2, 4$ )

similar experiment on relative Coulomb excitation of  $^{114,116}\text{Sn}$  beams on a  $^{58}\text{Ni}$  target was carried out earlier at GSI [1]. The resulting  $B(E2\uparrow)$  values in  $^{112}\text{Sn}$  and  $^{114}\text{Sn}$  are  $0.242(8) e^2b^2$  and  $0.232(8) e^2b^2$ , respectively.

The deduced  $B(E2;0+ \rightarrow 2+)$  values of  $^{112}\text{Sn}$  and  $^{114}\text{Sn}$  are compared with theoretical models i.e Large-Scale Shell-Model(LSSM) and Relativistic-Quasiparticle-Random-Phase Approximation (RQRPA). In figure 2 (left) the experimental  $B(E2)$  values are compared to LSSM calculations for an increasing number  $t = n$  of proton  $np$ - $nh$  excitations. The evolution of the  $B(E2)$  systematics is presented here from the pure neutron space ( $t=0$ ) to  $t = 4$  proton excitations. The  $t = 0$  curve shows a slight asymmetric maximum at  $N = 70$ , which is shifted to  $N = 68$  ( $t = 2$ ) and  $N = 66$  ( $t = 4$ ) with increasing number of  $ph$  excitations. These calculations demonstrate the important role of core-polarization effects when one breaks the  $^{100}\text{Sn}$  core and allows for proton excitations.

The experimental data are also compared with RQRPA calculations [4]. The RQRPA calculations are independent of effective charges for protons and neutrons and do not require any inert core for the  $B(E2\uparrow)$  values. It is interesting to note that the same RQRPA calculations yield quite satisfactory agreement also for the Ni and Pb isotopes [5]. In view of there being no free adjustment of parameters, the agreement with experimental data is quite good. The most important feature is the asymmetric behaviour of the  $B(E2\uparrow)$  data with respect to the mid-shell nucleus  $^{116}\text{Sn}$ .

## REFERENCES

- [1] P. Doornenbal *et al.*, Phys. Rev. C 78, 031303(R)(2008).
- [2] R.Kumar *et al.*, Phys. Rev. C 81, 024306 (2010)
- [3] A. Winther and J. de Boer, in *Coulomb Excitation*, edited by K. Alder and A. Winther, (Academic Press, New York/London, 1966)
- [4] A. Ansari Phys. Lett. B 623, 37 (2005).
- [5] A. Ansari and P. Ring, Phys. Rev. C 74, 054313 (2006).

### 5.1.8 How does projectile structure affect incomplete fusion? The case of $^{14}\text{N}+^{169}\text{Tm}$

R. Kumar<sup>1</sup>, Abhishek Yadav<sup>2</sup>, Pushpendra P. Singh<sup>3</sup>, Avinash Aggarwal<sup>4</sup>, S. Appannababu<sup>5</sup>, S. Mukherjee<sup>5</sup>, S. Muralithar<sup>1</sup>, R.Ali<sup>2</sup>, B. P. Singh<sup>2</sup>, and R. K. Bhowmik<sup>1</sup>

<sup>1</sup> Inter University Accelerator Centre, Aruna Asaf Ali Marg, New Delhi

<sup>2</sup> Physics Department, A. M. University, Aligarh (U.P.)

<sup>3</sup> INFN-Laboratori Nazionali di Legnaro, I-35020 Legnaro, Italy

<sup>4</sup>Physics Department, Bareilly College, Bareilly (U.P.)

<sup>5</sup>Physics Department, M.S. University of Baroda, Vadodara

In recent years, the study of incomplete fusion (ICF) reactions has got resurgent interest after observation of its strong influence on complete fusion (CF) processes at energies  $\approx 4-7$  AMeV [1-2]. In ref. [1-2], high quality data have been achieved at the Inter-University Accelerator Center (IUAC), New Delhi using alpha-cluster structure beams (viz;  $^{12}\text{C}$ ,  $^{16}\text{O}$ ) with medium mass target nuclei. In previous studies, the onset and strength of ICF have been studied in terms of different observables, viz; projectile energy and entrance channel mass-asymmetry. Despite the fact that the probability of ICF increases with projectile energy, we observed a significant contribution of ICF even at energies as low as 7 % above the fusion barrier. The unexpected presence of ICF at such a low energy has been justified as the consequence of high input angular momenta imparted into the system due to non-central interactions [3]. It has been observed that excess input angular momenta above the fusion limit ( $\ell_{\text{crit}}$ ) leads to projectile breakup to provide sustainable input angular momenta to the system to fuse. In this case, only a part of projectile fuses with target nucleus, while the remnant flows at forward angles with projectile velocity. Apart from the well documented existence of low energy ICF, we observed a strong contradiction on mass-asymmetry systematics presented by Morgenstern et al., [4]. As per Morgenstern's systematics, the fraction of ICF is expected to be larger for more mass-asymmetric systems. However, in a recent systematic study of ICF based on six projectile-target combinations [1], it has been found that mass-asymmetry systematics is valid only for individual projectiles but there is a significant difference in the yields with  $^{12}\text{C}$  and  $^{16}\text{O}$  beams with targets of comparable mass asymmetry. It may, however, be pointed out that all the data presented in ref. [1] is based on alpha-cluster structure beams. In addition to our recent findings, it's important to understand how does projectile structure affect ICF? As such, we have undertaken a program to carry out some conclusive experiments using  $^{13}\text{C}$ ,  $^{14}\text{N}$ , and  $^{18}\text{O}$  beams on  $^{169}\text{Tm}$  target (same as in ref.[1]), which will provide us a rich data set to settle the understanding of underlying dynamics. Present work is the first experiment in this series, where ICF strength function has been deduced for non-alpha cluster structure  $^{14}\text{N}$  beam with  $^{169}\text{Tm}$  target from near barrier energies to well above it.

These experiments have been performed at the IUAC using activation technique. The targets of  $^{169}\text{Tm}$  (100%) of thickness  $\approx 1.2-2.5$  mg/cm<sup>2</sup> were prepared by rolling. In order to trap recoiling products, each target was backed by an Al-catcher of appropriate thickness (measured by  $\alpha$ -transmission). The experimental setup used in this experiment was same as in ref. [1]. In the present experiment 12 energy points were obtained using energy degradation technique. Keeping in mind the half-lives of interest, around 10-12 hrs of irradiations were carried out with beam current  $\approx 30$  pA. The activities produced after irradiation were recorded by a pre-calibrated HPGe detector coupled to a CAMAC based data acquisition system CANDLE. The reaction residues have been identified by

their characteristic decay  $\gamma$ -lines followed by decay curve analysis. The cross sections of different reaction residues have been computed using the standard formulation [2]. The excitation functions (EFs) for 4n, p3n, p4n,  $\alpha$ 2n,  $\alpha$ 3n,  $\alpha$ 4n and  $\alpha$ 5n channels have been measured and compared with the predictions of theoretical model code PACE4[5] to check if they follow the equilibrated CN decay pattern. Since PACE4 does not take ICF into account, any enhancement of the experimental EFs from the theoretically estimated ones may be attributed to the contribution from ICF process. Fig.1 shows the experimental EFs for 4n, p3n, and  $\alpha$ 2n channels. Here, solid curves represent PACE4 predictions using systematically justified level density parameter ( $a = A/K \text{ MeV}^{-1}$ ) and a good agreement of theoretical predictions with experimental data in case of 4n and p3n channels indicates the population of these residues via CF of  $^{14}\text{N}$  with  $^{169}\text{Tm}$ .

Further, in case of alpha-emitting channels (such as  $\alpha$ 2n-channel), PACE4 under predicts experimental EFs, which points towards the onset of ICF. The alpha-emitting channels may be formed via; (a) CF of  $^{14}\text{N}$  with  $^{169}\text{Tm}$ , and/or (b) partial fusion of  $^{14}\text{N}$ . In the later case, only a fraction of projectile i.e.,  $^{10}\text{Be}$  is assumed to fuse with target nucleus to form an incompletely fused composite nucleus. While, the remnant alpha-cluster flows in forward cone as a spectator.

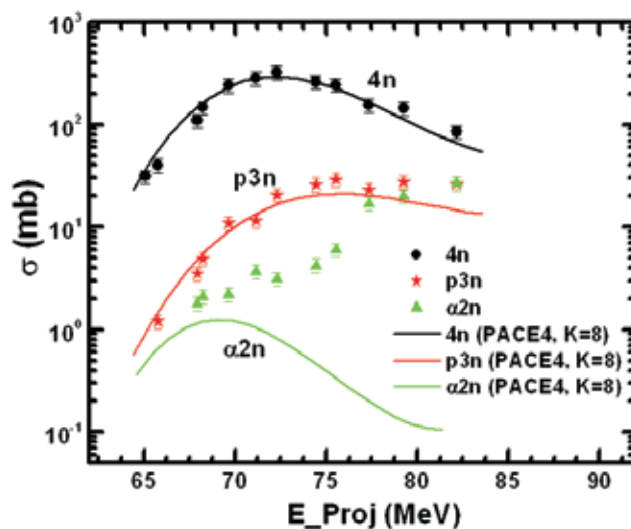


**Fig.1. Experimentally measured and theoretically calculated EFs of 4n, p3n and  $\alpha$ 2n channel**

In order to understand how ICFs show up with projectile energy and entrance channel mass-asymmetry, the ICF strength function has been deduced using same data reduction procedure as adopted in refs.[1-2]. Fig.2 (a) shows percentage fraction of ICF as a function of projectile energy for the presently studied  $^{14}\text{N} + ^{169}\text{Tm}$  system. This figure shows that (i) the presence of ICF at around barrier energies, and (ii) smooth increasing trend of ICF with projectile energies, as expected. In Fig.2 (b) the ICF strength function for the presently studied system is plotted along with several other projectile target combinations, at the same relative velocity ( $v_{\text{rel}}=0.053$ ).

From the given systematic study using data of eight projectile-target combinations, it can be inferred that the Morgenstern's systematic does not explain the experimental data achieved for different projectiles as a whole. However, the ICF fraction is found to increase with mass-asymmetry separately for each projectile. A strong projectile dependence of ICF has been revealed even in case of non- $\alpha$ -cluster structure beam.

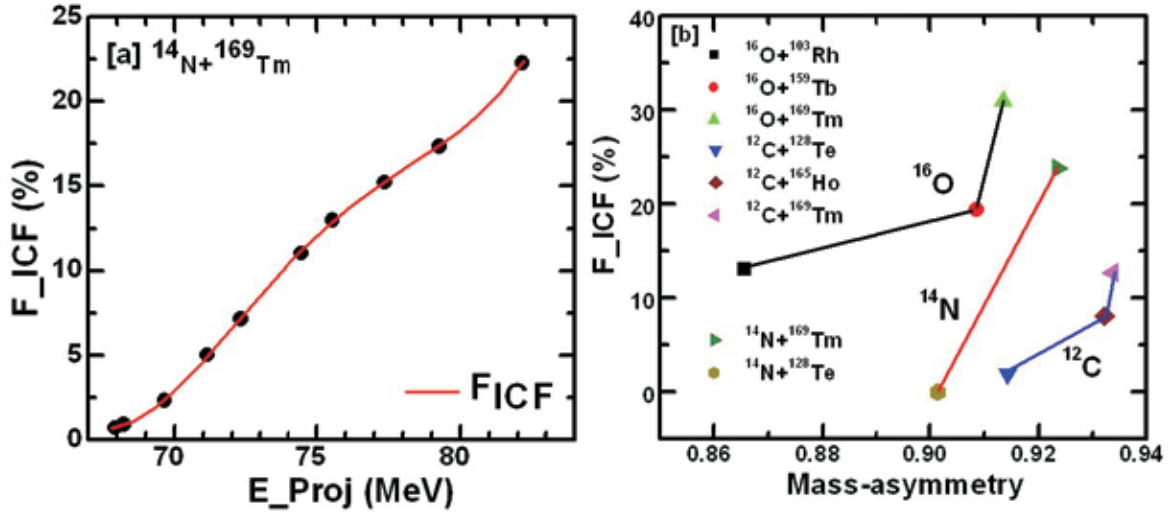


Fig.2. (a) Experimentally measured percentage fraction of ICF as a function of projectile energy and (b) entrance channel mass-asymmetry at the same  $v_{rel}$ .

## REFERENCES

- [1] Pushpendra P. Singh *et al.*, Phys. Rev. C 77, 014607 (2008), Phys. Rev. C (2010), comm.
- [2] Unnati Gupta *et al.*, Nucl. Phys. A811, 77 (2008).
- [3] Pushpendra P. Singh *et al.*, Phys. Lett. B 671, 20 (2009), Phys. Rev. C 80, 064603 (2009).
- [4] H. Morgenstern *et al.*, Phys. Rev. Lett. 52, 1104 (1984).
- [5] A. Gavron, Phys. Rev. C 21, 230 (1980).

### 5.1.9 Development of a set up to measure g factor of a nucleus using transient field technique

M.Saxena<sup>1</sup>, S.Mandal<sup>1</sup>, A.Mandal<sup>2</sup>, J.Chacko<sup>2</sup>, S.Kar<sup>2</sup>

<sup>1</sup>Department of Physics and Astrophysics, University of Delhi, Delhi

<sup>2</sup>Inter University Accelerator Centre, Aruna Asaf Ali Marg, New Delhi

Measurements of g factor or magnetic moments provide substantial information on the microscopic structure of the nuclei [1]. There are different techniques available

for measuring  $g$  factors depending on the lifetime of the state involved. It is now possible to accurately measure  $g$  factors of stable or unstable nuclei with states having lifetime of the order of several hundreds of femto seconds. As the lifetime of the states is very small, large magnetic fields of the order of several Mega Tesla will be required. As it is extremely difficult to create such fields on a macroscopic level, the transient magnetic field technique [2] is used in such cases. In this method a very high transient magnetic field is generated by the hyperfine interactions for ions traversing magnetized solids. To measure the  $g$  factor of low lifetime states we have designed and fabricated a setup based on the Transient Field Measurement Technique.

The setup essentially consists of a target chamber made of aluminium with a built in magnet and a liquid nitrogen dewar. The magnet used is C frame electromagnet which can produce a magnetic field of the order of 1000 Gauss. Super enamelled copper wire (SWG 23) has been used to build coils of the magnet. The coils are wound on a Teflon bobbin and placed over a soft iron yoke. Before building the magnet, the magnetization of the soft iron material was also investigated using a Vibrating Sample Magnetometer and was found to be appropriate. The pole pieces are designed in a special way with a slit so that the target can be placed between them and will face the maximum uniform magnetic field. The distance between the pole tips can be adjusted. Since we are using Gadolinium as a ferromagnetic material, it is necessary to keep it at liquid nitrogen temperature because of its low Curie temp. For this purpose an arrangement has been made inside the target chamber to cool the target and also the coils of the magnet. This will also minimize the beam heating of the target. The set-up design is shown in Fig. 1. It also consists of a liquid nitrogen dewar.



**Fig. 1. The  $g$  factor measurement set up.**

**Magnet Specifications:** The coils of the C – frame electromagnet have been built using super enameled (SWG 23) wire. The wire is wound over a teflon bobbin of height 80 mm. Numerous holes have been drilled on the face of the bobbin so that liquid nitrogen can reach the inner layers of the coils of the magnet and thermal equilibrium can be reached easily. The magnet has been tested and operated at room temperature and liquid nitrogen temperature conditions. A



calibration curve of current vs the magnetic field was also plotted. The results obtained are as follows:

The entire setup was first cleaned with alcohol and later then it was ultrasonically cleaned for about one hour. Then the hermetically sealed LEMO and BNC connectors were put. Then the individual parts of the setup were vacuum tested. After this the whole setup was vacuum tested. The setup will now be used in the beam line and tested with beam.

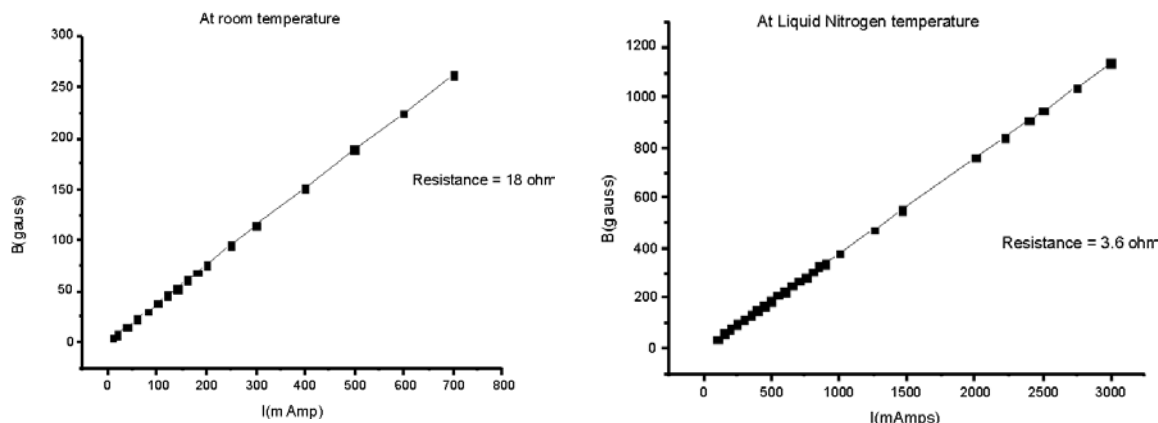


Fig. 2. Calibration curve for magnetic field vs current at room temperature.

## REFERENCES

- [1] Speidel *et al* ; Prog in Part and Nucl Physics ; 49 ( 2002)
- [2] Borchers *et al* ; Phy Rev Lett , 20 , 424

### 5.1.10 Exclusive Measurements of GDR Decay from Hot Excited $^{196}\text{Hg}$

I. Mazumdar<sup>1</sup>, N. Madhavan<sup>2</sup>, D.A. Gohe<sup>1</sup>, S. Nath<sup>2</sup>, J. Gehlot<sup>2</sup>, T. Varughese<sup>2</sup>, I. Mukul<sup>2</sup>, G. Mohanto<sup>2</sup>, P. Sugathan<sup>2</sup>, A.K. Sinha<sup>3</sup>, P.B. Chavan<sup>1</sup>

<sup>1</sup>Tata Institute of Fundamental Research, Mumbai

<sup>2</sup>Inter-University Accelerator Centre, Aruna Asaf Ali Marg, New Delhi

<sup>3</sup>UGC-DAE -CSR, Kolkata Centre, Kolkata

The studies in Giant Dipole Resonance (GDR) decay of high energy gamma rays have established itself as one of the primary tools to understand the dynamics of the hot rotating nuclei. The spectral shape and angular anisotropies of the GDR gamma

rays are expected to manifest variety of shape-phase transitions in the atomic nuclei with increasing temperature and angular momentum. The unambiguous experimental confirmation of such shape transitions will go a long way to understand the real time response of the hot and rapidly rotating nuclei to external trigger. The selection of the nuclei to be studied and the region of phase space to be probed, are guided by the predictions of theoretical calculations, both microscopic and macroscopic. It is now well established, that all mean field calculations predict a transition temperature  $T_{c1}$ , at which the nucleus, irrespective of its ground state deformation, becomes spherical and on rotation becomes oblate, rotating about its symmetry axis [1]. A series of recent calculations by Goodman have resulted in the prediction of a second transition temperature  $T_{c2}$ , where  $T_{c2} > T_{c1}$ , in some heavy nuclei [2]. According to these calculations the nucleus is expected to rotate about its symmetry axis with a prolate shape in a narrow region of the phase space demarcated by the two angular momentum dependent transition temperatures  $T_{c1}$  and  $T_{c2}$ . Our previous measurements of phase space selected GDR gamma rays from  $^{194}\text{Au}$  provided a definite indication of shape transition [3]. In particular, the reversal in the angular anisotropy pattern of the GDR gamma rays for the two different beam energies lent further credence to a possible shape transition. This provided further impetus to carry out the investigations in other neighboring nuclei. Here we report on the measurements of GDR decay in  $^{196}\text{Hg}$ .

The  $^{196}\text{Hg}$  compound nucleus was populated by bombarding a 1.1 mg/cm<sup>2</sup>, self-supporting  $^{180}\text{Hf}$  target with 120 MeV  $^{16}\text{O}$  beam from the IUAC Pelletron-LINAC facility. The high energy gamma rays were detected in the large NaI(Tl) High Energy Gamma Ray spectrometer (HIGRASP) [4] kept at 90° with respect to the beam direction and at a distance of 75 cm from the target position. The multiplicity and total energy of the low energy discrete gamma rays were measured using an array of 32 conical NaI(Tl) detectors in complete  $4\pi$  configuration. The pileup events were removed by zero cross-over technique [4] and the neutrons were rejected by time-of flight. The cosmic ray events were rejected using plastic anti-coincidence shields around the NaI(Tl) (HIGRASP). A large volume LaBr<sub>3</sub>(Ce) detector was also used to measure the high energy gamma rays. The scattering chamber and the  $4\pi$  spin spectrometer were installed on the IUAC HYRA beam line in order to detect the GDR gamma rays in coincidence with the evaporation residues detected at the focal plane of the IUAC Hybrid Recoil Analyzer (HYRA) [5]. Fig.1a shows the prompt gated multiplicity spectrum detected in coincidence with high energy gamma rays ( $> 4$  MeV) detected in HIGRASP. Fig.1b shows the multiplicity gated (fold  $> 3$ ) high energy gamma ray spectrum, detected in HIGRASP after the final data reduction. The pronounced GDR bump is visible above the straight line fitting the low energy part of the spectrum. Further analysis of the angular momentum gated spectrum is in progress and will be reported elsewhere.

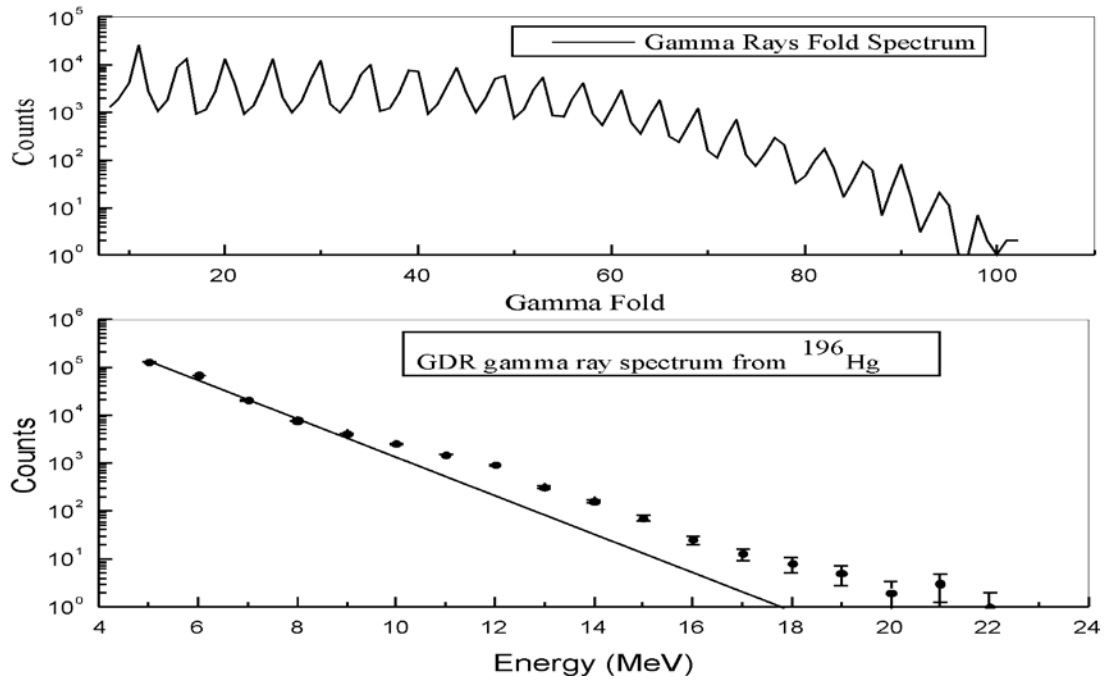


**Fig. 1a & 1b**

## REFERENCES

- [1] M. Aggarwal and I Mazumdar, Phys. Rev. C80, 024322 (2009).
- [2] A.L.Goodman, Phys. Rev. Lett. 73, 416 and 1734 (1994); A.L. Goodman, Nucl. Phys. A611, 139 (1996).
- [3] I.Mazumdar, Y.K.~Agarwal, D.A.~Gothe, U.~Kadhane, Nucl. Phys. A731, 146 (2004).
- [4] I. Mazumdar et. al. Nucl. Inst. Meth. A417, 297 (1998).
- [5] N. Madhavan et. al.

### 5.1.11 Effects of Neutron Shell Closure in Fission Dynamics

Golda K.S.<sup>1,2</sup>, A. Saxena<sup>3</sup>, V.K. Mittal<sup>2</sup>, K. Mahata<sup>3</sup>, A. Jhingan<sup>1</sup>, P. Sugathan<sup>1</sup>, V. Singh<sup>4</sup>, R. Sandal<sup>4</sup>, S. Goyal<sup>5</sup>, J. Gehlot<sup>1</sup>, A. Dhal<sup>1</sup>, B.R. Behera<sup>4</sup>, R.K. Bhowmik<sup>1</sup>, and S. Kailas<sup>3</sup>

<sup>1</sup>Inter University Accelerator Center, Aruna Asaf Ali Marg, New Delhi

<sup>2</sup>Department of Physics, Punjabi University, Patiala, Punjab

<sup>3</sup>Nuclear Physics Division, Bhabha Atomic Research Centre, Mumbai

<sup>4</sup>Department of Physics, Panjab University, Chandigarh

<sup>5</sup>Department of Physics and Astrophysics, University of Delhi

The study of fusion-fission dynamics in nucleus-nucleus collision to find optimum conditions for the synthesis of super heavy elements is an exciting topic these days. Some experiments [1] have been carried out to understand the mechanism involved in the heavy ion induced fusion reactions which show the effects of entrance and exit channel shell closure in the enhancement of fusion cross section. K. Mahata et.al [2] have tried to explain how the shell corrections at saddle point is helpful in explaining the evaporation residue cross sections and pre-scission neutron multiplicity data in mass  $\sim 200$  region. In this work we have recently carried out experiments to understand the effects of neutron shell closure in fission dynamics using neutron multiplicity measurements. The measurement of average neutron multiplicity has been extensively used to study the neutron emission as a 'Clock' for establishing the time scale for fusion-fission reactions [3].

The experiment has been carried out to study the effects of shell closure in fusion-fission dynamics using the heavy ion facility at Inter University Accelerator Centre, New Delhi. Pulsed beam of  $^{12}\text{C}$  at energies from  $\sim 62$  MeV to 81 MeV delivered by Pelletron, was bombarded on targets of  $^{194}\text{Pt}$  and  $^{198}\text{Pt}$  of thickness  $1.75 \text{ mg/cm}^2$  and  $1.45 \text{ mg/cm}^2$  respectively. The beam energies had been so adjusted that the measurements were done at the same excitation energies; 50, 55 and 60 MeV for both the systems. Fission fragments were detected by a pair of Multi-wire proportional counter (MWPC) ( $5'' \times 3''$ ) kept at  $\pm 40^\circ$  with respect to beam direction at a distance of 17 cm from target position.

24 neutron detectors (BC501) at different angles around the target chamber were used for the neutron TOF measurements. Out of these 24 detectors, 16 detectors ( $5''$  thick  $\times 5''$  diameter) were kept in reaction plan and remaining 8 detectors ( $3'' \times 5''$ ) were kept at  $15^\circ$  up and down with respect to the reaction plane. Four of the reaction plane detectors were placed at 1 meter away from the target. All the remaining detectors were placed at 2 m away from the target in a cylindrical fashion. In order to reduce gamma background beam dump was extended 4 m downstream from target and beam line was shielded with paraffin and lead bricks. The time width of the beam was continuously measured using a  $\text{BaF}_2$  detector placed near to the beam dump and it was found to be between 0.80 to 1.2 nsec at different beam energies. Discrimination between neutrons and  $\gamma$  rays was made by using pulse shape discrimination based on the zero-crossing technique and the TOF. The TOF of neutrons were converted into neutron energy by considering the prompt  $\gamma$  peak in the TOF spectrum for reference time.

The pre- and post-scission components of neutron multiplicities were obtained from the measured neutron energy spectra by using a multiple source least-square fitting procedure, using Watt expression. Three moving sources of neutrons (The CN plus two fully accelerated fission fragments) were considered while determining the multiplicities from the fits. The neutrons emitted from these moving sources were assumed to be

isotropic in their respective rest frames. Thus the measured neutron multiplicities are given as

$$\frac{d^2 M_n}{dE_n d\Omega_n} = \sum_{i=1}^3 \frac{M_{n_i} \sqrt{E_n}}{2(\pi T_i)^{3/2}} \exp \left[ -\frac{E_n - 2\sqrt{E_n E_i/A_i} \cos \theta_i + E_i/A_i}{T_i} \right]$$

where  $A_i$ ,  $E_i$ ,  $T_i$  and  $M_{n_i}$  are the mass, energy, temperature and multiplicity of each neutron emitting source  $i$ .  $E_n$  is the laboratory energy of neutron and  $\theta_i$  is the neutron detection angle with respect to the source  $i$ . Fission fragment velocities and folding angle are obtained from Viola [4] systematics for symmetric fission.

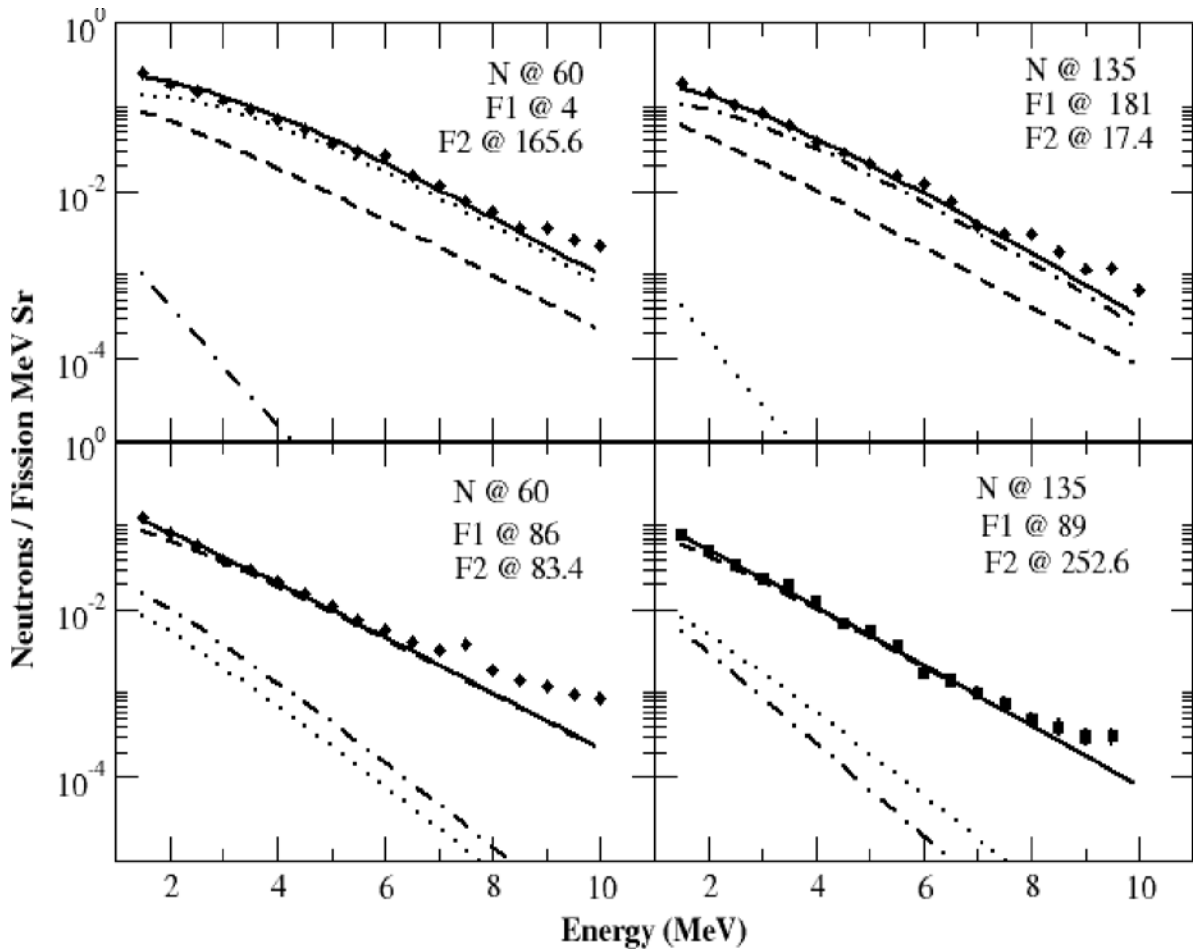


**Fig.1. Double differential neutron multiplicity spectra for  $^{12}\text{C}+^{194}\text{Pt}$  (60 MeV excitation energy) along with the fits for the pre-scission (dashed curve), post-scission from one fragment (dotted curve) and that from the other (dot dashed curve). The solid curve represents the total contribution.**

The angular acceptance of both the neutron detectors and the fission detectors were taken into account while calculating the relative angle between the neutron and the source direction in the fitting procedure. Fig.1 shows the fits to the double differential neutron multiplicity spectra at various angles for the two reactions. The pre-scission temperature has been calculated by assuming a level density parameter of  $A_{CN}/10$  MeV<sup>-1</sup> and was fixed in the moving source fits.

The experimental neutron multiplicities were compared with the statistical model predictions, PACE for the decay of a CN with a modified fission barrier and level density prescription [2]. Fig.2 compares the statistical model calculations with the experimental  $M_{pre}$  for both the systems as a function of CN excitation energy. The fission barrier height and the ratio of single particle level density parameters at saddle point to ground state are adjusted to reproduce the fission and ER cross sections measured earlier. A shell correction of 75% has been used at saddle point with respect to that at ground state in this calculation. The reduced value of pre-scission neutron multiplicity for  $^{12}\text{C}+^{198}\text{Pt}$  system compared to that of  $^{12}\text{C}+^{194}\text{Pt}$  can be accounted for the shell closure effects as the CN has 126 neutrons even though it has larger number of neutrons.

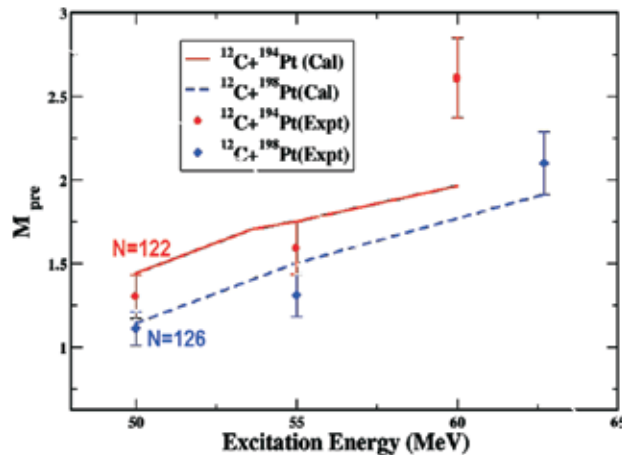


**Fig. 2. Experimental pre-scission neutron multiplicities along with the statistical model calculation results.**

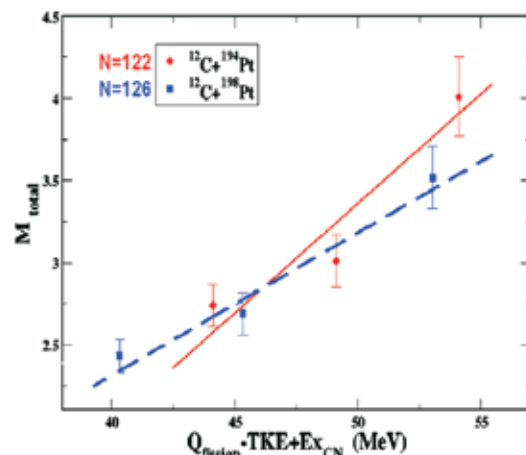


**Fig.3. Experimental total neutron multiplicities**

Fig.3 compares the total neutron multiplicities for both the systems as a function of the total available excitation energy of the fissioning system. The figure shows a smooth variation with available excitation energy with average number of neutrons emitted per MeV of available excitation energy ( $M_{total}/Ex+Q_{fiss}-TKE$ ) =  $0.097 \pm 0.013$ . This compares well within error bar with the values given in ref. 3 for similar fissility ( $\sim 0.71$ ) region.

## REFERENCES

- [1] Shrivastava, et.al, Phys. Rev. Lett. 82 (1999) 699
- [2] K. Mahata, et.al, Phys. Rev. C 74, 041301, 2006 and references therein

- [3] D. Hilscher and H. Rossner, Ann. Phys. (Paris) 17, 471 (1992); A.Saxena et al, Phys. Rev. C 49 (1992) 932
- [4] V. E. Viola, K. Kwiatkowski, and M.Walker, Phys. Rev. C 31, 1550 (1985).

### 5.2.12 Spin distribution measurement in fusion reaction $^{30}\text{Si}+^{170}\text{Er}$

G. Mohanto<sup>1</sup>, N. Madhavan<sup>1</sup>, S. Nath<sup>1</sup>, J. Gehlot<sup>1</sup>, M.B. Naik<sup>2</sup>, E. Prasad<sup>3</sup>, Ish Mukul<sup>1</sup>, T. Varughese<sup>1</sup>, A. Jhingan<sup>1</sup>, R.K. Bhowmik<sup>1</sup>, A.K. Sinha<sup>4</sup>, I.Mazumdar<sup>5</sup>, D.A. Gothe<sup>5</sup>, P.B. Chavan<sup>5</sup>, Santanu Pal<sup>6</sup>, and V.S. Ramamurthy<sup>7</sup>

<sup>1</sup>Inter University Accelerator Centre, Aruna Asaf Ali Marg, New Delhi

<sup>2</sup>Department of Physics, Karnatak University, Dharwad

<sup>3</sup>Department of Physics, Calicut University, Calicut

<sup>4</sup>UGC-DAE CSR, Kolkata Centre, 3/LB-8, Bidhan Nagar, Kolkata

<sup>5</sup>Tata Institute of Fundamental Research, Homi Bhabha Road, Mumbai

<sup>6</sup>Variable Energy Cyclotron Centre, 1/AF Bidhan Nagar, Kolkata

<sup>7</sup>National Institute of Advanced studies, Bengaluru

Angular momentum ( $\ell$ ) of Evaporation Residues (ER), produced in a fusion reaction is an interesting tool to study fusion-fission dynamics. With increase in angular momentum the fission barrier decreases and above the critical value ( $\ell_{\text{crit}}$ ) formation of Compound Nucleus (CN) becomes impossible. At higher  $\ell$ -values (well below  $\ell_{\text{crit}}$ ) fission starts playing a dominant role and restricts ER production. Spin distribution can therefore give lots of information on the reaction dynamics. ER cross section and spin distribution of  $^{16}\text{O}+^{184}\text{W}$  and  $^{19}\text{F}+^{181}\text{Ta}$ , populating the same compound nucleus (CN)  $^{200}\text{Pb}$  were studied at IUAC by Shidling [1,2]. A more symmetric target projectile combination namely,  $^{30}\text{Si}+^{170}\text{Er}$ , producing same CN, was studied in this experiment. This reaction will bring much larger  $\ell$  in the entrance channel and hence the effect of  $\ell$  in fusion-fission dynamics can be studied in a better way. Fusion and fission cross sections of this system were measured by Hinde [3]. Complete comparison of these three systems will study the entrance channel effect from different aspects.

$^{30}\text{Si}$  beam was accelerated by Pelletron + LINAC at energies 132,136, 141,146,151,156,161 and 166 MeV. Enriched  $^{170}\text{Er}$  target of thickness  $130 \mu\text{g}/\text{cm}^2$ , sandwiched in two  $^{12}\text{C}$  layers of thicknesses 23 and  $45 \mu\text{g}/\text{cm}^2$ , was placed at the target chamber of HYRA [4].  $^{170}\text{Er}$  targets were prepared at IUAC target lab using high vacuum evaporation technique. HYRA was coupled with TIFR  $4\pi$  spin spectrometer [5,6]. The spin spectrometer consists of 32 NaI detectors covering nearly  $4\pi$  solid angle. The target was put at the geometrical centre of the spin spectrometer. HYRA was operated in gas

filled mode, filled with  $^4\text{He}$  at a pressure of 0.15 torr. Out of 32 NaI detectors of spin spectrometer, 28 were used during the experiment. The ERs were detected at the HYRA focal plane with the help of a  $53 \times 53 \text{ mm}^2$  MWPC. Time of flight (TOF) technique was used to separate out beam like contamination, if any. The time taken by ER to reach focal plane was  $\sim 1.6 \mu\text{s}$ . Pulsed beam with a repetition rate of  $2 \mu\text{s}$  was taken. Two Time to amplitude converters (TAC) were set in order to separate the ER from other events. One TAC had start from MWPC anode and stop from RF TWD. The other TAC also had start from MWPC anode and stop from OR of all NaI timing signals. No significant beam contamination was observed. For detecting elastic recoils, one SSBD was placed at the target chamber at an

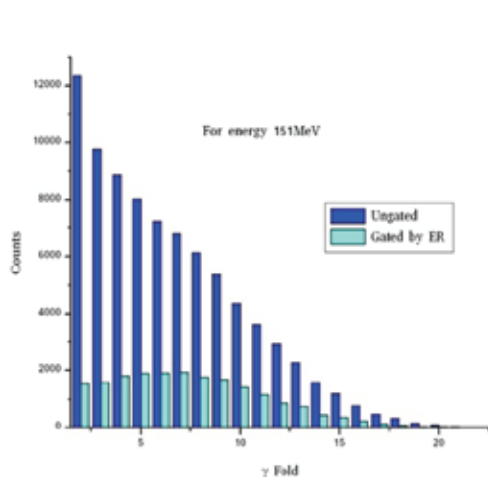


Fig. 1. Nongated and gated  $\gamma$  fold distribution

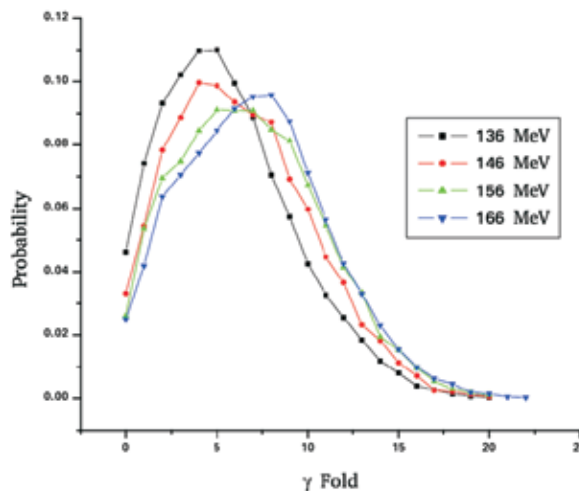


Fig. 2. ER  $\gamma$  fold distribution for different lab energies. 0<sup>th</sup> and 1<sup>st</sup> folds are extrapolated

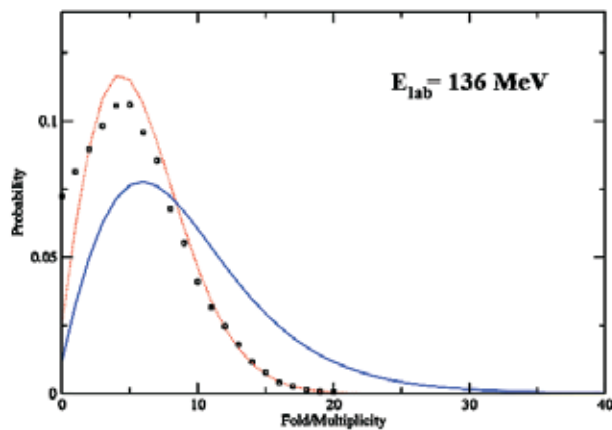


Fig. 3. Experimental (square) and fitted (red dotted)  $\gamma$  fold distribution. The continuous blue line shows corresponding multiplicity distribution.

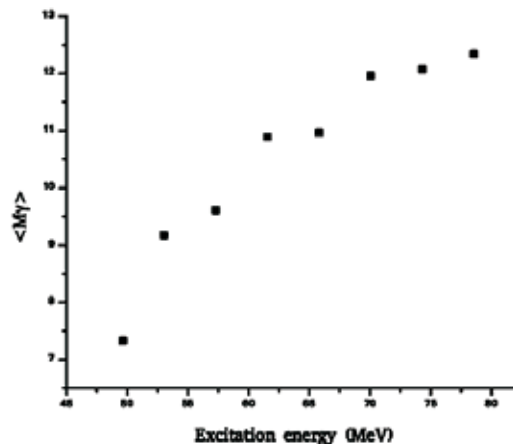


Fig. 4. Mean  $\gamma$  multiplicity plotted against excitation energy for  $^{30}\text{Si}+^{170}\text{Er}$ .

angle 25° with respect to beam direction. The  $\gamma$  rays were detected at the NaI detectors and were converted by the electronics to corresponding measured fold. To get the  $\gamma$  ray fold distribution for ER, the Time Of Flight (TOF) gate was put on the fold distribution. It was clear that lower folds were highly contaminated by events other than ER formation. After gating, other events were thrown out successfully.

The experimental folds were converted to actual  $\gamma$  multiplicity using the prescription of Van Der Worf [7]. The multiplicity was assumed to be a modified Fermi distribution of the form

$$P(M) = \frac{2M+1}{1+e^{\frac{M-M_0}{\Delta M}}}$$

where  $M_0$  and  $\Delta M$  are free parameters. These two parameters were calculated by fitting the experimental fold distribution. The  $\gamma$  multiplicity was then obtained using these parameters. The moments of the distribution were calculated for comparison.

Fig. 3 shows the experimental (square) and fitted (red dotted)  $\gamma$  fold distribution at a beam energy of 136 MeV. The continuous blue line shows corresponding multiplicity distribution. Fig. 4 shows the dependence of the average extracted multiplicity  $\langle M_\gamma \rangle$  as a function of excitation energy of the compound nucleus. Further analysis is in progress.

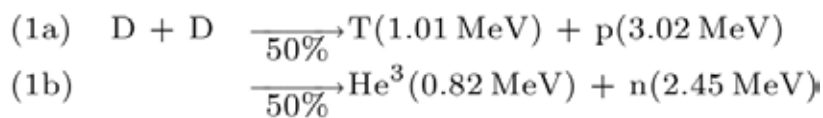
## REFERENCE

- [1] P.D.Shidlingetal., Physics Letters B 670(2008)99
- [2] P.D.Shidlingetal., Physical Review C 74(2006)064603
- [3] D.J. Hinde et al., Nucl. Phys. A 385, 109 (1982).
- [4] N.Madhavan et.al., Pramana-J.Phys.75(2010)317.
- [5] I.Mazumdar et.al., DAE Symp.onNucl.Phys.53(2008)713.
- [6] G.AnilKumar et.al., DAE Symp. on Nucl.Phys.53(2008)683.
- [7] S.Y.Van Der Werf, NIM 153 (1978)221

### 5.1.13 Measurement of neutron emission during 50 keV deuterium implantation in CaO- Pd-CaO multilayer samples

BARC, Mumbai - IUAC, Delhi collaboration

The objective of the experiment was to investigate neutron emission in d-d fusion during deuterium implantation in certain metal lattices like Palladium when the d/Pd ratio becomes close to 1. In general, d-d fusion follows the two paths:



While the Coulomb barrier for pure d-d fusion is  $\sim 200$  keV, detectable reaction rate may occur even at much lower kinetic energies  $\sim 10$  keV if there is enhancement of fusion due to the Coulomb screening in metal lattices. In this regard we irradiated a Pd metallic layer ( $\sim 2000$  Å) sandwiched between two Ca-O layers of thickness  $\sim 7500$  and  $\sim 7000$  Angstroms respectively. The total number of Palladium atoms in the layer is  $\sim 1.35 \times 10^{18}$ . The average energy of the deuterium ions entering the Pd layer was  $\sim 15$  keV with a range  $\sim 920$  Å.

Fig. 1 shows a Monte Carlo simulation of the range distribution of Deuterium ions using the SRIM-2008 software. As can be seen, more than 90% of the implanted ions are in the Pd layer of thickness 2000 Å. At 10 micro ampere current for about 10 hours of irradiation one can achieve d/Pd ratio greater than 1.0.

Deuterium ions (produced by ECR source at the LEIBF facility of IUAC) were accelerated to the required energy (e.g. 50 keV) with an average current of about 10 micro ampere at the target. The beam profile was monitored using the Beam Profile Monitors (BPM) continuously and once on a scintillating medium. The experimental set-up consisted of four large area NE213 neutron detectors placed around the scattering chamber at about 40 cm from the target. The energy threshold of  $\sim 0.5$  MeV for neutrons was kept on all four neutron detectors. A Californium source spectrum is also taken to ensure proper n-gamma discrimination. A neutron gate was put using the software and the neutron rate was monitored online.

Multi Layer (ML) Sample 2- CaO(7500)-Pd(2000)-CaO(7000)-SS(1mm)  
 – Simulation SRIM 2008

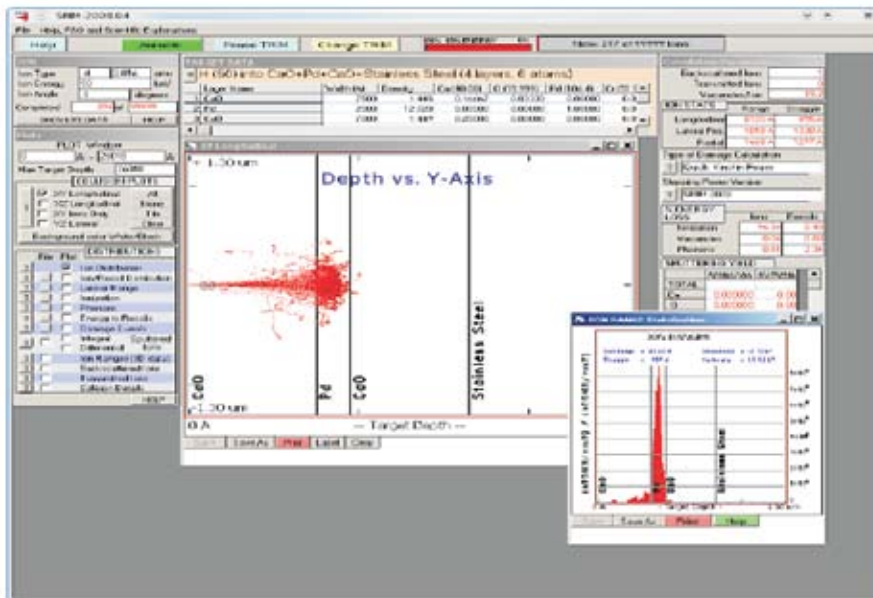
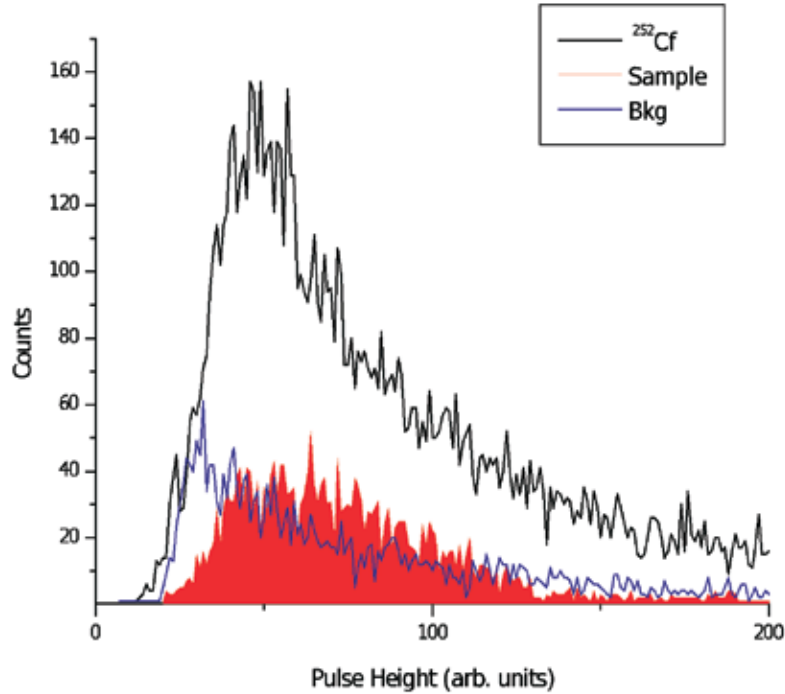


Fig. 1. Monte Carlo simulation of the range distribution in a typical multi-layer sample



**Fig. 2. Neutron gated pulse height spectrum.**

Fig. 2 shows the neutron gated pulse height spectrum for a given detector for three different counting situations, viz, the  $^{252}\text{Cf}$  source, the background and during the time of implantation. As can be clearly seen, the shape of the spectrum during deuterium implantation is quite different from the background shape, and the  $^{252}\text{Cf}$  spectrum. There is an indication of high energy neutrons, (i.e. 2.45 MeV neutrons expected from d+d reaction) produced during the irradiation. Detailed analysis is in progress.

#### **5.1.14 A study of incomplete fusion reaction dynamics in $^{12}\text{C} + ^{159}\text{Tb}$ system at $\approx 4\text{-}7$ MeV/A**

Abhishek Yadav<sup>1</sup>, Vijay R. Sharma<sup>1</sup>, Pushpendra P. Singh<sup>2</sup>, Manoj K. Sharma<sup>3</sup>, Devendra P. Singh<sup>1</sup>, Unnati<sup>1</sup>, Varinderjit Singh<sup>4</sup>, D. Singh<sup>5</sup>, R. Kumar<sup>5</sup>, B. P. Singh<sup>1</sup>, R.Prasad<sup>1</sup> and R. K. Bhowmik<sup>5</sup>

<sup>1</sup>Physics Department, Aligarh Muslim University, Aligarh

<sup>2</sup>INFN-Laboratori Nazionali di Legnaro, I-35020 Legnaro, Italy

<sup>3</sup>Physics Department, S.V.College, Aligarh

<sup>4</sup>Physics Department, Panjab University, Chandigarh

<sup>5</sup>Inter University Accelerator Centre, New Delhi

Recent studies [1-4] indicated that at low projectile energies  $\approx 4-7$  MeV/A, where complete fusion (CF) is expected to be the sole contributor, in-complete fusion (ICF) also plays an important role. In the case of ICF, to release excess input angular momenta, the projectile may break up into fragments with one of the fragments merging with the target nucleus. The main motivation of ICF studies is to explore the effect of various entrance channel parameters on reaction dynamics, such as the projectile energy, the mass asymmetry of interacting partners, the input angular momenta imparted to the system, etc. In order to study the aforementioned issues related to ICF reaction dynamics, the experiments have been performed using  $^{12}\text{C}$  beam delivered from the 15UD-Pelletron accelerator at the Inter University Accelerator Centre (IUAC), New Delhi, India. Targets of spectroscopically pure  $^{159}\text{Tb}$ , of thickness  $\approx 2$  mg/cm $^2$ , have been used. Irradiations were carried out in the General Purpose Scattering Chamber (GPSC). The activities produced after irradiation were recorded using a pre-calibrated, HPGe detector coupled to a PC through CAMAC based CANDLE software for data acquisition. The cross sections for the population of evaporation residues were determined from the observed  $\gamma$ -activity. The EFs for 9 reaction residues populated via xn ( $x=3, 4, 6$ ), pxn ( $x=3$ ) and  $\alpha$ xn ( $x=2, 4$ )  $2\alpha$ xn ( $x=2, 3, 4$ ) channels, which may be formed through CF and/or ICF, have been measured. As a representative case, the measured EFs for the residues populated via xn and pxn channels are shown in Fig.1. The EFs have also been calculated using code PACE4 [5], based on CN-model, and are found to be satisfactorily reproduced.

The measured EFs for all the  $\alpha$ -emitting channels were also compared with the statistical model calculations employing the same set of parameters as used to reproduce the CF channels. In case of  $\alpha$ xn and  $2\alpha$ xn channels the measured EFs are found to be significantly enhanced over the theoretical predictions (as shown in Fig.2). This enhancement may be attributed to the contribution from ICF-reaction process in all  $\alpha$ -emitting channels.

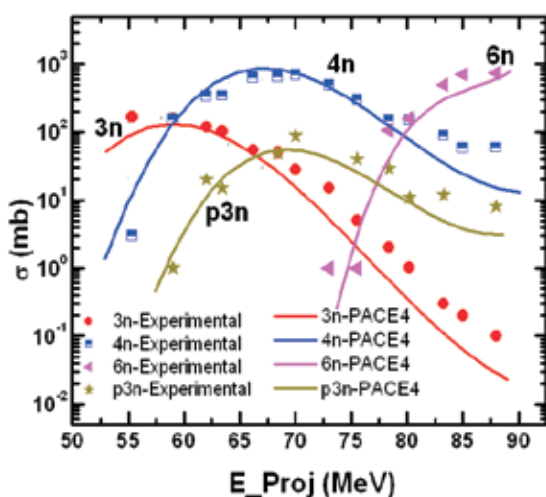


Fig.1. The experimentally measured EFs for xn ( $x=3, 4, 6$ ) and p3n-channels. The lines drawn are the calculations with best choice of parameters.

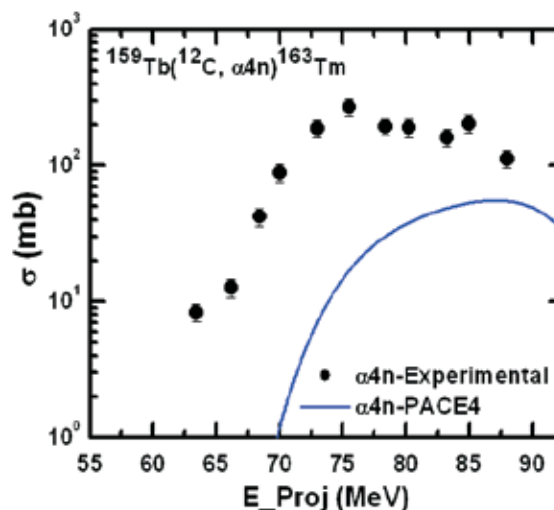


Fig.2. The experimentally measured and theoretically calculated EFs for  $\alpha$ 4n-channel.

The ICF fraction  $F_{ICF}$  has also been deduced and is found to increase with energy. A complementary experiment for the same system to study the linear momentum transfer from the projectile to the target nucleus has also been carried out at several energies to directly disentangle the CF and ICF contributions. The authors thank the Chairman, Dept. of Physics, AMU and the Director, IUAC, New Delhi, India, for providing all the necessary facilities. A.Y. thanks to the UGC for SRF, B.P.S. and R.P. thanks to the UGC & DST for financial support.

## REFERENCES

- [1] Diaz-Torres et al., Phys. Rev. C 65, 024606 (2002); Phys. Rev. Lett. 98, (2007) 152701.
- [2] M. Dasgupta et al., Phys. Rev. C70, (2004) 024606.
- [3] L. F. Canto et al., Phys. Rev. C58, (1998) 1107.
- [4] Pushpendra P. Singh et al., Phys. Lett. B671, (2009) 20; Phys. Rev. C 77, (2008) 014607.
- [5] A. Gavron et al., Phys. Rev. C 21, (1980) 230.

### 5.1.15 Study of fission fragment mass distributions for the compound nucleus $^{215}\text{Fr}$

S. Appannababu<sup>1</sup>, S. Mukherjee<sup>1</sup>, K. S. Golda<sup>2</sup>, P. Sugathan<sup>2</sup>, A. Jhingan<sup>2</sup>, E. Prasad<sup>3</sup>, D. Negi<sup>2</sup>, J. Gehlot<sup>2</sup>, P. K. Rath<sup>1</sup>, B. K. Nayak<sup>4</sup>, R. G. Thomas<sup>4</sup>, and R. K. Choudhury<sup>4</sup>

<sup>1</sup>Physics Department, Faculty of Science, The M. S. University of Baroda, Vadodara

<sup>2</sup>Inter University Accelerator Centre, Aruna Asaf Ali Marg, New Delhi

<sup>3</sup>Department of Physics, Calicut University, Calicut

<sup>4</sup>Nuclear Physics Division, Bhabha Atomic Research Centre, Mumbai

Recently the study of fusion-fission dynamics in less fissile systems is of great interest due to the observation of many interesting results. In these less fissile systems it appears that the mass relaxation is much slower than the relaxation in K degrees of freedom, which is in contradiction to heavier and highly fissile systems [1, 2]. Earlier dynamical models predict that quasi fission (QF) occurs when  $Z_p Z_T > 1600$ . However recent experimental results show evidence of QF with asymmetric systems like  $^{19}\text{F} + ^{197}\text{Au}$  ( $Z_p Z_T = 632$ ) [1]. These results makes it is very imperative to understand the relaxation mechanism of various degrees of freedom in detail, in less fissile systems. In this context it will be interesting to study the mass distributions and angular distributions for a reaction similar to the above reported system. In our earlier work, we have studied fission fragment angular distributions for the reaction  $^{18}\text{O} + ^{197}\text{Au}$  having entrance channel mass asymmetry very much similar to  $^{19}\text{F} + ^{197}\text{Au}$ . The experimental results show that complete K equilibration takes place in case of this

reaction as the angular distribution results match with theoretical predictions [3]. In order to investigate the contribution from non compound nucleus fission during mass equilibration process, we have studied the mass ratio distributions and mass angle correlation around the Coulomb barrier for the reactions  $^{18}\text{O} + ^{197}\text{Au}$  and  $^{11}\text{B} + ^{204}\text{Pb}$  which are leading to the same compound nucleus  $^{215}\text{Fr}$ .

$^{11}\text{B}$  and  $^{18}\text{O}$  beams at different energies were bombarded on enriched targets of  $^{204}\text{Pb}$ ,  $^{197}\text{Au}$  of thickness 250 and 150  $\mu\text{g}/\text{cm}^2$  respectively. Fission fragments were detected by two large area multi wire proportional counters (MWPC) placed at distances of 40 and 55 cm on the rotatable arms inside the 1.5m diameter General Purpose Scattering Chamber (GPSC). These two detectors were kept at folding angles to detect the complementary fragments in coincidence. Two Si surface barrier detectors of thickness 300 microns with a collimator of 1mm were placed at  $\pm 10^\circ$  to the beam direction, at a distance of 70 cm from the target. These detectors were used for aligning the beam and to take care that the beam was always on the center of the target. The angular calibration of the MWPC's was done on-line by collecting the elastic scattering data at an energy well below the Coulomb barrier and also offline by using a  $^{252}\text{Cf}$  source of known strength. DC beams were used in the experiment and time difference method was adopted to extract the mass ratios assuming only binary reaction processes [4]. The positions information of the fission fragments entering the detectors were obtained from the delay line read out of the MWPC wire planes. The central foil of both the MWPC's recorded the timing and energy loss signals. The position calibration (x,y) and solid angle of both the detectors were determined by taking elastic scattering data in singles mode below the Coulomb barrier. These (x,y) position information was converted to  $(\theta, \phi)$  and the time of flight information was taken from the TAC signal. Individual TDCs were used for each MWPC, with the anode as the start and four position signals by taking start signal from the anode signal of back detector and stop from the delayed anode signal from the front detector. The velocities of the fission fragments were reconstructed by using the  $(\theta, \phi)$  information with the time difference information. The time difference calibration for the studied systems was achieved by imposing the condition that the mass ratio distribution is reflection symmetric about  $M_r = 0.5$  at  $\theta_{\text{c.m.}} = 90^\circ$ . The mass distributions were extracted as mentioned in Ref. [5]. The experimentally extracted mass distribution for the two systems  $^{11}\text{B} + ^{204}\text{Pb}$  and  $^{18}\text{O} + ^{197}\text{Au}$  at the same excitation energy  $E = 55.5$  MeV are shown in Fig.1. Data analysis is under progress,

We acknowledge the financial assistance from CSIR and IUAC for the present research work. We also thank the Pelletron staff and I. Bala for their help during the experiment.

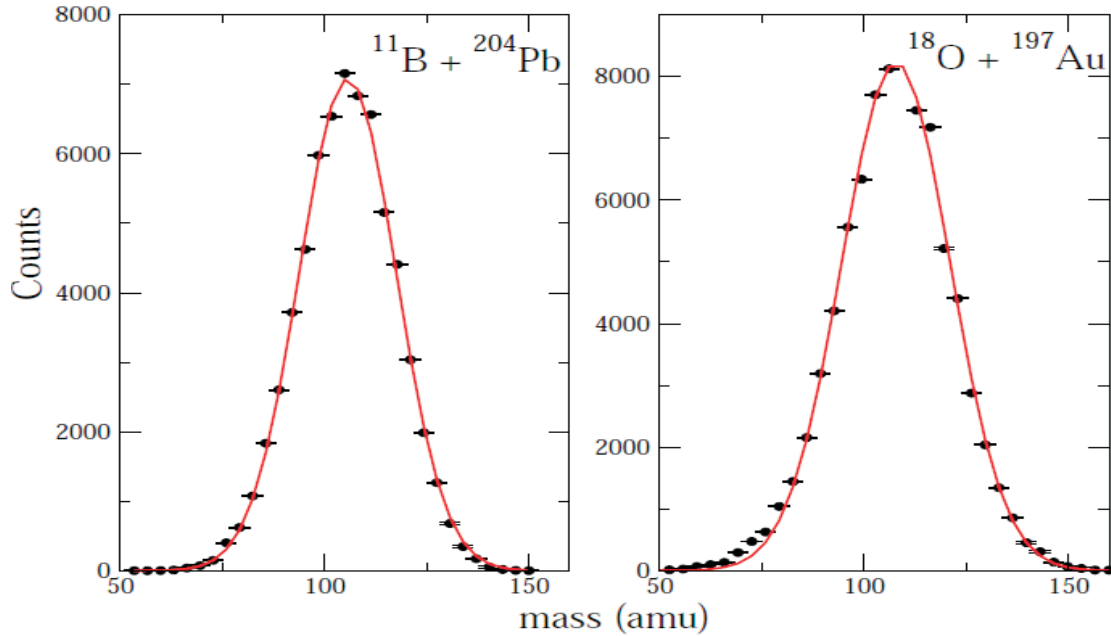


**Fig. 1. The mass distributions for  $^{11}\text{B} + ^{204}\text{Pb}$  and  $^{18}\text{O} + ^{197}\text{Au}$  at the same excitation energy  $E^* = 52.6$  MeV.**

## REFERENCES

- [1] A. C. Berriman *et al.*, Nature (London) 413, 144 (2001).
- [2] R. Tripathi *et al.*, Phys. Rev. C 71, 044616 (2005).
- [3] S. Appannababu *et al.*, Phys. Rev. C 80, 024603 (2009).
- [4] R. K. Choudhury *et al.*, Phys. Rev. C 60, 054609 (1999).
- [5] S. Appannababu *et al.*, Accepted in Phys. Rev. C (2011).

### 5.1.16 Lifetime Measurements in Nuclei of Mass 125 Region

K. Selvakumar<sup>1</sup>, Subhashri Das<sup>1</sup>, A. K. Singh<sup>1</sup>, Purnima Singh<sup>1</sup>, R. Raut<sup>2</sup>, M. Kumar Raju<sup>8</sup>, A. Goswami<sup>2</sup>, S. Muralithar<sup>7</sup>, A. Mukherjee<sup>2</sup>, U. Datta Pramanik<sup>2</sup>, G. Gangopadhyay<sup>3</sup>, Samit Bhowal<sup>4</sup>, P. Dutta<sup>5</sup>, S. Roy<sup>6</sup>, Rakesh Kumar<sup>7</sup>, R. P. Singh<sup>7</sup>, and Thomas Reddy<sup>8</sup>

<sup>1</sup>Department of Physics, Indian Institute of Technology, Kharagpur

<sup>2</sup>Nuclear and Atomic Physics Division, Saha Institute of Nuclear Physics, Kolkata

<sup>3</sup>Department of Physics, University of Calcutta, Kolkata

<sup>4</sup>Surendra Nath College, Kolkata

<sup>5</sup>Ananda Mohan College, Kolkata

<sup>6</sup>S.N.Bose National Centre for Basic Sciences, Kolkata

<sup>7</sup>Inter University Accelerator Center, Aruna Asaf Ali Marg, New Delhi

<sup>8</sup>Department of Nuclear Physics, Andhra University, Visakhapatnam

Nuclei which are lying between spherical and well-deformed region are generally known as transitional nuclei. The alignment of the valence nucleons outside the spherical <sup>114</sup>Sn core in the transitional nuclei of mass  $\sim 125$  drives the nuclei into different shapes. The shape co-existence, which occurs in the excited nuclei, is mainly due to the collective and noncollective excitations of the nucleons. The shape driving properties of the excited nucleons depends upon the position of its Fermi surface. For example, the neutron Fermi surface lying in the middle or upper part of the  $h_{11/2}$  favors oblate shape, whereas, the proton Fermi surface, which lies in the lower part of the  $h_{11/2}$  subshell, favors prolate shape.[1,2]. Recent investigations of nuclei <sup>123</sup>Cs and <sup>124</sup>Ba in this mass region shows that there is an interplay between the single-particle excitations and the collective excitations in the negative parity  $h_{11/2}$  band at high spins, which favors band termination [3,4]. The lifetime measurements in these bands will be helpful to understand the nature of band termination. The Doppler Shift Attenuation Method (DSAM) technique has been used for the lifetime measurements.

The excited states of <sup>123</sup>Cs were populated in the <sup>96</sup>Zr (<sup>32</sup>S, p4n) <sup>123</sup>Cs reaction. High spin states of <sup>124</sup>Ba were populated in the same reaction by 4n channel. The <sup>32</sup>S beam of energy 140 MeV was provided by 15UD Pelletron accelerator at Inter University Accelerator Center, New Delhi. The target used was 1mg/cm<sup>2</sup> enriched <sup>96</sup>Zr deposited on lead backing of thickness 10 mg/cm<sup>2</sup>. Gamma ray coincidence events were collected by the Indian National Gamma ray Array (INGA) spectrometer consisting of 17 Compton-suppressed HPGe detectors at the time of experiment [5]. The detectors were grouped into five rings at angles 32°, 57°, 90°, 123° and 148° with respect to the beam axis. The events were collected in the list mode by CANDLER [6], the data acquisition system, with the condition of minimum three detectors being fired at the same time.

In the offline analysis, the data were calibrated for energy and efficiency by using <sup>152</sup>Eu source. The calibrated data were sorted into symmetric 4k x 4k matrix using INGASORT [7] for the intensity measurements. For the line shape analysis an asymmetric 4k x 4k matrix was formed. Finally the lifetime values are obtained by fitting theoretical line shapes with the experimental line shapes for all the angles (57°, 90° and 148°) simultaneously using the code LINESHAPE [8].

In <sup>123</sup>Cs, lifetime values were obtained for eight transitions in the negative parity  $h_{11/2}$  band within the spin range of  $I = 27/2^-$  to  $55/2^-$ . The lifetime measurements show that the average quadrupole moment of this band is  $\sim 3.35$  eb and there is no change in nuclear structure up to spin  $55/2^-$ . This indicates that the band termination in the  $h_{11/2}$  band of <sup>123</sup>Cs could be an abrupt one. Similarly, we have carried out lifetime measurements in

the  $h_{11/2}$  band of  $^{124}\text{Ba}$ . The transition quadrupole moment obtained from the lifetime measurements shows an average value of  $\sim 4.68$  eb in the spin range  $16^+ \leq J^\pi \leq 22^+$ . The theoretical line shape fitted with the experimental line shape for the transitions of energy 955 keV and 766 keV for the angles  $57^\circ$ ,  $90^\circ$  and  $148^\circ$  are shown in Fig1.

This work was supported by the Department of Science and Technology (DST/SR/S2/HEP-09/2005), New Delhi. The financial support from the MHRD, Govt. of India is also gratefully acknowledged. The authors would like to thank the pelletron and electronics group of IUAC for their kind support during the experiment.

## REFERENCES

- [1] R. Wyss et al., Nucl. Phys. A505, 337 (1989).
- [2] A. Granderath et al. Nucl. Phys. A 597, 427 (1996).
- [3] A. K. Singh et al., Phys. Rev. C 70, 034315(2004).
- [4] Al-Khatib et al., Phys. Rev. C 74, 014305 (2006)
- [5] S. Muralithar et al., DAE Symposium on Nucl. Phys. 53, 689 (2008).
- [6] E. T. Subramaniam et al., Rev. Sci. Instr. 77, 096102 (2006)
- [7] R. K. Bhowmik et al., DAE Symposium on Nucl. Phys. 44B, 422 (2001).
- [8] J. C. Wells and N.R. Jhonson, Report ORNL-6689, 44 (1991).

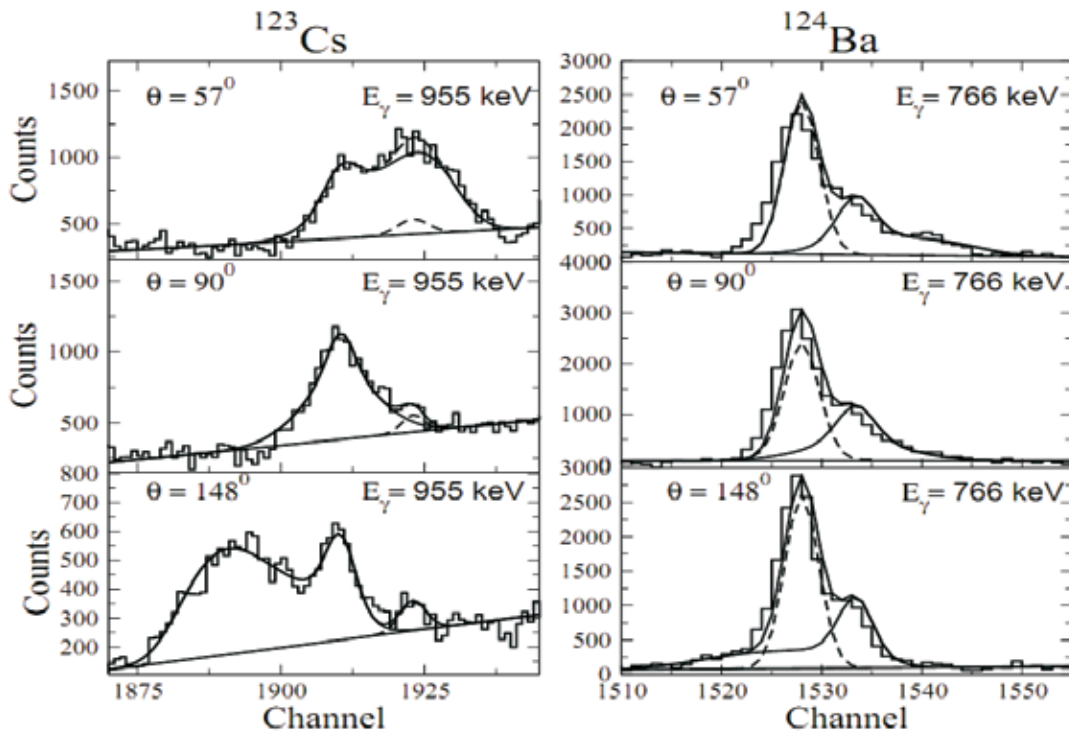


Fig.1. Theoretical line shape fitted with the experimental lineshape for the transitions 955 keV and 766keV.

### 5.1.17 Investigation of tetrahedral symmetry in nuclei

R.P. Singh<sup>1</sup>, G. de Angelis<sup>2</sup>, D. Curien<sup>3</sup>, J. Dudek<sup>3</sup>, A. Astier<sup>4</sup>, S. Aydin<sup>6</sup>, D. Bazzacco<sup>6</sup>, P. Bednarczyk<sup>9</sup>, S. Bhattacharya<sup>5</sup>, R.K. Bhowmik<sup>1</sup>, M. Ciemata<sup>9</sup>, D. D. Di Julio<sup>7</sup>, Q.T.Doan<sup>8</sup>, G. Duchêne<sup>3</sup>, E. Farnea<sup>6</sup>, C. Fahlander<sup>7</sup>, A. Gadea<sup>2,12</sup>, P. Golubev<sup>7</sup>, D. Guinet<sup>8</sup>, C.Y. He<sup>2</sup>, F. Haas<sup>3</sup>, S. Lunardi<sup>6</sup>, K. Mazurek<sup>9</sup>, D. Mengoni<sup>6</sup>, R. Menegazzo<sup>6</sup>, M. Moukaddam<sup>3</sup>, S. Muralithar<sup>1</sup>, S. Myalski<sup>9</sup>, D.R. Napoli<sup>2</sup>, C.Petrache<sup>10</sup>, F. Recchia<sup>6</sup>, E. Sahin<sup>2</sup>, O. Stezowski<sup>8</sup>, D. Tonev<sup>11</sup>, J.J. ValienteDobon<sup>2</sup>, A. Vancraeynest<sup>8</sup> and C. A. Ur<sup>6</sup>

<sup>1</sup> Inter-University Accelerator Centre, Aruna Asaf Ali Marg, New Delhi

<sup>2</sup> INFN, Laboratori Nazionali di Legnaro, Legnaro, Italy

<sup>3</sup> IPHC, Strasbourg, France

<sup>4</sup> CSNSM, Orsay, France

<sup>5</sup> Saha Institute of Nuclear Physics, Kolkata, India

<sup>6</sup> Dipartimento di Fisica and INFN, Sezione di Padova, Padova, Italy

<sup>7</sup> University of Lund, Sweden

<sup>8</sup> IPN, Lyon, France

<sup>9</sup> IFJ-PAN, Krakow, Poland

<sup>10</sup> IPN, Orsay, France

<sup>11</sup> Bulgarian Academy of Sciences, Sofia, Bulgaria

<sup>12</sup> IFIC-CSIC Valencia, Spain

In recent years a number of theoretical studies [1-9] based on the nuclear mean field have predicted high rank symmetry leading to nuclei with a tetrahedral shape. With 48 symmetry elements, this shape would mean the most symmetric shape to be discovered so far. Because of this high level of symmetry the single nucleonic spectra possess unique properties. The most important one is that the nucleonic levels are divided into three families, one of which is composed of states with the four-fold degeneracy. Among the symmetry groups used in physics only the tetrahedral (and octahedral) ones imply the above special degeneracies - all the other point-groups symmetries lead to the well known double Kramers degeneracies. Strong tetrahedral symmetry effects are predicted in nuclei to occur at nucleon numbers around 16, 20, 32, 40, 56, 58, 70, 90, 94 [2]. However, it has not yet been identified in an unambiguous way in nuclei.

Dudek et al [9] had pointed out band structures in <sup>156</sup>Gd showing tentative signatures of possible tetrahedral symmetry. To investigate these signatures we have carried out Coulomb excitation study of the <sup>156</sup>Gd nucleus. <sup>58</sup>Ni beam of 225 MeV was delivered by the LNL tandem accelerator for safe Coulomb excitation of <sup>156</sup>Gd nuclei.

The target thickness was about  $1\text{mg}/\text{cm}^2$ . An annular double sided Si strip detector called LuSiA [10] from University of Lund was used to detect the scattered nickel ions at the back angles; the angular range covered by LuSiA was about 138 to 170 degrees relative to the beam direction. The gamma transitions were measured in coincidence with the scattered nickel ions using the gamma detector array GaSp [11] at LNL. Particle-gamma and gamma-gamma matrices were formed using the scattered particle information for Doppler correction event by event.

Figure 1 shows the tentative level scheme developed based on the present study. Apart from the ground state band (GSB) negative parity odd spin (NPOS) band, negative parity even spin (NPES) band along with a beta and gamma bands have been shown. The NPES band is the one which was pointed out in reference [9] to show tentative signs of being tetrahedral in character. The last study on Coulomb excitation of  $^{156}\text{Gd}$  was reported in [12]. However, in this study no B(E1) or B(E2) for the proposed tetrahedral band was reported. Based on our preliminary analysis we had reported the B(E2)/B(E1) ratio for this band in [13]. We have extracted the intensity of the gamma lines from the particle-gamma projection and from different gates from gamma-gamma matrix for this and the other bands shown in the figure. We are now trying to do multi-step Coulomb excitation calculation using the code GOSIA [14] to determine the various matrix elements for the bands.

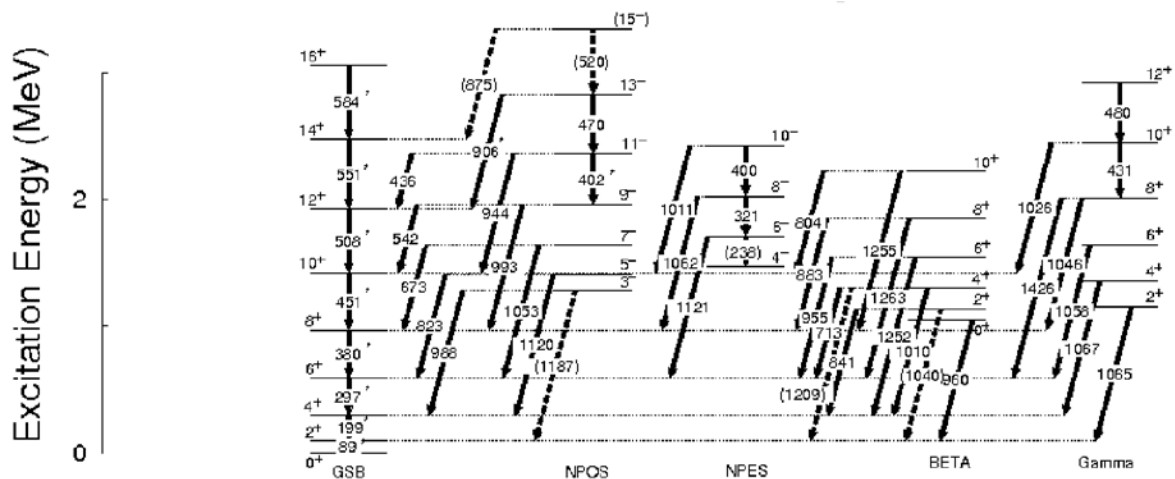


Fig. 1. Tentative level scheme of  $^{156}\text{Gd}$  based on the present analysis of Coulex data

## REFERENCES

- [1] X. Li and J. Dudek, Phys. Rev. C94 (1994) R1250
- [2] J. Dudek, A. Gozdz, N. Schunck, M. Miskiewicz, Phys. Rev. Lett. 88, 252502 (2002).
- [3] J. Dudek, A. Gozdz and D. Rosly, Acta Phys. Polon. B32, (2001) 2625.
- [4] A. Gozdz, J. Dudek and M. Miskiewicz, Acta Phys. Polon. B34, (2003) 2123.

- [5] J. Dudek, A. Gozdz and N. Schunck, *Acta Phys. Polon.* B34, (2003) 2491.
- [6] N. Schunck, J. Dudek, A. Gozdz and P. Regan, *Phys. Rev. C*69, 061305 (R) (2004).
- [7] N. Schunck and J. Dudek, *Int. Journal of Modern Phys.*, E13, (2004) 213.
- [8] N. Schunck, J. Dudek and S. Frauendorf, *Acta Phys. Polon.*, B36, (2005) 1071.
- [9] J. Dudek, D. Curien, N. Dubray, J. Dobaczewski, V. Pangon, P. Olbratowski and N. Schunck, *Phys. Rev. Lett.* 97, 072501 (2006).
- [10] <http://wwwnsg.nuclear.lu.se/lusia/>
- [11] D.~Bazzacco, in *Proceedings of the International Conference on Nuclear Structure at High Angular Momentum*, Ottawa, 1992, Report No. AECL 10613, Vol. II, p. 376
- [12] M. Sugwara et al; *Nucl. Phys.* A557(1993)653
- [13] R. P. Singh et al; *Int. Symp. on Nucl. Phys.* Vol. 54(2009)106
- [14] T. Czosnyka, D. Cline, and C. Y. Wu, *Bull. Am. Phys. Soc.* 28, 745 (1983).

## 5.2 MATERIALS SCIENCE

There were relatively fewer materials science beam line experiments in year 2010 due to the priority given to pending nuclear physics experiments in the period July to Dec. 2010.

Hydrogen profiling were performed by ERDA in Pd, Pd/Mg and Pd/Mg-Ni layers. In-situ XRD studies of Pd-silica system revealed the release of strain along with decrease in particle size of Pd nanoparticles as a result of ion irradiation. In-situ XRD of the textured ZnO thin films during swift heavy ions (SHI) irradiation revealed increase in compressive strain the films. A compressive strain is also observed in NiO thin films under SHI irradiation, investigated by in-situ XRD.

Ni-silica nanocomposite thin films were synthesized by atom beam co-sputtering with different metal fractions. The films with Ni content below 56 at.% were superparamagnetic, whereas the films with higher Ni content were metallic in nature and were ferromagnetic. Nano ripples formed at glass by atom beam, were used as template to grow Au nanowires by glancing angle deposition. Au nanoparticles embedded in carbonaceous matrix were synthesized by 150 keV Ar ion irradiation of Au film deposited on PET polymer substrate.

Embedded Si nanostructures are formed by SHI irradiation of Si rich  $\text{Si}_3\text{N}_4$  thin film. Swift ion irradiation of Ni-silica nanocomposite thin film results in elongation of Ni nanoparticles of specific size larger than ion track size in silica. The healing of CNT's was demonstrated by 55MeV C ion irradiation. It appears from the experiment that defect annealing around an annular region of ion path and the central core of the ion path creates damage. It so happen that the central damage core is small whereas the surrounding annular region is larger in case of C ions. Photoluminous(PL) of the ZnO/PMMA nanocomposite is significantly enhanced by SHI irradiation. Thin films of ZnS with wurtzite phase transforms to zinc blend phase under SHI irradiation whereas the zinc blend phase remains the same under SHI irradiation.

SHI irradiation studies have also been performed on Ag/PVA nanocomposite thin film, strontium hexaferrite nanoparticles, Co doped ZnS, ZnO,  $\text{In}_2\text{O}_3$ ,  $\text{SnO}_2$ , Co doped Ni ferrite, GaN, GaP, perovskite, polypyrrole thin films. The effect of SHI was investigated on the electrical characteristics of NPN RF power transistors.

A conference on 'Swift heavy ions in materials engineering and characterization' was organized in October 2010. There were twenty six invited talks out of which twelve were from foreign scientists. The proceedings of the conference will be published in international journal 'Radiation effects and defects in solids', after refereeing of the submitted papers. It was decided in a meeting with foreign experts that such a conference should be organized at alternate years at international level and there should be a school on basics of ion beams in materials science before the conference.

### 5.2.1 The effects of Ni and Mg<sub>2</sub>Ni interlayer on hydrogenation properties of Pd sandwiched Mg films

Pragya Jain<sup>1</sup>, Ankur Jain<sup>1</sup>, Devendra Vyas<sup>1</sup>, S. A. Khan<sup>2</sup>, I.P.Jain<sup>1</sup>

<sup>1</sup>Centre for Non-Conventional Energy Resources, University of Rajasthan, Jaipur

<sup>2</sup>Inter University Accelerator Centre, Aruna Asaf Ali Marg, New Delhi

Magnesium (Mg) based materials have attracted extensive attention for application as light weight hydrogen storage materials in the further hydrogen economy. This is due to the high hydrogen storage capacity (7.6wt% of MgH<sub>2</sub>) of the material coupled with light weight, low cost and abundance on earth crust [1-2]. Addition of Ni to Mg leads to the formation of Mg-Ni alloys like Mg<sub>2</sub>Ni. Furthermore, Ni also assists in dissociation of hydrogen molecules present in the environment. Thus, the formed H atoms diffuse into the solid and reacts with the metal atoms to form MgH<sub>2</sub> and Mg<sub>2</sub>NiH<sub>4</sub>. In the present work, we investigate the effect of Ni and Mg<sub>2</sub>Ni interlayer on the hydrogen storage capacity of Mg thin films sandwiched between Pd layers. The variation in the hydrogen content has been studied using Elastic Recoil Detection Analysis (ERDA). The structural and morphological changes are studied via X-Ray Diffraction and Atomic Force Microscope respectively.

Three samples (i) Pd/Mg/Pd (ii) Pd/Ni/Mg/Pd and (iii) Pd/Mg<sub>2</sub>Ni/Mg/Pd with total thickness of 200nm were deposited for the H storage studies.

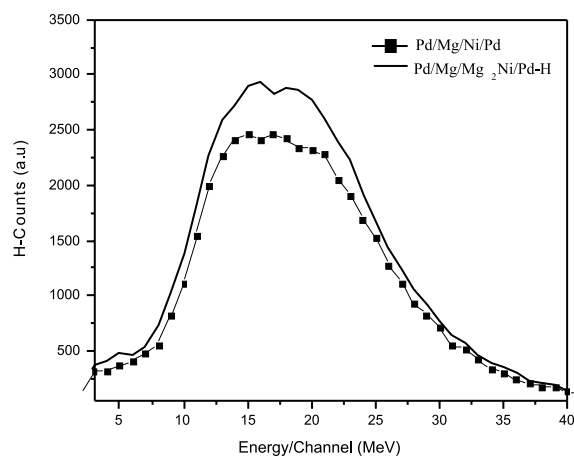


**Fig.1. ERDA spectra of hydrogenated Pd/Mg/Ni/Pd (dotted line) and Pd/Mg/Mg<sub>2</sub>Ni/Pd (solid line) film taken at 1<sup>st</sup> minute of ERDA measurement**

The deposited samples were exposed to hydrogen gas at 2bar pressure and 150°C temperature for 2hrs. Three cycles of hydrogen absorption/desorption were performed to ensure complete hydrogenation of the films. The structural characterizations of the as-deposited and hydrogenated samples were studied by GIXRD technique. After hydrogenation, Elastic recoil detection analysis (ERDA) measurements were performed with 120MeVAg<sup>9+</sup> beam to determine the aerial concentration of hydrogen ( $N_H$  in atoms cm<sup>-2</sup>).

The ERDA spectrum of hydrogenated Pd/Mg/Ni/Pd and Pd/Mg/Mg<sub>2</sub>Ni/Pd films taken during the first minute of the ERDA measurements is shown in Fig.1 in which the area under the hydrogen recoil spectra is used to obtain the hydrogen concentration  $N_H$  (atoms/cm<sup>2</sup>) in the samples at a particular time during experiment. The amount of hydrogen absorbed by the films  $N_H$  under 150°C and 2bar H<sub>2</sub> pressure is calculated for different ion doses. Fig. 2(a) and (b) represents the plot of  $N_H$  atoms/cm<sup>2</sup> versus incident ion fluence (ions/cm<sup>2</sup>) after hydrogenation for both the films. The decrease in the hydrogen content is due to H loss on ion irradiation during ERDA analysis.

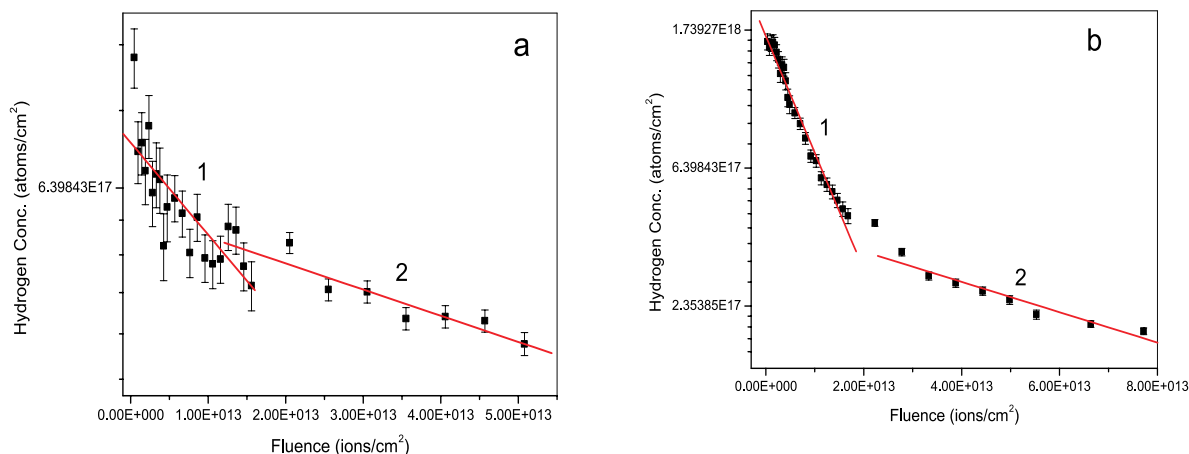


**Fig.2. Variation of hydrogen concentration with fluence of Ag<sup>9+</sup> 120 MeV ion beam irradiation on hydrogenated (a) Pd/Mg/Ni/Pd and (b) Pd/Mg/Mg<sub>2</sub>Ni/Pd films. Solid lines (red) are linear fits of region 1 and 2 (see text). Error bars show statistical error in the calculated regions.**

This study shows the effect of Ni and Mg<sub>2</sub>Ni layer addition on the hydrogen storage properties of Pd sandwiched Mg thin films which after deposition are submitted to thermal treatment under 2 bar H<sub>2</sub> pressure at 150°C for 2 hrs to promote metal to hydride phase transition. XRD studies supported by ERDA data shows the formation of MgH<sub>2</sub> and Mg<sub>2</sub>NiH<sub>4</sub> phases with 1.68x10<sup>18</sup> hydrogen atoms/cm<sup>2</sup> in Mg/Mg<sub>2</sub>Ni film as compared to Mg<sub>2</sub>NiH<sub>4</sub> phase with 7x10<sup>17</sup> hydrogen atoms/cm<sup>2</sup> in Mg/Ni film. We suggest that under given temperature conditions only a small amount of hydrogen absorbing Mg<sub>2</sub>Ni phase is formed at Mg/Ni interface of Pd/Mg/Ni/Pd system, while a large amount of Ni remains unreacted and Mg reacts with Pd to form Mg<sub>5</sub>Pd<sub>2</sub> alloy. This may be the possible reason responsible for low hydrogen content in this system.

## REFERENCES

- [1] A.Zaluska, L. Zaluski, J.O. Ström-Olsen, Applied Physics A 72(2001)157-165.
- [2] M. Zhu, H. Wang, L.Z. Ouyang, M.Q. Zeng, Int. Journal of Hydrogen Energy 31 (2006) 251.
- [3] W. Lohstroh, R. J. Westerwaal, B. Noheda, S. Enache, I. A. M. E. Giebels, B. Dam, and R. Griessen, Physical Review Letters 93 (2004) 197404.

## 5.2.2 Hydrogen absorption study of Pd/Mg thin films using elastic recoil detection analysis with 120 MeV $^{107}\text{Ag}^{+9}$ ions

Yogendra K. Gautam<sup>1,2</sup>, Amit K. Chawla<sup>1</sup>, Rajan Walia<sup>1</sup>, Saif A. Khan<sup>3</sup>, R.D. Agrawal<sup>2</sup> and Ramesh Chandra<sup>1</sup>

<sup>1</sup>Nano Science Laboratory, IIC, Indian Institute of Technology, Roorkee

<sup>2</sup>Dept. of Met. & Mat. Engineering, Indian Institute of Technology, Roorkee

<sup>3</sup>Inter-University Accelerator Centre, Aruna Asaf Ali Marg, New Delhi

Hydrogen storage in metallic thin films in the form of metal hydride has a great potential to solve the hydrogen storage challenges. Mg is a highly interesting material as pure Mg absorbs hydrogen with high gravimetric density (7.6 wt %) [1-3]. In the present work the exsitu study on structural and hydrogen storage properties of Pd-capped Mg thin films have been investigated. The nano structured Pd-capped Mg thin films have been prepared by DC magnetron sputtering on glass substrate. Hydrogenation was carried out with hydrogen gas (purity: 99.99 %) in a custom built chamber (Excel Instruments, India). The samples were kept there for 12 hrs at different temperatures (100-300°C) so that the hydrogenation (annealing in hydrogen atmosphere) of Pd/Mg films takes place by absorption of hydrogen. After annealing all samples were cool down to room temperature to conduct structural and ERDA studies. The as deposited and hydrogenated samples have been characterized by XRD and FE-SEM.

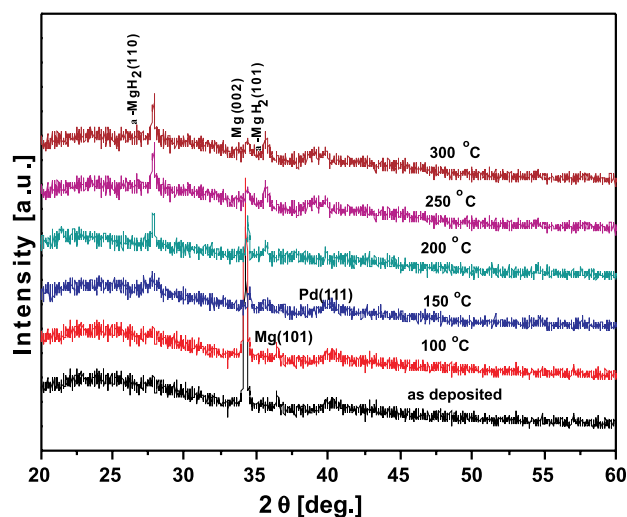


Fig. 1. XRD patterns of as deposited and hydrogenated samples

From Fig.1, it is observed that the as deposited polycrystalline Pd/Mg film shows major XRD peak corresponding to a hexagonal closed packed (hcp) structure for Mg with dominant orientation at 34.36° along (002) plane and fcc-Pd along (111) at 40.29°. In all the

hydrogenated samples  $\alpha$ -MgH<sub>2</sub> magnesium hydride phase was found to present however a small amount of Mg still remains in the samples. The dominant peak of tetragonal  $\alpha$ -MgH<sub>2</sub> (110) was observed at 27.83° in all hydrogenated samples. The peak intensity of  $\alpha$ -MgH<sub>2</sub> (110) increases with temperature up to 250°C, which suggests that hydrogen absorption enhances with temperature up to certain limit [4, 5]. The saturation of hydrogen absorption has been observed above 250°C as peak intensity of  $\alpha$ -MgH<sub>2</sub> (110) for 300°C was approximately same as for 250°C. The Peaks at 35.68° can be indexed as  $\alpha$ -MgH<sub>2</sub> (101), while the  $\alpha$ -MgH<sub>2</sub> (200) one is marked as fcc-Pd (111) (Fig.1). Hydrogen content in as deposited and hydrogenated samples have been measured by reliable elastic recoil detection analysis (ERDA) using following relation [6]:

$$Y_H = N_p N_t \left( \frac{d\sigma}{d\Omega} \right)_R \Omega / \sin \alpha$$

where hydrogen concentration  $N_t$  is in atoms /cm<sup>2</sup> In the above relation  $N_p$  is the number of incident ions,  $\Omega$  is the solid angle subtended by the detector,  $\alpha$  is the tilt angle of the

sample with respect to ion beam direction and  $\left( \frac{d\sigma}{d\Omega} \right)_R$  is the Rutherford recoil cross section for H in laboratory frame. The  $Y_H$  defined is the area under H recoil peak. The elemental H content in as deposited and hydrogenated samples was analyzed by using 120 MeV <sup>107</sup>Ag<sup>+9</sup> ions. The incident ion current was about 12nA which is equivalent to 1.22×10<sup>11</sup> ions/ second and the size of the beam spot was about 1mm<sup>2</sup> in diameter.

H content (arial density) was measured to be 6.08×10<sup>15</sup> atoms/cm<sup>2</sup>, 4.82×10<sup>16</sup> atoms/cm<sup>2</sup>, 1.36×10<sup>17</sup> atoms/cm<sup>2</sup>, 4.26×10<sup>17</sup> atoms/cm<sup>2</sup> and 4.30×10<sup>17</sup> atoms/cm<sup>2</sup> at temperature 100°C, 150°C, 200°C, 250°C and 300°C respectively. The temperature dependent hydrogen content in the thin film samples had been estimated by ERDA study in which the H content in Pd/Mg was found increase with temperature up to 250°C. Saturation hydrogen absorption had been observed at 250°C among all studied samples. The error in ERDA (Elastic Recoil Detection Analysis) measurement is within ± 2.5 %.

## REFERENCES

- [1] Huiberts JN, Griessen R, Rector JH, , Wijngaarden RJ, Dekker JP, Groot DG de, Koeman NJ. Nature 1996;380:231-234.
- [2] Alefeld G, Volkl J. Hydrogen in Metals. Topics in Applied Physics. Springer, Berlin 1978.
- [3] Sankituna B, Lamari- Darkmim F, Hersher M. Int. J. Hydrogen Energy 2007;32:121-11214.
- [4] Schlapbach L, Osterwalder J, Riesterer T. J Less Common Met 1984;103:295-297.
- [5] Hjort P, Krozer AB, Kasemo. J Alloys Compd 1996;234:11-16.
- [6] Jain IP, Babita Devi, Sharma P, Williamson A, Vijay YK, Avasthi DK, Tripathi A. Int. J. Hydrogen Energy 2000;25:517-521

### 5.2.3 Study of the structural modifications induced by ion irradiation in Pd-SiO<sub>2</sub> nanocomposite using insitu X-ray diffractometer

P. K. Kulriya<sup>1,2</sup>, B. R. Mehta<sup>2</sup>, D. C. Agarwal<sup>1</sup>, V.N.Singh<sup>2</sup>, D.K.Avasthi<sup>2</sup>

<sup>1</sup>Department of Physics, Thin Film Laboratory, IIT, New Delhi

<sup>2</sup>Inter-University Accelerator Centre, Aruna Asaf Ali Marg, New Delhi

Metallic nanostructures especially of Palladium are extensively studied due to their wide range of applications as a hydrogen sensor [1, 2], magnetic storage media [3] and catalyst etc. Ion irradiation is an unique tool for engineering density of defects, structural phase transformation, surface and interface modification, and for creation of desired structure in a controlled manner because of the non- equilibrium process of interaction and smaller dimension of the perturbed volume. A review article on the effect of ion and electron beam on the nano-structured materials such as semiconductor and metal nanoclusters and nanowires, nanotubes and fullerenes is reported by Krasheninikov et al [4]. The fine structure study in the ion track created by 27 MeV Au and 1.43 GeV Xe ions in the amorphous silica by small angle x-ray scattering revealed the ion track is consisting of a core with significant density deficit surround by a shell of higher density [5]. Ion beam can also be used for fabrication of well aligned nanorods of Au encapsulated in silica films on irradiation with 110 MeV Br [6]. The insitu x-ray diffraction (XRD) demonstrated the growth of Au nanoparticle embedded in the silica matrix on 90MeV Ni ion irradiation [7]. We have reported an application of ion irradiation for enhancement of ferromagnetism in Pd nanoparticle embedded in the carbon matrix [3]. The possible reason of the magnetism is the strain induced by the ion irradiation. Other than strain, there are many factors related to crystal structure of the material such that point defect, line defect and alternation of coordination number, structural transformation etc which decide the ferromagnetic behavior of the Pd. Therefore, it is desirable to do a systematic insitu studies on the structural modification induced by heavy ion irradiation. We report the

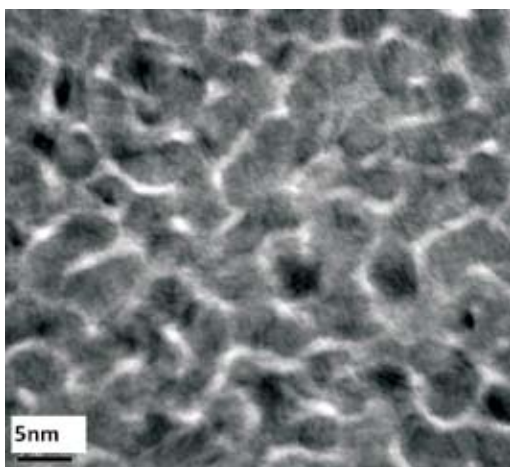


Fig. 1. HRTEM image of the Pd-SiO<sub>2</sub> nanocomposite

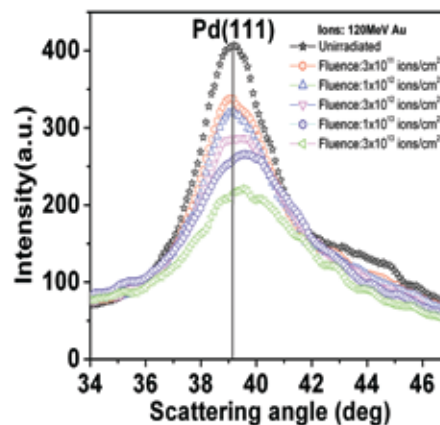


Fig. 2. Insitu XRD spectra of the Pd-silica nanocomposite when irradiated with 120 MeV Au. The amorphization induced by ion irradiation is observed.

structural modifications induced by ion irradiation in the Pd nanoparticle embedded in the silica matrix using the insitu XRD analysis.

The polycrystalline Pd nanoparticles embedded in the SiO<sub>2</sub> matrix were synthesized by the atom beam sputtering setup. The concentration of the Pd in the silica was about to 60 at. % as confirmed by the Rutherford backscattering spectroscopy. The particle size of the Pd was measured by high resolution transmission electron microscopy (HRTEM) which revealed the measured size is about to 4.8nm (Fig 1). The nanocomposite thin film (~100 nm thick) of silica having Palladium nanoparticles were irradiated with 120 MeV Au ions in the vacuum chamber (~ 10<sup>-5</sup> torr) of in-situ XRD set up. The ion fluences were varied in the range of 3x 10<sup>11</sup> to 3x 10<sup>13</sup> ions/cm<sup>2</sup> using 15UD Pelletron accelerator at Inter University Accelerator Centre (IUAC) New Delhi. Fig 2 shows the XRD spectra of pristine as well irradiated Pd-silica nanocomposite, measured using scintillation detector with step size of 0.02°/step. The XRD spectrum of the pristine sample show that the modified fcc structure of the Pd. It may be results of the strain (~2.48%) induced in the Pd nanoparticle by its nano-dimension and/or due to some matrix effect. It also indicates that Pd nanoparticle partly amorphise on ion irradiation. From XPS analysis, it is observed that there is weak interaction between Pd and silica which may leads to release in the strain induced by the matrix on irradiation. Detailed Analysis is in progress.

## REFERENCES

- [1] Pulse-like hydrogen sensing response in Pd nanoparticle layers, Manika Khanuja, Deepak Varandani and B.R. Mehta, Applied Physics Letters, 101 (2007) 124312
- [2] Nanotracks as transport routes for enhanced and reversible hydrogen diffusion in SHI irradiated Pd-Pr layers, S. Kala, B.R. Mehta, S.A. Khan and D.K. Avasthi. Applied Physics Letters, 90, 153121 (2007)
- [3] P. K. Kulriya, B. R. Mehta, D. K. Avasthi, D. C. Agarwal, P. Thakur, N. B. Brookes, A. K. Chawla, and R. Chandra, Applied Physics Letters, 96 (2010) 053103
- [4] A.V. Krashennikov and K. Nordlund, Journal of Applied Physics 107 (2010) 071301
- [5] P. Kluth, C. S. Schnohr, O. H. Pakarinen, F. Djurabekova, D. J. Sprouster, R. Giulian, M. C. Ridgway, A. P. Byrne, C. Trautmann, D. J. Cookson, K. Nordlund, and M. Toulemonde, Physics Review Letters 101 (2008) 175503
- [6] Koichi Awazu, Xiaomin Wang, Tetsuro Komatsubara, Jun Watanabe, Yuki Matsumoto, Shin'ichi Warisawa and Sunao Ishihara, Nanotechnology 20 (2009) 325303
- [7] Y. K. Mishra, D.K. Avasthi, P.K. Kulriya, F. Singh, D. Kabiraj, A. Tripathi, J. C. Pivin, I.S Bayer, A. Biswas, Applied Physics Letters, 90 (2007) 073110

### 5.2.4 Origin of swift heavy ion induced stress in textured ZnO thin films: An *in situ* X-ray diffraction study

Fouran Singh<sup>1</sup>, P. K. Kulriya<sup>1</sup> and J. C. Pivin<sup>2</sup>

<sup>1</sup>Inter-University Accelerator Centre, Aruna Asaf Ali Marg, New Delhi

<sup>2</sup>CSNSM, Bâtiment 108, 91405 Orsay Campus, France

In the last few years, ZnO based nanostructures has attracted much attention and research activities in view of their potential applications [1], such as the short wavelength electro-optical devices, lasers, white light emitting devices, spintronic devices and solar cells. The study of strain in textured films is of considerable importance for understanding the response of dilute magnetic semiconductor devices, as the strain or stress in the films can tailor the magnetic and optical properties to a very large extent. As a matter of fact, a lot of studies are reported on the strain or stress effects on properties of ZnO films, but to the best of our knowledge hardly any study exists on their manipulation. Swift Heavy Ion (SHI) irradiation is a very efficient means for modifying the structural and optical properties of materials in a narrow zone along its trajectory. Therefore, *in situ* X-ray diffraction (XRD) measurements were carried out during ion irradiation at incremented fluences under 120 MeV Ag<sup>+9</sup> ions on the textured ZnO films grown by pulsed laser deposition technique. In this study [2], the issue of stress is addressed in view of its strong implications on origin of ferromagnetism in oxide materials such as ZnO. A systematic induction of compressive stress in the textured ZnO film by swift heavy ion irradiation is demonstrated. The origin of the stress is attributed to the strong density of defects like dislocations at the grain boundaries created by dense electronic excitations.

## REFERENCES

- [1] U. Ozgur, Y.I. Alivov, C. Liu, A. Teke, M.A. Reshchikov, S. Dogan, V. Avrutin, S.J. Cho and H. Morkoc, A comprehensive review of ZnO materials and devices, J. Appl. Phys. 98 (2005) 041301-103.
- [2] Fouran Singh, P.K. Kulriya and J.C. Pivin, Solid State Communications 150 (2010) 1751-1754.

### 5.2.5 An *in situ* X-ray diffraction study of 120 MeV Au ion irradiation induced modification of microstructure in NiO thin film

P. Mallick<sup>1,4</sup>, B.N. Dash<sup>2,4</sup>, P.K. Kulriya<sup>3</sup>, D.C. Agarwal<sup>3</sup>, D.K. Avasthi<sup>3</sup>, D. Kanjilal<sup>3</sup>  
and

N.C. Mishra<sup>4</sup>

<sup>1</sup>Department of Physics, North Orissa University, Baripada

<sup>2</sup>Department of Physics, Salipur College, Salipur

<sup>3</sup>Inter-University Accelerator Center, Aruna Asaf Ali Marg, New Delhi

<sup>4</sup>Department of Physics, Utkal University, Vani Vihar, Bhubaneswar, Orissa

NiO thin film of thickness 300 nm was deposited by pulsed laser deposition method as described elsewhere [1]. The modification of the microstructure of the film under 120 MeV Au ion irradiation was studied by *in situ* X-ray diffraction at 300 K. The pristine film was textured along <111>. Ion irradiation led to increase of XRD peak intensity up to a fluence of  $3 \times 10^{11}$  ions cm<sup>-2</sup>, beyond which it decreased monotonically up to the

highest fluence ( $1 \times 10^{13}$  ions  $\text{cm}^{-2}$ ) used in the present study. Irradiation by 120 MeV Au ions thus improved the crystalline quality of the film up to the fluence of  $3 \times 10^{11}$  ions  $\text{cm}^{-2}$  and suppressed the crystalline volume fraction thereafter. The electronic energy loss,  $S_e$  ( $\sim 31.79$  keV  $\text{nm}^{-1}$ ) of 120 MeV Au ions in NiO is higher than the threshold  $S_e$  ( $\sim 30$  keV  $\text{nm}^{-1}$  [2]) for columnar track formation. Each ion is therefore expected to form a columnar track along its path and suppress the crystalline volume fraction. The increase of XRD peak intensity in the low fluence regime however indicates that in addition to track formation, the thermal spike created by the swift heavy ion anneals out some of the preexisting defects. At higher fluences, the volume fraction of the amorphized latent tracks becomes significant. The crystalline volume fraction thus decreases exponentially with ion fluence following the Poisson's law [3]. The diameter of the ion tracks was found to be  $\sim 5$  nm by fitting the integrated intensity of the  $\langle 111 \rangle$  XRD peak vs. fluence to Poisson relation. The low density of the material in the track region is expected to produce radial compressive strain in the crystalline matrix around the ion track. The generation of compressive stress is reflected in the continuous shift of XRD peak towards higher angles with increasing ion fluence. The lattice parameter extracted from the line position showed an exponential decrease with increasing ion fluence. The diameter of the strained region was estimated to be  $\sim 15$  nm by fitting the variation of the lattice parameter with fluence to the Poisson's law. Irradiation of 120 MeV Au ion in NiO thin films has thus resulted into annealing of defects, creation of columnar ion track and a strained matrix around each ion track.

## REFERENCES

- [1] P. Mallick, Chandana Rath, Jai Prakash, D.K. Mishra, R.J. Choudhary, D.M. Phase, A. Tripathi, D.K. Avasthi, D. Kanjilal and N.C. Mishra, Nucl. Instrum. Methods Phys. Res. B 268, 1613 (2010)
- [2] B. Schattat, W. Bolse, S. Klaumünzer, I. Zizak and R. Scholz, Appl. Phys. Lett. 87, 173110 (2005).
- [3] N. Ishikawa, S. Yamamoto and Y. Chimi, Nucl. Instrum. Methods Phys. Res. B 250, 250 (2006).

### 5.2.6 Ion beam–induced shaping of Ni nanoparticles embedded in a silica matrix: From spherical to prorate shape

Hardeep Kumar<sup>1</sup>, Santanu Ghosh<sup>1</sup>, Devesh Kumar Avasthi<sup>2</sup>, Debdulal Kabiraj<sup>2</sup>, Arndt Mücklich<sup>3</sup>, Shengqiang Zhou<sup>3</sup>, Heidemarie Schmidt<sup>3</sup> and Jean-Paul Stoquert<sup>4</sup>

<sup>1</sup>Nanotech Laboratory, Department of Physics, IIT, Delhi, New Delhi

<sup>2</sup>Inter University Accelerator Centre, Aruna Asaf Ali Marg, New Delhi

<sup>3</sup>Institute of Ion Beam Physics and Materials Research, Helmholtz-Zentrum Dresden-Rossendorf, P.O. Box 510119, 01314 Dresden, Germany

<sup>4</sup>Institut d'Electronique du Solide et des Systèmes, 23 rue du Loess, BP 20 CR, 67037 Strasbourg Cedex 2, France

Present work reports the elongation of spherical Ni nanoparticles (NPs) parallel to each other, due to bombardment with 120 MeV Au<sup>+9</sup> ions at a fluence of  $5 \times 10^{13}$  ions/cm<sup>2</sup>. The Ni NPs embedded in silica matrix have been prepared by atom beam sputtering technique and subsequent annealing. Figs. 1a and b show the cross-sectional TEM view of *pristine film* and the particle size histogram, respectively. It is clear that *pristine film* contains nearly spherical particles with a broad size distribution ranging from 3.8-60 nm with a mean particle size of ~25 nm. Inset of Fig. 1a shows the HRTEM image of a particle evidencing its single crystalline nature and the measured lattice spacing of 0.202 nm corresponds to (111) plane of fcc Ni. Figure 2a shows the cross-sectional TEM image of the *irradiated* film taking the direction of ion irradiation from top to bottom. It is clear from Fig. 2a that most of the Ni NPs change from spherical to prolate shape with their major axis aligned along the direction of ion beam at a fluence of  $5 \times 10^{13}$  ions/cm<sup>2</sup>. The elongated particles exhibit polycrystalline morphology, as apparent from HRTEM image (see inset of Fig. 2a).

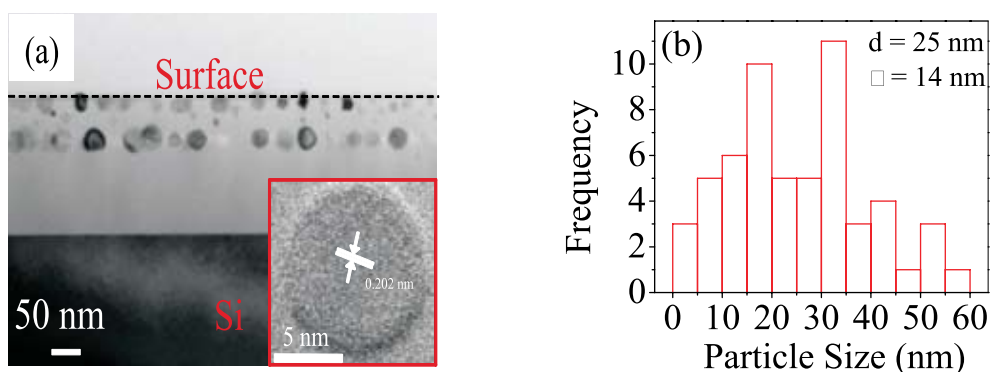


**Fig. 1. Cross-sectional TEM micrograph of (a) *pristine* Ni: SiO<sub>2</sub> granular film, (b) corresponding particle size histogram. Inset of Fig. 1 shows the HRTEM image of a spherical Ni nanoparticle showing single crystalline nature of particle.<sup>1</sup>**

Figures 2b and 2c show the histogram of major and minor axis length for prolate shape Ni particles. The mean major and minor axis lengths are 28.8 nm and 14.7 nm, respectively, estimated by considering all particles in Fig. 2a. The mean aspect ratio

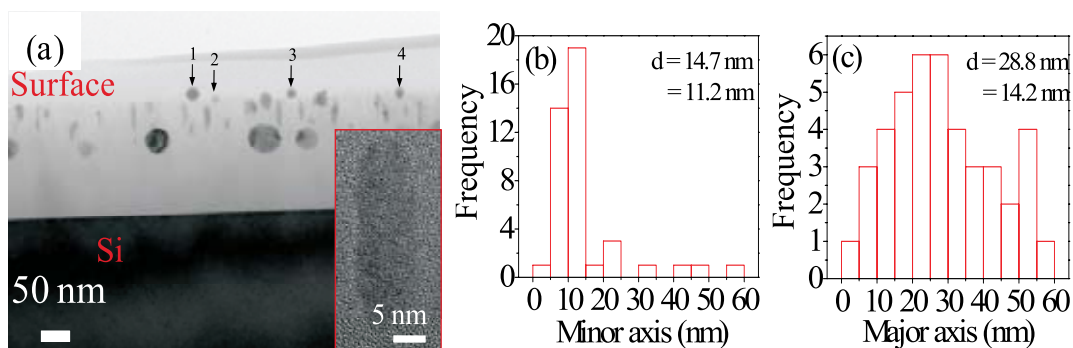


**Fig. 2. (a) Cross-sectional TEM micrograph of *irradiated* Ni: SiO<sub>2</sub> nanogranular film, (b) and (c) histogram of minor and major axis lengths of elongated particles, respectively. Inset of Fig. 2a shows the HRTEM image of an elongated Ni particle.<sup>1</sup>**

for prolate shaped particles is  $\sim 2$ . Further no deformation is observed for the free standing Ni particles present at the surface of film (indicated by 1-3 in Fig. 2a) and also those which are not surrounded by silica matrix completely (indicated by 4 in Fig. 2a). The experimental observations are well explained by thermal spike model based simulations.

## REFERENCE

- [1] H. Kumar, S. Ghosh, D. K. Avasthi, D. Kabiraj, A. Mücklich, S. Zhou, H. Schmidt, J. P. Stoquert, *Nanoscale Research Letters* 6, 155 (2011).

### 5.2.7 Modifications of Si-nanostructures embedded in Si- $\alpha$ -SiN<sub>x</sub>:H film by Swift heavy ion irradiation

Sarab Preet Singh<sup>1</sup>, S. Ghosh<sup>1</sup>, G. V. Prakash<sup>1</sup>, Saif A. Khan<sup>2</sup>, D. Kanjilal<sup>2</sup>, A. K. Srivastava<sup>3</sup>, Himanshu Srivastava<sup>3</sup> and P. Srivastava<sup>1</sup>

<sup>1</sup>Department of Physics, IIT Delhi, Hauz Khas, New Delhi

<sup>2</sup>Inter-University Accelerator Centre, Aruna Asaf Ali Marg, New Delhi

<sup>3</sup>Raja Ramanna Centre for Advanced Technology, Indore

Synthesis and modifications of Si-nanostructures embedded in dielectric matrix has been of considerable interest to scientific community [1]. In the present study, we have performed swift heavy ion (SHI) irradiation of as-deposited Si-rich  $\alpha$ -SiN<sub>x</sub>:H (SRSN) film to explore the possibility to obtain Si-nanostructures of uniform size and distribution. A SRSN thin film was deposited on p-type (100) Si substrate by Hg-sensitized Photo-CVD (chemical vapour deposition) technique. The as-deposited SRSN film were irradiated with 100 MeV Ni<sup>8+</sup> ions at a fluence of  $5 \times 10^{12}$  and  $1 \times 10^{14}$  ions/cm<sup>2</sup> respectively using a 15 UD Pelletron Accelerator at IUAC, New Delhi. Figure 1(a) shows the cross-sectional transmission electron microscopy (XTEM) image of the as-deposited SRSN film which clearly reveals the *in-situ* formation of Si-nanostructures (dark spots) embedded in  $\alpha$ -SiN<sub>x</sub>:H matrix. On irradiating the as-deposited SRSN film with 100 MeV Ni<sup>8+</sup> ions at a fluence of  $5 \times 10^{12}$  ions/cm<sup>2</sup>, complete dissolution of Si-nanostructures is noticeable [Fig. 1(b)], which is similar to as reported for metal nanocrystals [2]. Whereas, around a fluence of  $1 \times 10^{14}$  ions/cm<sup>2</sup> re-precipitation of Si-nanostructures in  $\alpha$ -SiN<sub>x</sub>:H matrix is observed [Fig. 1(c)]. This experimental observation in brief is described as a loss of hydrogen and structural modifications both induced due to energy dissipation during the passage of energetic ions through the SRSN film. The present study can pave a path to obtain Si-nanostructures of uniform size and distribution embedded in  $\alpha$ -SiN<sub>x</sub>:H dielectric matrix for the realization of Si-based optoelectronic devices.

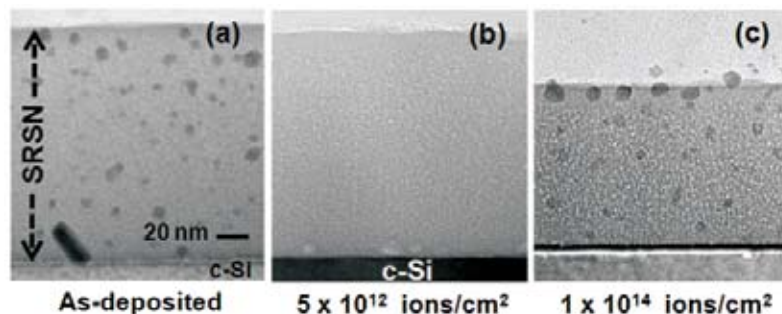


**Fig. 1. XTEM images of (a) As-deposited SRSN film (b) and (c) Irradiated with 100 MeV Ni<sup>8+</sup> ions with a fluence of  $5 \times 10^{12}$  ions/cm<sup>2</sup> and  $1 \times 10^{14}$  ions/cm<sup>2</sup> respectively.**

## REFERENCES

- [1] T. Mohanty, A. Pradhan, S. Gupta and D. Kanjilal, *Nanotechnology*, 15 (2004) 1620.  
 [2] J. C. Pivin, G. Roger, M. A. Garcia, F. Singh and D. K. Avasthi, *Nucl. Instrum. Methods B*. 215 (2004) 373.

### 5.2.8 Structural modifications of Carbon nanotubes by irradiation of Carbon, Nickel and Gold ion beam

Kiran Jeet<sup>1</sup>, V. K. Jindal<sup>1</sup>, L. M. Bharadwaj<sup>2</sup>, D. K. Avasthi<sup>3</sup> and Keya Dharamvir<sup>1</sup>

<sup>1</sup>Dept. of Physics & Centre for Adv. studies in Physics, Punjab University, Chandigarh

<sup>2</sup>Biomolecular Electronic & Nanotechnology Division, Central Scientific instruments organisation, Chandigarh

<sup>3</sup>Inter University Accelerator Centre, Aruna Asaf Ali Marg, New Delhi

The devices based on carbon nanotubes (CNTs) are used in space shuttles, nuclear reactors and other environmental conditions. In certain applications, these nanotubes are expected to interact with different types of radiations (photons, electrons or ions), which may affect their structure, electrical and mechanical properties and their range of applicability. It is therefore important to study their stability under extreme conditions of temperature and radiation. We studied the stability of CNTs both single-wall CNTs (SWCNTs) and multiwalled CNTs (MWCNTs) under irradiation of C, Ni and Au ion beams of energies 55 MeV, 60 MeV and 120 MeV respectively.

Irradiated samples were characterized using Raman Spectroscopy. Modifications of the disorder mode (D mode) and the tangential mode (G mode) under different irradiation fluences were studied in detail. Raman results of carbon ion beam indicate the interesting phenomenon of ordering of the system under irradiation. Under the effect of Ni and Au

ion irradiation, the structural evolution of CNTs occurs in three different stages. At lower fluences the process of healing occurs; at intermediate fluences damages on the surface of CNTs occurs and finally at very high fluences of the order of  $1 \times 10^{14}$  ions/cm<sup>2</sup> the system gets amorphised.

The variation of intensity of D and G peaks, along with the second order Raman modes, are found in all irradiated samples. In order to get the qualitative estimate of the modification occurring in CNTs due to irradiation, we plot the variation of disorder parameter as a function of ion fluence for all the three ion beams. The disorder parameter, is defined as the ratio of integral intensities of D and G peaks ( $I(D)/I(G)$ ). Figure 1 (a) shows variation of disorder parameter of SWCNTs as function of ions fluence and figure 1 (b) shows the same for MWCNT samples. From figure 1 (a), it is seen that the disorder parameter first decreases and then increases for Ni and Au ion irradiated samples whereas for C ion irradiated samples the disorder parameter decrease for whole range of fluences. Similarly for MWCNTs samples, it is seen that first the disorder parameter decreases and then increases for all the three ion beams. At high value of fluences i.e  $1 \times 10^{14}$  ions/cm<sup>2</sup> for Ni ion irradiated MWCNTs and  $5 \times 10^{13}$  ions/cm<sup>2</sup> Au ion irradiated MWCNTs samples, again decrease in disorder parameter is observed. The decrease in the value of disorder parameter at initial low fluences indicates healing or annealing of the tubes. It is seen that the behaviour of healing is dominated in C ion beam. The basic idea of healing of the tubes under irradiation is given in work reported earlier [1]. The increase in the disorder at intermediate fluence values show damages on the surfaces of CNTs or formation of nano crystalline graphite. Decrease in  $I(D)/I(G)$  value for MWCNT samples at highest irradiation fluence indicates formation of amorphous carbon (a-C). These observations can be explained on the basis of the three stage model of Ferrari and Robert [2]. According to their model, once the system becomes nano crystalline graphite further irradiation can cause the destruction of aromatic ring structure of the material which finally leads to the amorphization of the system.

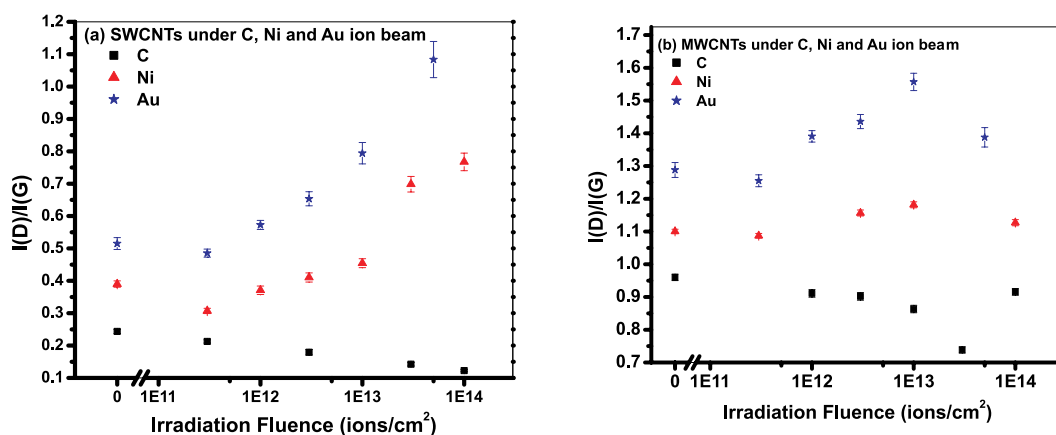


**Fig.1. Comparison of variation of disorder parameters as function of ion fluence for (a) SWCNTs and (b) MWCNTs irradiated by C, Ni and Au ion beams.**

## REFERENCES

- [1] K. Jeet, V. K. Jindal, L. M. Bharadwaj, D. K. Avasthi, and K. Dharamvir, *J. Appl. Phys.* 108, (2010), 034302-1-6.
- [2] A. C. Ferrari and J. Robertson *Phy. Rev. B* 61, (2000),14095-14107.

### 5.2.9 Photoluminescence Properties of SHI irradiated ZnO/PMMA nanocomposites

Sarla Sharma<sup>1</sup>, Shweta Agrawal<sup>1</sup>, Subodh Srivastava<sup>1</sup>, Fouran singh<sup>2</sup>, Y.K. Vijay<sup>1</sup>.

<sup>1</sup>Department of Physics, University of Rajasthan, Jaipur

<sup>2</sup>Inter-University Accelerator Center, Aruna Asaf Ali Marg, New Delhi

In recent years, many researchers have been given elaboration on nanocomposite systems by embedding inorganic nanoparticles into the polymer matrix. These nanocomposites offer a path for a new class of material which inherent in the properties of both inorganic nanoparticles and organic polymers [1]. The defects in polymer/nanoparticles nanocomposites can be altered by ion beam irradiations. It has been also observed that the photoluminescence (PL) emission of polymer/nanoparticles nanocomposites can be enhanced by swift heavy ion (SHI) irradiation [2]. Since swift heavy ion (SHI) irradiation is a unique technique to modify structural, optical, optoelectronic and transport properties of the materials [3-4]. The passage of SHI generates modifications in size, shape and structure of defects which in turn changes the fluorescence property of nanocomposite films. The extent of damage strongly depends on the mass of the incident ion, the irradiation energy and the fluence [5-6]. In present work we have studied the changes in optical property of ZnO nanoparticles doped in PMMA matrix which has been irradiated by 100MeV Ni<sup>+8</sup> beam at dose  $1 \times 10^{11}$  ions/cm<sup>2</sup>. Photoluminescence has been carried out to reveal surface emission.

The ZnO nanoparticles were synthesized via chemical route and then the nanocomposites were prepared using solution cast method. The as prepared nanocomposite film was irradiated by Ni<sup>+8</sup> ion (100 MeV) at a fluence of  $1 \times 10^{11}$  ions/cm<sup>2</sup> using the 15 UD Pelletron Accelerator facility at Inter University Accelerator Centre (IUAC), New Delhi. The structural and photo-luminescence properties were studied by XRD, PL measurements and fluorescence images respectively. The XRD patterns for pristine and irradiated ZnO/PMMA nanocomposite films show the formation of nanocomposites and could be indexed in similar fashion. The pattern shows a broad hump at  $2\theta \approx 11^\circ$  corresponding to the amorphous nature of PMMA [2], while other peaks appearing were indexed to pure wurtzite phase of ZnO. After irradiation reduction in peak intensity has been observed [7-8].

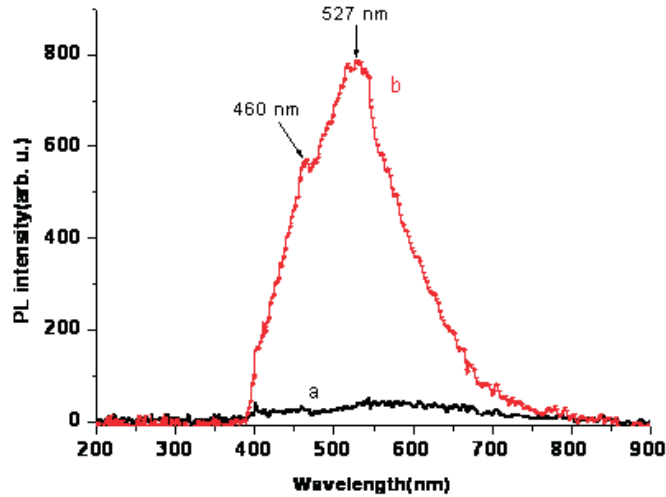


**Fig.1. PL spectra for ZnO/PMMA nanocomposite film (a) Pristie (b) irradiated**

The PL spectrum of pristine and irradiated ZnO/PMMA nanocomposite films are shown in Fig. 1 and it was found that after irradiation the luminosity of ZnO/PMMA nanocomposite film enhanced. It may be due to the change in microstructure of PMMA matrix and redistribution of nanoparticles during the formation of tracks in the nanocomposite films after SHI irradiation which is an outcome of SHI irradiation [9]. It is predicted on the basis of our model that the PL spectra given by pristine ZnO/PMMA nanocomposite film include the contribution from the emission and simultaneous absorption of photoluminescence by neighboring ZnO nanoparticles which result in lower PL emission. Whereas, SHI irradiation introduces the lower and higher density regions in ZnO/PMMA nanocomposite films and consequently the emission starts leading the absorption of photoluminescence which in turn results in enhanced luminosity in irradiated ZnO/PMMA nanocomposite film. These PL investigations were also corroborated by the fluorescence image investigations.

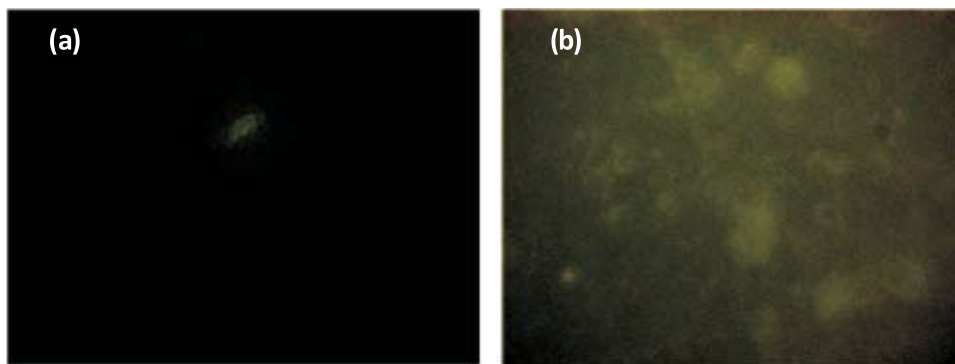


**Fig.2. Fluorescence image of ZnO/PMMA nanocomposite film (a) pristine (b) irradiated**

## REFERENCES

- [1] E. Tang, G. Cheng, X. Pang, X. Ma, F. Xing, Colloid. Polym. Sci. 284 (2006) 422–428.
- [2] S. Agarwal, S. Shrivastava, S. Kumar, S.S. Sharma, B. Tripathi, M. Singh, Y.K. Vijay, Bull. Mater. Sci. 32(6) (2009) 569-573.
- [3] O. Fukuoka, N. Matsunami, M. Tazawa, T. Shimura, M. Sataka, H. Sugai, S. Okayasu. Nucl. Instr. and Meth. In Phys. Res. B. 250 (2006) 295-299.
- [4] S.L. Wielunski, D.H. Hill, J. Quinn, R.A. Bartynski, P. Wu, Y. Lu, Nucl. Instr. and Meth. In Phys. Res. B. 219–220 (2004) 708- 712.
- [5] D.K. Awasthi, Curr. Sci.78 (2000) 1297.
- [6] D. Kanjilal, Curr. Sci. 80 (2001)1560.
- [7] D. Lesueur, A. Dunlop, Rad. Eff. & Def. Solids. 126 (1993) 163-172.
- [8] C.Dimitrov, H. Dammak, P. Legrand, A. Dunlop, D. Lesueur, Rad. Eff. & Def. Solids. 126 (1993) 115 – 118.
- [9] D. K. Awasthi, J. C. Pivin, Curr. Sci. 98 (2010) 780-792

### 5.2.10 Swift heavy ions induced structural phase transition in ZnS nanocrystalline thin films

Shiv P Patel<sup>1</sup>, J. C. Pivin<sup>2</sup>, A. K. Chawla<sup>3</sup>, Ramesh Chandra<sup>3</sup>, D. Kanjilal<sup>4</sup>, and Lokendra Kumar<sup>1</sup>

<sup>1</sup>Physics Department, University of Allahabad, Allahabad

<sup>2</sup>CSNSM, IN2P3-CNRS, Batiment 108, F-91405 Orsay Campus, France

<sup>3</sup>Nanoscience Laboratory, IIC, Indian Institute of Technology, Roorkee

<sup>4</sup>Inter-University Accelerator Centre, Aruna Asaf Ali Marg, New Delhi

Zinc sulfide (ZnS) has two polytypes, with zinc-blend (ZB) cubic and wurtzite (W) hexagonal crystal structure. Out of these two phases, ZB phase is more stable at standard temperature and pressure. The ZB structure of bulk ZnS changes into W structure at transition temperature of 1020 °C [1]. As it is well established that substrate temperature greatly influences the atomic motion and grain growth kinetics, and is also an essential parameter for the development of crystalline films [2]. In the present work, ZnS nanocrystalline thin films with both ZB and W structure have been fabricated by the variation of substrate temperature ( $T_s$ ). Modifications of these crystal structures of ZnS thin films using energetic ion beam by means of swift heavy ion (SHI) are also presented [3].

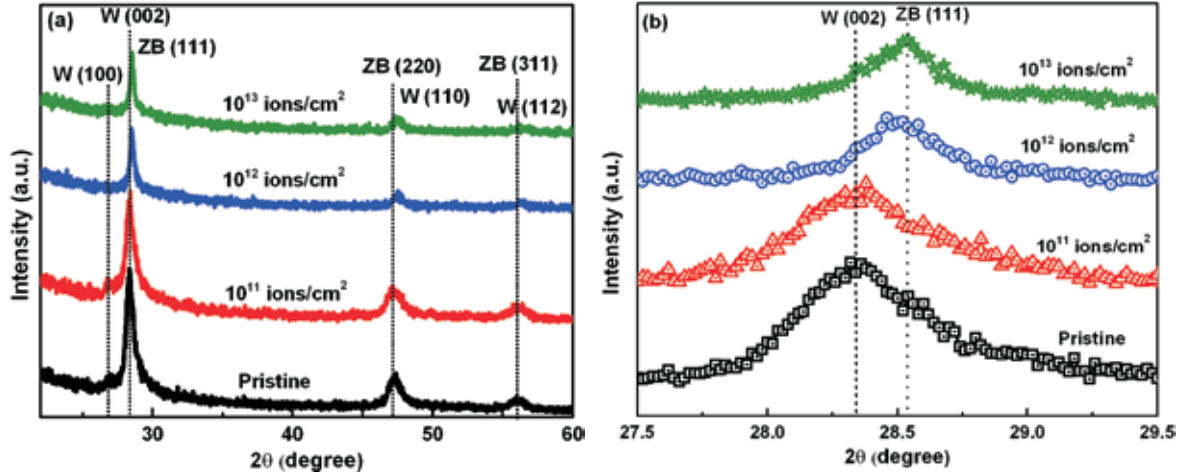


**Fig.1.(a)** XRD pattern of ZnS thin film on fused silica deposited at 400 °C and irradiated at different fluences (b) extended part of Figure 1(a) for 2θ value ranging from 27.5° to 29.5° for evidencing clearly the shift of (002) peak [3].

ZnS nanocrystalline thin films were deposited at  $T_s$  of 200 °C, 300 °C and 400 °C using pulsed laser deposition technique [3]. Rutherford backscattering (RBS), X-ray diffraction (XRD), and UV-Visible absorption measurements were used to characterize these samples. The films deposited at  $T_s$  of 200 °C have ZB structure while films deposited at  $T_s$  of 300 °C and 400 °C have W structure [3]. The films have been irradiated with 150 MeV Ni ions using fluences of  $1 \times 10^{11}$ ,  $1 \times 10^{12}$ , and  $1 \times 10^{13}$  ions/cm<sup>2</sup> at room temperature. The films with ZB structure do not show any structural phase transformation due to ion irradiation. On the contrary, the films with W structure are converted into ZB structure. Figure-1 shows the XRD pattern of a film deposited at  $T_s$  of 400 °C (pristine) and ion irradiated at different fluences. The pristine sample shows the diffraction peaks at 26.82°, 28.30°, 47.20° and 56° which are characteristics of (100), (002), (110), and (112) lattice planes of the W structure of ZnS [3]. The (002), (110) and (112) peaks of pristine samples, are found to be shift towards higher 2θ values in the samples irradiated at fluence of  $10^{13}$  ions/cm<sup>2</sup> while (100) peak vanishes as shown in Figure 1. These shifted peaks match better with lattice planes of ZB structure. A complete model based on thermal and pressure spike has been proposed to explain these results [3]

## REFERENCES

- [1] B. Gilbert, B. H. Frazer, H. Zhang, F. Haung, J. F. Banfield, D. Haskel, J. C. Lang, G. Srajer, G. D. Stasio, Phys. Rev. B 66 (2002) 245205.
- [2] Shiv P. Patel, J.C. Pivin, V.V. Siva Kumar, A. Tripathi, D. Kanjilal, and Lokendra Kumar, Vacuum 85 (2010) 307.
- [3] Shiv P. Patel, A. K. Chawla, Ramesh Chandra, Jai Prakash, P. K. Kulriya, J. C. Pivin, D. Kanjilal, and Lokendra Kumar, Solid State Communications 150 (2010) 1158.

### 5.2.11 Synthesis of Au Nanoparticles at the Surface and Embedded in Carbonaceous Matrix by 150 keV Ar Ion Irradiation

Jai Prakash<sup>1</sup>, A. Tripathi<sup>2</sup>, V. Rigato<sup>3</sup>, J. C. Pivin<sup>4</sup>, Jalaj Tripathi<sup>1</sup>, Keun Hwa Chae<sup>5</sup>, Sanjeev Gautam<sup>5</sup>, P. Kumar<sup>2</sup>, K. Asokan<sup>2</sup> and D. K. Avasthi<sup>2</sup>

<sup>1</sup>Dept. of Chemistry, M.M.(P.G) College [Ch. Charan Singh University, Meerut] Ghaziabad

<sup>2</sup>Inter University Accelerator Centre, Aruna Asaf Ali Marg, New Delhi

<sup>3</sup>INFN Laboratori Nazionali di Legnaro, Via Romeo. 4, 35020 Legnaro, Padova, Italy

<sup>4</sup>CSNSM, Batiment 108, 91405, Orsay Campus, France

<sup>5</sup>Nano Analysis Center, Korea Inst. of Science and Technology, Seoul, Republic of Korea

In recent years, there have been efforts to develop the polymer based nanomaterials because of their importance in applications in microelectronics and fabrication of nano-electronics devices. Metal-polymer systems are one such polymer based materials. These metal polymer systems have been widely studied for (i) metallization of polymer which is of much interest in microelectronics for multilayer devices, coatings, packaging industry [1] and (ii) synthesizing metal polymer nanocomposites which are of great interest in thin film device applications and nano-electronics devices. Particularly, the nanocomposites of noble metals are of rich interest because of their optical applications [2].

Ion beam irradiation is a unique tool for the synthesis and engineering of nanostructures. Surface nanostructuring by ion beam irradiation is the topic of interest not only from technological point of view but also from the scientific point of view for understanding the ion beam interaction of surfaces. Synthesis of noble metal nanoparticles or surface nanostructuring of thin film is the important class of nanotechnology because of their potential applications in thin film technology and nanoelectronic [3]. Ion beam irradiation in case of bilayer thin films may induce surface nanostructuring and at the same time, mixing can take place introducing embedded nanoparticles in the matrix forming nanocomposite [4]. We have investigated low energy ion beam induced surface nanostructuring of thin Au film deposited on polyethylenetetrathlate (PET) substrate with the emphasis on ion beam induced mixing using 150 keV Ar ions.

Samples were prepared by depositing 15 nm Au film on PET (polyethyleneterephthlate) [From Good Fellow, Cambridge Ltd. England] substrate of thickness ~ 350  $\mu\text{m}$  using electron beam evaporation technique. Irradiation was carried out with 150 keV Ar ions at the fluences varying from  $5 \times 10^{15}$  to  $5 \times 10^{16}$  ions/cm<sup>2</sup> at a current of  $0.5 \mu\text{A/cm}^2$  using low energy ion beam facility (LEIBF) at IUAC, New Delhi. Surface structures were characterized with field emission-scanning electron microscopy

(FE-SEM) [MIRA\, TESCAN] at IUAC, New Delhi. Electron beam of energy 20 keV was used with the magnification upto 100 kx to capture the SEM images in the present experiment. For compositional analysis, the energy dispersive X-ray (EDX) analysis was performed using INCA penta FETx3 attached with FE-SEM.

Figure 1 shows the SEM images (a) pristine sample and (b) sample irradiated with 150 keV Ar ions at the fluence of  $5 \times 10^{16}$  ions/cm<sup>2</sup>. EDX analyses confirm the presence of uniform Au film on the polymer in the pristine sample [EDX spectra is not shown here], as it was performed at different places and similar composition was obtained. In figure 1 (b), the dark and bright regions of the SEM images correspond to mixed (Au-C) region (carbon rich) and Au nanoparticles ( $45 \pm 20$ ), respectively. Dark regions are the secondary electron image from the carbon (rich) mainly because the ion irradiation results in liberating hydrogen from the polymer leaving amorphous carbon rich material [5,6]. Au nanoparticles (bright spots) on the surface with the large fraction of Au-C mixed region (dark region), are formed after irradiation at fluences  $5 \times 10^{16}$  ions/cm<sup>2</sup>.

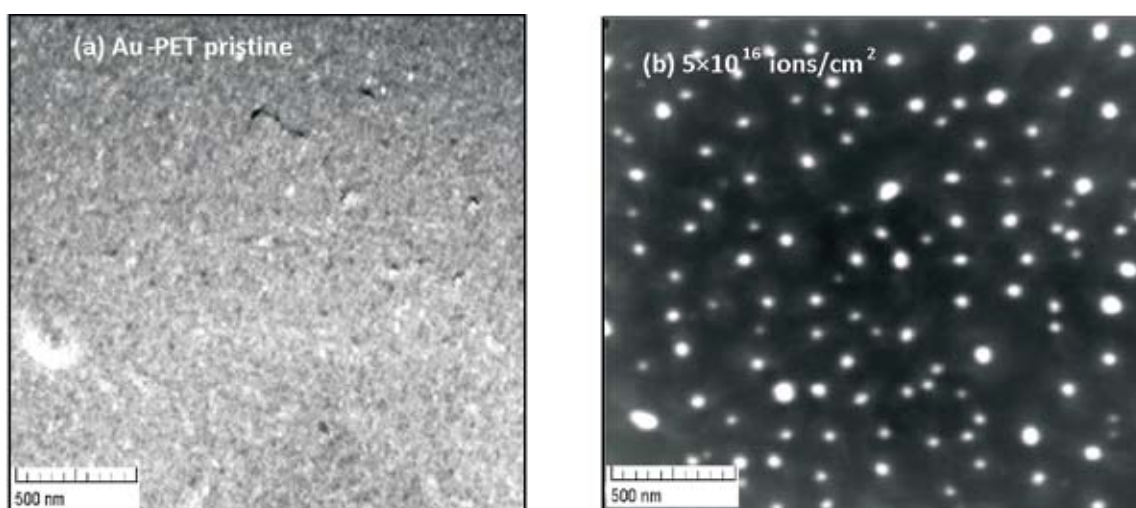


**Fig. 1. SEM images of Au-PET (a) pristine sample and (b) sample irradiated with 150 keV Ar ions at the fluence of  $5 \times 10^{16}$  ions/cm<sup>2</sup>. Dark region corresponds to the mixed Au-C region whereas the bright spots correspond to the Au nanoparticles after irradiation at the higher fluence. [From Ref. 6]**

In conclusion, we report on synthesis of spherical Au nanoparticles at the surface and embedded in carbonaceous matrix by 150 keV Ar ion irradiation of thin Au film on polyethyleneterephthalate (PET).

## REFERENCES

- [1] K L Mittal J. Vac. Sci. Tech. 13 (1976) 19.
- [2] D. K. Avasthi, Y. K. Mishra, D. Kabiraj, N. P. Lalla, J. C. Pivin, Nanotechnology 18 (2007) 125604.
- [3] M. Stepanova, S. K. Dew, J. Phys.: Condens. Matter 2 (2009) 224014.

- [4] Z. Paszti, G. Peto, Z. E. Horvath, O. Geszti, A. Karacs, L. Guzzi, Nucl. Instr. and Meth. B 178 (2001) 131.
- [5] Y. Q. Wang, M. Curry, E. Tavenner, N. Dobson, R. E. Giedd, Nucl. Instr. and Meth. B 219/220 (2004) 798.
- [6] Jai Prakash, A. Tripathi, V. Rigato, J. C. Pivin, Jalaj Tripathi, Keun Hwa Chae, Sanjeev Gautam, P. Kumar, K. Asokan, D. K. Avasthi, J. Phys. D: Applied Physics 44 (2011) 125302.

### **5.2.12 Energy dependence studies of surface nanostructures on InP(100) using energetic ion bombardment**

Indra Sulania<sup>1,2</sup>, Mushahid Husain<sup>2</sup>, Dinesh Agarwal<sup>1</sup>, Praveen Kumar<sup>1</sup> and D K Avasthi<sup>1</sup>

<sup>1</sup>Inter University Accelerator Centre, Aruna Asaf Ali Marg, New Delhi

<sup>2</sup>Jamia Milia Islamiya University, New Delhi

In recent years, special interest is being paid to the study of self-organized nanopattern formation on surfaces by *ion beam sputtering* (IBS) techniques [1]. In general, two types of surface nanostructures can be induced by IBS: (a) nano-ripples and (b) nanodots. In both cases, the pattern formed by these nanostructures can have dimensions ranging from a few nm to hundreds of nm. These patterns can be produced on variety of materials such as amorphous or crystalline. The generated nanostructures depend upon many parameters such as angle of incidence, ion fluence and ion energy etc. Studies have shown that with increase in ion energy, the surface nanostructures show an increase in the dimension (size/wavelength) of nanostructures. There is an increase in ripple wavelength,  $\lambda \sim E^n$ , where E is the energy of the ions and n is between 0 and 1. There are not many experimental studies to validate this relation. In a study by Facsko et al., for ion beam sputtered (IBS) nanodot patterns on GaSb, 15 different energy values have been studied [2]. They obtained a value of  $n = 0.5 \pm 0.02$ . In our study, we have used different ion energies varying from 50-250 keV of Ar ions to create surface nanostructures on InP. The experiment was performed in Low Energy Ion Beam (LEIB) facility of IUAC, New Delhi.

In the present studies we have used the Ar<sup>+</sup> ions with different energies ranging from 50 keV to 250 keV to bombard the commercially available InP(100) single crystalline samples. The bombardment was carried out at an incidence angle of 20° with respect to the surface normal. The ion fluence for different energies was also varied from  $1 \times 10^{16}$  ions/cm<sup>2</sup> to  $3 \times 10^{17}$  ions/cm<sup>2</sup>. The studies were carried out at LEIB facility of the Inter University Accelerator Centre, New Delhi.

The commercially available InP(100) wafer was taken and cleaved into smaller pieces of  $1 \times 1$  cm<sup>2</sup> to be used for irradiation. These small pieces were cleaned with ethanol

to remove the traces of impurities from the surface of InP. The surface morphology of the pristine and irradiated samples were taken using Nanoscope IIIa SPM in tapping mode AFM. The images of pristine and irradiated samples at an energy of 50 keV are shown in figures 1 and 2. The surface of the pristine sample is flat with a rms roughness  $\sim 0.2$  nm. The irradiated samples show an increase in roughness with increase in energy. The size of the dots also increases with increase in ion energy. The fluence used for the irradiated sample was  $8 \times 10^{16}$  ions/cm<sup>2</sup>. The images were scanned for  $2\mu\text{m} \times 2\mu\text{m}$  scan size. The pristine sample (Figure 1) has a roughness  $\sim 0.6$  nm. Upon irradiation, the nanodot formation is clearly visible on the surface (Figure 2).

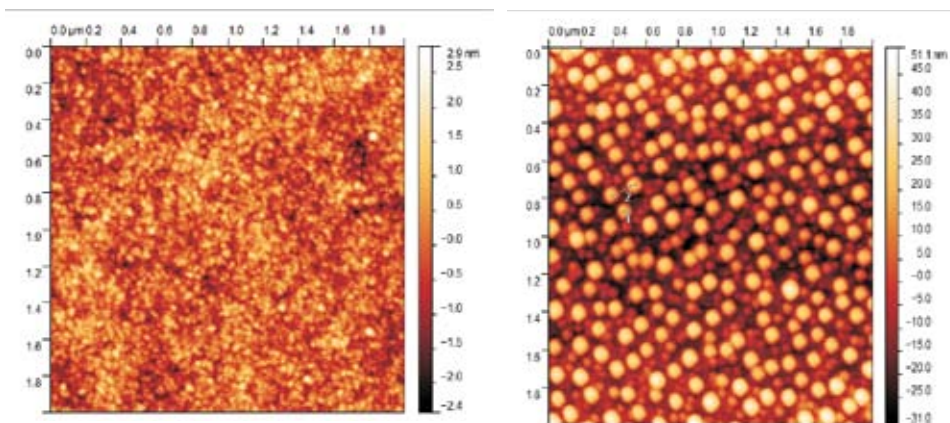


**Fig. 1.**

**Fig.2.**

The average size of the nanodots was found to be 70nm. There is an increase in the roughness as compared to the pristine sample to 15.9 nm. There is ordering of nanodots with square symmetry. The nanodots formed are circular in shape with a small variation in their sizes. The detailed analysis of the energy dependence is in progress.

## REFERENCES

- [1] Facsko S, Dekorsy T, Koerdts C, Trappe C, Kurz H, Vogt A, Hartnagel HL (1999) Formation of ordered nanoscale semiconductor dots by ion sputtering. *Science* 285: 1551-1553
- [2] Facsko S, Kurz H, Dekorsy T (2001) Energy dependence of quantum dot formation by ion sputtering. *Phys Rev B* 63: 165329

### 5.2.13 Effect on Optical Properties of Silver/PVA Nanocomposites Influenced by High Energy Ion Beam Irradiation

Chaitali Gavade, Dolly Singh, N.L.Singh

Department of Physics, M.S.University of Baroda, Vadodara

The nanocomposite films of different concentrations (5%, 10% and 15%) of nano particles (Ag, Ni and Cu) were prepared by dispersed in PMMA and PS by casting method.

These films were irradiated with 85 MeV  $C^{+6}$  ions and 100 MeV  $Si^{+9}$  ions at different fluences of  $1 \times 10^{11}$ ,  $1 \times 10^{12}$  ions/cm<sup>2</sup>. We have also synthesized Ag-PVA nanocomposites by in situ technique and irradiated with these ions. Here we are discussing one of the results of samples.

Noble metal nanoparticles dispersed in insulating matrices have attracted the interest of many researchers as such nanocomposites exhibit unique optical, magnetic and electrical properties, making them suitable as advanced technological materials to be used as novel sensors, in catalytic applications, for energy storage, etc. Recently, considerable attention has been paid to the in situ synthesis of metal nanoparticles in polymer matrixes, which involves the dissolution and reduction of metal salts/ complexes [1-2].

For the preparation of silver nanoparticles, silver nitrate solution (0.01 M) and 5% solution of polyvinyl alcohol (MW 1, 25, 000) were used as a metal salt precursor and a stabilizing agent, respectively. Amine hydrazine (1%, w/v) was used as a reducing agent. To the polyvinyl alcohol solution different volume of silver nitrate and amine hydrazine were added and reaction was carried out. The transparent colourless solution was converted to the characteristic pale brown yellow colour [3]. The confirmation of nanoparticles was carried out using TEM analysis as shown in Fig. (1). Then this solution was allowed to dry at room temperature for 48 hours and these films were irradiated with 85 MeV  $C^{+6}$  ions at different fluences of  $1 \times 10^{11}$ ,  $1 \times 10^{12}$  ions/cm<sup>2</sup>.

Where, A =  $1 \times 10^{11}$ , B =  $1 \times 10^{12}$

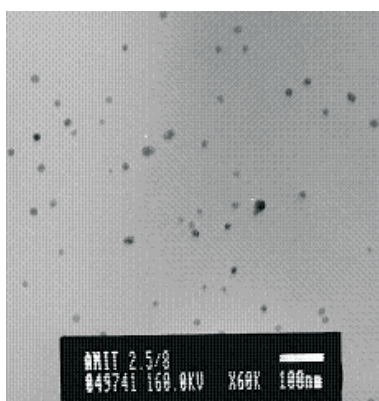


**Fig1**

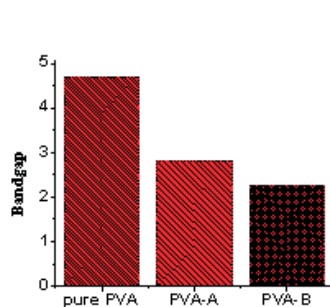


**Fig2 (a)**

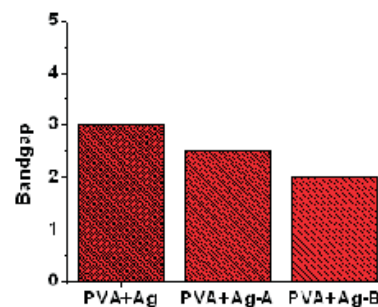


**Fig2 (b)**

**Fig.1. shows the TEM image of PVA-Ag nanocomposites, Fig.2 (a) and (b) show the effect of band gap with different fluences as compared with pristine samples**

The study of optical absorbance provides the information about the band structure of solids. Optical characteristic of the pristine and irradiated samples have been studied by Perkin- Elmer 25 Lambda UV-Visible Spectroscope in the frequency range of 200-800  $\text{cm}^{-1}$ . The optical band gap  $E_g$  is obtained by Tauc's equation [4]

$$\text{i. e. } \omega\varepsilon(\lambda) = (\hbar\omega - E_g)^2$$

where  $\varepsilon(\lambda)$  is the optical absorbance and  $\lambda$  is the wavelength. The intersection of the extrapolated spectrum with the abscissa of the plot  $\varepsilon^{1/2}/\lambda$  versus  $1/\lambda$  yields the gap wavelength  $\lambda_g$  from which the energy gap is derived as  $E_g = hc/\lambda_g$ . It reveals from the plots that the band gap energy decreases initially with increasing fluences.

## REFERENCES

- [1] Z. Zhang and M. Han, J. Mater. Chem., 13 (2003) 641.
- [2] Tyurin, G. De Filpo, D. Cupelli, eXPRESS Polymer Letters .4(2) (2010) 71.
- [3] Pal, S. Shah and Surekha Devi, Colloids and Surfaces A: Physicochem. Eng. Aspects 302 (2007) 51.
- [4] Das, S. Dhara and A. Patnaik Physical Rev B 59 (1999) 11069.

### 5.2.14 The effect of $\text{Ag}^{16+}$ SHI irradiation on the Strontium hexaferrite nanoparticles

N. R. Panchal<sup>1</sup>, R. B. Jotania<sup>1</sup> and K. Asokan<sup>2</sup>

<sup>1</sup> Department of Physics, Gujarat University, Ahmedabad

<sup>2</sup> Inter-University Accelerator Centre, Aruna Asaf Ali Marg, New Delhi

Over the decades, radiation damage is a widely used technique for controlled modification of physical properties of different systems [1]. This is possibly the most suitable one for tuning structural, electrical and magnetic properties of different materials through controlled production of defects and disorder induced by ion-beam irradiation [2, 3].

Objective of present investigation is to study the effect of  $\text{Ag}^{16+}$  SHI irradiation on synthesized  $\text{SrFe}_{12}\text{O}_{19}$  hexaferrite nanoparticles prepared by two different routes namely co-precipitation and Self Propagating High temperature Synthesis (SHS). Nanocrystalline Sr-M hexaferrites are irradiated with 200 MeV  $\text{Ag}^{16+}$  ions with two different fluences  $1 \times 10^{12}$  and  $1 \times 10^{13}$  ions/ $\text{cm}^2$ . There are only few reports on swift heavy ion (SHI) induced modification of structural properties of  $\text{SrFe}_{12}\text{O}_{19}$  prepared by these routes. SHI irradiation technique is unique due to its capability to deposit very high energy in a localized area of the material and thereby attaining spatial selection while modifying its properties [4].

To study the structural morphology, the samples before and after irradiation are characterized by using XRD and SEM. XRD results are shown in fig.1(a, b) for unirradiated sample and the samples irradiated with fluencies  $1 \times 10^{12}$  and  $1 \times 10^{13}$  ions/cm<sup>2</sup>. All the peaks are assigned to the M-phase of Strontium hexaferrite before and after irradiation. No extra peak of impurity has been observed for irradiated samples. Average particle size has been estimated by using Debye Scherrer formula for the most intense peaks from XRD for each sample.

It is observed that there is a negligible increase in particle size in case of SrFe<sub>12</sub>O<sub>19</sub> prepared by co-precipitation route with irradiation and increasing the fluence. But for the case of SrFe<sub>12</sub>O<sub>19</sub> prepared by SHS route, grain size decreases from 78 nm to 48 nm with Ag<sup>16+</sup> irradiation. Further increasing the fluence to  $1 \times 10^{13}$  ions/cm<sup>2</sup>, still particle size is reducing. Figure 2 shows the effect of ion fluence on particle size for SrFe<sub>12</sub>O<sub>19</sub> hexaferrite particle prepared by different chemical routes.

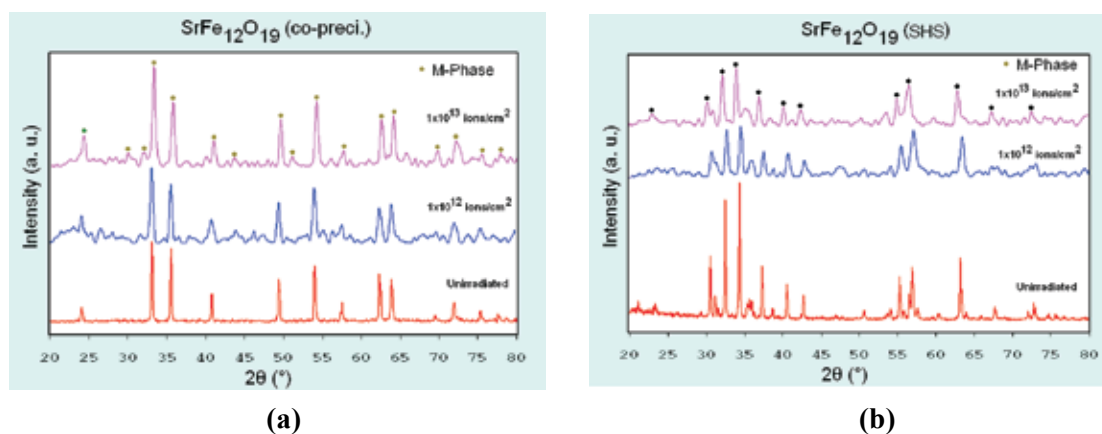


Fig. 1. XRD of SrFe<sub>12</sub>O<sub>19</sub> hexaferrites (un-irradiated and irradiated) synthesized by (a) co-precipitation and (b) auto combustion method

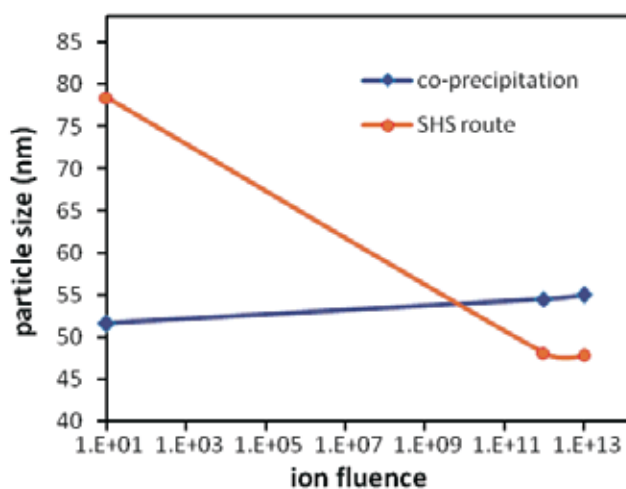


Fig. 2. Effect of ion fluence on particle size

## REFERENCES

- [1] D. C. Look et al., Appl. Phys. Lett. 82 (1999) 811  
 [2] W. S. Shi et al., J. Appl. Phys. 91 (2002) 5640  
 [3] P. M. Ratheesh Kumar et al., J. Appl. Phys. 97 (2005) 013509  
 [4] V V Ison, A Ranga Rao, V Dutta, P K Kulriya, D K Avasthi and S K Tripathi, J. Appl. Phys. 106 (2009) 023508

### 5.2.15 Swift Heavy Ion Induced Effects on PEO based Polymer Nano Composite Electrolytes

Sangeeta Kishore<sup>1</sup>, Dolly Singh<sup>1</sup>, Chaitali Gavde<sup>1</sup>, N. L. Singh<sup>1</sup>, F. Singh<sup>2</sup>

<sup>1</sup> Department of Physics, The M. S. University of Baroda, Vadodara

<sup>2</sup> Inter-University Accelerator Center, Aruna Asaf Ali Marg, New Delhi

Solid electrolyte materials have attracted growing interest in recent years owing to their potential application at ambient temperature in ionic devices such as polymer batteries, electrochemical display devices, super capacitors and fuel cells [1]. Designed synthesis of a novel polymer electrolyte exhibiting high ionic conductivity, good electrochemical stability and mechanical strength, is highly desired and has been a vital part in the effort to create a new generation of polymer ion batteries [2]. PEO dissolves high concentrations of a wide variety of salts to form polymeric electrolytes. Sodium Iodide (NaI) has been chosen as electrolyte as sodium has more advantages over lithium counter parts.

PEO (MW 3,00,000) and PVA (MW 1, 25,000) has been used for making films. Nano SnO<sub>2</sub> and nano In<sub>2</sub>O<sub>3</sub> were prepared using citrate gel method. Polymers and NaI were dissolved in double distilled water and complexed. The nanoparticles were added to the

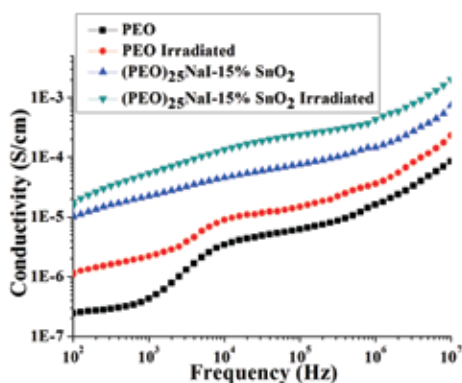


Fig.1. Frequency spectra of ac conductivity of pristine and irradiated PEO/ (PEO)<sub>25</sub>NaI-15%SnO<sub>2</sub>

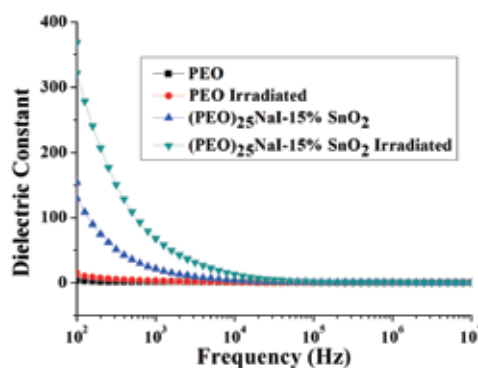


Fig.2. Frequency spectra of Dielectric constant of pristine and irradiated PEO/ (PEO)<sub>25</sub>NaI-15%SnO<sub>2</sub>

solution in different concentrations (5%, 10%, 15%, and 20%) and sonicated for 10 minutes. The solution was then immediately cast on a Teflon mould and dried at room temperature till the solvent evaporated completely. The free standing films hence prepared were cut in size  $1 \times 1 \text{ cm}^2$  and were irradiated with 80 MeV  $\text{C}^{6+}$  ions and 120 MeV  $\text{Si}^{10+}$  ions under high vacuum with a beam current of 0.5 pA (particles per nano ampere) at a fluence of  $1 \times 10^{11}$  ions/ $\text{cm}^2$ . AC impedance measurements were carried out in the frequency range 100 Hz to 10 MHz using an impedance-phase analyzer (Solartron-1260). The films were sandwiched between two spring loaded copper electrodes.

Fig. 1 shows the variation of ac conductivity with frequency for pristine and irradiated PEO/(PEO)<sub>25</sub>NaI-15%SnO<sub>2</sub> at room temperature. The ac conductivity patterns show a frequency independent plateau in the low frequency region and exhibits dispersion at higher frequencies. This behaviour obeys the universal power law

$$\sigma_{ac} = \sigma_0 + A\omega^n$$

where  $\sigma_0$  is the dc conductivity (frequency independent plateau in the low frequency region), A is the pre-exponential factor and n is the fractional exponent between 0 and 1 [3]. The deviation from  $\sigma_0$  (plateau region) value in the conductivity spectrum (in the low frequency region) is due to the electrode polarization effect. The overall behaviour of  $\sigma_{ac}$  follows the universal dynamic response, which has widely been observed in disordered materials like ionically conducting glasses, conducting polymers, and also doped crystalline solids and is generally believed to be reflected in the mechanism of charge transport behaviour of charge carriers [4]. From fig. 2 it is observed that incorporation of SnO<sub>2</sub> enhances the dc conductivity of polymer and upon ion irradiation the conductivity increases further. Upon ion irradiation of (PEO)<sub>25</sub>NaI-15%SnO<sub>2</sub>, the conductivity spectrum remains similar as that of the PEO, except dispersion in the low frequency region, where the deviation from  $\sigma_0$  (plateau region) is more prominent.

Fig. 2 compares the variation of dielectric constant with frequency for pristine and irradiated PEO/ (PEO)<sub>25</sub>NaI-15%SnO<sub>2</sub> at room temperature. In all the cases, a strong frequency dispersion of permittivity is observed in the low frequency region followed by a nearly frequency independent behaviour above 10 kHz. The low frequency dispersion region is attributed to the contribution of charge accumulation at the electrode-electrolyte interface [5]. The decrease of dielectric constant with increase in frequency may be attributed to the electrical relaxation processes, but at the same time the material electrode polarization cannot be ignored, as the samples under investigation are ionic conductors. It is seen that with addition of SnO<sub>2</sub> and ion irradiation, dielectric constant value increases in the lower frequency and remains nearly same in the higher frequency region. The addition of nanoparticle and ion irradiation may result in more localization of charge carriers along with mobile ions causing higher ionic conductivity. This may be the reason for higher dielectric constant and strong low frequency dispersion upon SnO<sub>2</sub> incorporation and ion irradiation.

## REFERENCES

- [1] R. Chandrasekaran and S. Selladurai, J. Solid State Electrochem., 5 (2001) 355.
- [2] Robert L. Karlinsey, Lyudmila M. Bronstein, and J. W. Zwanziger, J. Phys. Chem. B 108 (2004) 918.
- [3] A. K. Jonscher, Nature 267 (1977) 673.
- [4] Dillip K. Pradhan, R. N. P. Choudhary, B. K. Samantaray, Int. J. Electrochem. Sci., 3 (2008) 597.
- [5] R. Mishra, K.J. Rao, Solid State Ionics 106 (1998) 113.

### 5.2.16 Magnetic transition in Co doped ZnS thin films by 120 MeV Ag ion irradiation

Shiv P Patel<sup>1</sup>, J. C. Pivin<sup>2</sup>, A. K. Chawla<sup>3</sup>, Ramesh Chandra<sup>3</sup>, D. Kanjilal<sup>4</sup>, and Lokendra Kumar<sup>1</sup>

<sup>1</sup>Physics Department, University of Allahabad, Allahabad

<sup>2</sup>CSNSM, IN2P3-CNRS, Batiment 108, F-91405 Orsay Campus, France

<sup>3</sup>Nanoscience Laboratory, IIC, Indian Institute of Technology, Roorkee

<sup>4</sup>Inter-University Accelerator Centre, Aruna Asaf Ali Marg, New Delhi

The integration of electrons spin state together with their configuration energy level for conveying information in devices has become highly desirable goal in the growing field of spintronics. The insertion of transition metal impurities such as Co as solutes into semiconductors is one way of integration of spin effect in non-magnetic systems, known as diluted magnetic semiconductors (DMS). The II–VI or III–V compounds semiconductors seem to be the most promising materials for DMS based spintronics applications.

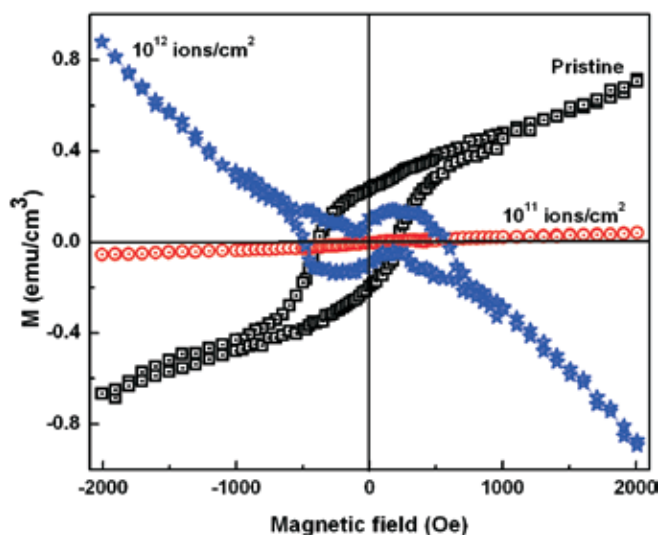


Fig. 1. M-H curve of pristine and irradiated films at different fluences.

Co (2.5%)-doped ZnS magnetic thin films were deposited by means of pulsed laser ablation on  $\alpha$ -quartz substrates at elevated temperatures ( $T_s$ ) of 200 °C, and 600 °C. X-ray diffraction, optical absorption, transmission electron microscopy (TEM) and SQUID measurements have been performed to study the structural and magnetic properties. Co has been successfully substituted at Zn tetrahedral sites in ZnS as evidenced by absorption, XRD, and TEM measurements. All films showed wurtzite crystal structure contrarily to films free of Co [1-2] and Co may stabilize the wurtzite structure of ZnS. The film deposited at  $T_s$  of 200 °C showed a weak ferromagnetism only at low temperature whereas the ferromagnetism is preserved up to RT in films deposited at  $T_s$  of 600 °C. 120 MeV Ag ion beam irradiation of films deposited at  $T_s$  of 600 °C has been carried out using fluences of  $1 \times 10^{11}$  ions/cm<sup>2</sup> and  $1 \times 10^{12}$  ions/cm<sup>2</sup> at room temperature to produce structural defects in the sample. The diffraction peak intensity and band gap of films decreases with increasing ion fluence. The magnetization of films deteriorate with increasing ion fluence due to irradiation, and they become a paramagnetic (paramagnetic with a Curie temperature below RT) at fluence of  $10^{12}$  ions/cm<sup>2</sup>. Therefore, one can say that structural defects in the films affect the long range coupling through orbitals of the host ZnS lattice.

## REFERENCES

- [1] Shiv P. Patel, J.C. Pivin, V.V. Siva Kumar, A. Tripathi, D. Kanjilal, and Lokendra Kumar, Vacuum 85 (2010) 307.
- [2] Shiv P. Patel, A. K. Chawla, Ramesh Chandra, Jai Prakash, P. K. Kulriya, J. C. Pivin, D. Kanjilal, and Lokendra Kumar, Solid State Communications 150 (2010) 1158.

### 5.2.17 Ni<sup>7+</sup> ion irradiation effect on thermally oxidized ZnO and In<sub>2</sub>O<sub>3</sub> films

R. K Bedi, A. K. Bal and A. Singh

Department of Physics, Guru Nanak Dev University, Amritsar

Inter University Accelerator Centre, New Delhi

Research interest on the metal oxide materials like ZnO and In<sub>2</sub>O<sub>3</sub> is still growing because of their potential applications in optoelectronic devices, displays, smart windows and gas sensors [1, 2]. Swift heavy ion irradiation is a unique tool to modify the properties of the material [3, 4].

In the present study we prepared Zinc oxide (ZnO) and Indium oxide (In<sub>2</sub>O<sub>3</sub>) films by thermal oxidation of pre-deposited zinc and indium films respectively, on the glass substrate kept at room temperature. These films are irradiated with 100 MeV Ni<sup>7+</sup> ions with ion fluence in range of  $5 \times 10^{11}$ -  $5 \times 10^{13}$  ions/cm<sup>2</sup>. The thickness of the films was in the range of 0.2-0.5  $\mu$ m. Figure 1(a, b) show the FESEM images of pristine and irradiated ZnO films respectively. The FESEM observation of thermally oxidized pristine ZnO showed that

nanowires embedded on cactus type crystallites are formed. At a fluence of  $5 \times 10^{13}$  ions/cm<sup>2</sup>, the material does not seem to have any definite morphology and small agglomerated grains were observed with a few number of nanowires. Thus irradiation has resulted in destruction of nanowires. Fig. 2(a) shows FESEM images of the surfaces of the In<sub>2</sub>O<sub>3</sub> films oxidized at 500 °C. The micrographs show that there are well developed microcrystallites of different sizes scattered on the surface of the films. The morphology changes to rod like structures at a fluence  $5 \times 10^{13}$  ions/cm<sup>2</sup> as shown in Fig. 2(b). Detailed analysis is in progress.

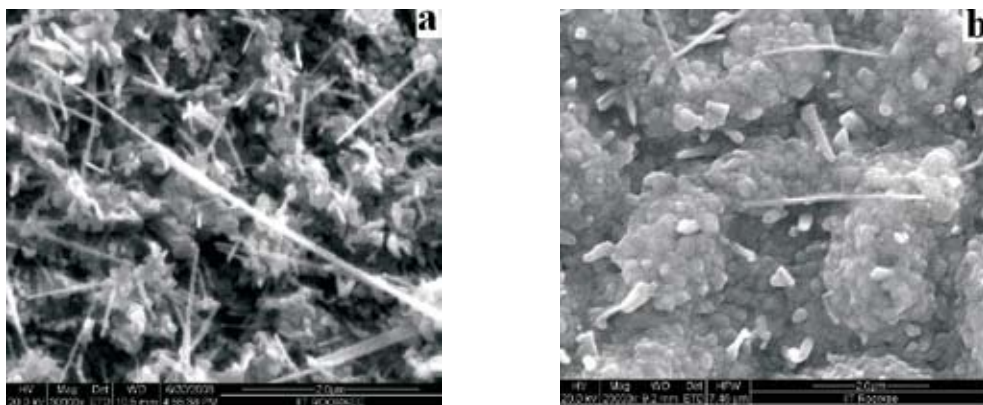


**Fig. 1. FESEM images of (a) pristine ZnO and (b) its irradiated counterpart.**

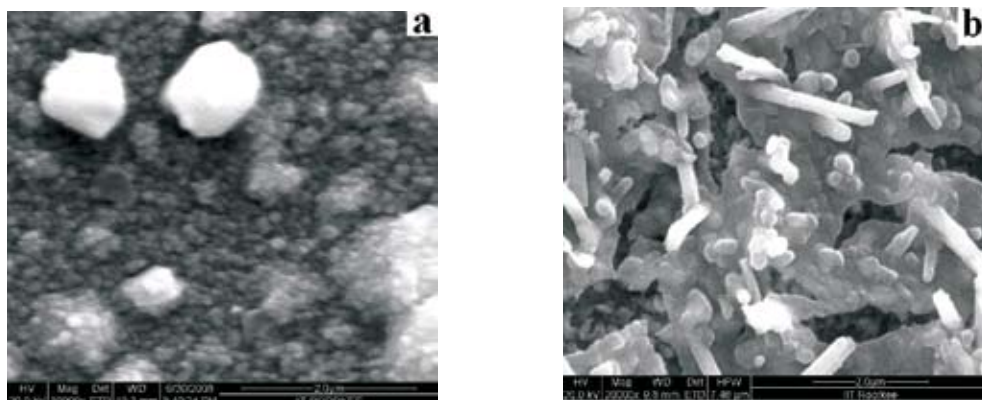


**Fig. 2. FESEM images of (a) pristine In<sub>2</sub>O<sub>3</sub> and (b) its irradiated counterpart.**

## REFERENCES

- [1] M. Sucheck, S. Christoulakis, K. Moschovis, N. Katsarakis, G. Kirakidis, *Thin Solid Films* 515 (2006) 551.
- [2] Z. Guo, J. Liu, Y. Jia, X. Chen, F. Meng, M. Li, J. Liu, *Nanotechnology* 19 (2008) 345704.
- [3] D.C. Agarwal, Amit Kumar, S.A. Khan, D. Kabiraj, F. Singh, A. Tripathi, J.C. Pivin, R.S. Chauhan, D.K. Avasthi, *Nucl. Instr. and Meth. B* 244 (2006) 136.
- [4] Mukesh Kumar, P G Ganesan, V N Singh, B R Mehta and J P Singh *Nanotechnology* 19 (2008) 175606 (6pp)

### 5.2.18 PEC Study on 100 MeV Si<sup>8+</sup> Ion Irradiated Nanostructured Fe<sub>2</sub>O<sub>3</sub>/TiO<sub>2</sub> bilayered Thin Films

Poonam Sharma<sup>1</sup>, Praveen Kumar<sup>1</sup>, Ambuj Tripathi<sup>3</sup>, Rohit Shrivastav<sup>2</sup>, Sahab Dass<sup>2</sup>, Vibha R. Satsangi<sup>1</sup>

<sup>1</sup>Department of Physics & Comp. Science, , Dayalbagh Educational Inst., Dayalbagh, Agra

<sup>2</sup>Department of Chemistry, Dayalbagh Educational Institute, Dayalbagh, Agra

<sup>3</sup>Inter University Accelerator Center, Aruna Asaf Ali Marg, New Delhi

Irradiation of metal oxide semiconductors with swift heavy ions can improve their photoelectrochemical (PEC) properties by creating favorable modification in the structural, morphological, optical and semiconducting properties [1]. We present an investigation on the effect of 100MeV Si<sup>8+</sup> ion irradiation on the photoelectrochemical properties of the nanostructured  $\alpha$ -Fe<sub>2</sub>O<sub>3</sub>/TiO<sub>2</sub> bilayered thin films prepared by the spray pyrolysis/sol-gel method respectively with respect to ion fluences ( $1 \times 10^{12}$ ,  $5 \times 10^{12}$ ,  $1 \times 10^{13}$  and  $2 \times 10^{13}$  ions/cm<sup>2</sup>). The photoelectrochemical study was carried out in three electrode configuration in which the unirradiated/irradiated samples served as working electrode (photoelectrode), Pt mesh as counter electrode and SCE as reference electrode, all immersed in 1M NaOH electrolytic solution [2]. These films were also characterized by X-ray diffraction (XRD), UV-visible absorption spectroscopy and atomic force microscopy (AFM).

XRD pattern for the unirradiated/irradiated samples confirmed the presence of hematite and anatase crystalline phase in the bilayered thin film of  $\alpha$ -Fe<sub>2</sub>O<sub>3</sub>/TiO<sub>2</sub>. No major change in the crystallinity and phase of the material was observed upon irradiation. The average value of crystalline size as calculated from the peaks of TiO<sub>2</sub> in XRD data was observed to decrease from ~30 nm for pristine sample to approximately ~22 nm for the sample irradiated at lowest fluence i.e.  $1 \times 10^{12}$  ions/cm<sup>2</sup>, afterward at higher fluence it again increased to ~30 nm.

Surface morphology as observed by AFM was also found to be affected by the fluence of irradiation. UV-visible optical absorption spectra indicate minor increase in the absorbance with increasing ion fluence upto  $5 \times 10^{12}$  ions/cm<sup>2</sup>.

Sample irradiated at fluence  $1 \times 10^{12}$  ions/cm<sup>2</sup> exhibited best photocurrent density of 0.89 mA/cm<sup>2</sup> at 0.5V/SCE. As-deposited bilayered photoelectrode exhibited open circuit photo-voltage,  $V_{oc}$  of ~112 mV and short circuit current,  $I_{sc}$  ~76  $\mu$ A/cm<sup>2</sup>. However, after irradiating at fluence  $1 \times 10^{12}$  ions/cm<sup>2</sup>,  $V_{oc}$  and  $I_{sc}$  increased to 406 mV and 485  $\mu$ A/cm<sup>2</sup> respectively, which may be attributed to the better separation of photogenerated charge carriers at the interface, reducing the charge carrier recombination. All these results collectively accounts for the better ability of irradiated bilayered films in water splitting as compared to unirradiated films.

## REFERENCES

- [1] Improved Photoelectrochemical Response of Titanium Dioxide irradiated with 120 MeV Ag<sup>9+</sup> ion”, J. of Phys. Chem. C, 114 (2010) 622.
- [2] Nanostructured Zn-Fe<sub>2</sub>O<sub>3</sub> thin film modified by Fe-TiO<sub>2</sub> for photoelectrochemical generation of hydrogen. Int. J. Hydrogen Energy, 35, 10883-10889, 2010.

### 5.2.19 200 MeV Ag<sup>16+</sup> ion irradiation effect on Ce doped nickel ferrite nanoparticles

Gagan Dixit<sup>1</sup>, J.P.Singh<sup>2</sup>, R.C.Srivastava<sup>1</sup>, H.M.Agarwal<sup>1</sup> and K.Asokan<sup>2</sup>

<sup>1</sup>G.B.Pant University of Ag. and Technology, Pantnagar, Uttrakhand

<sup>2</sup>Inter University Accelerator Centre, Aruna Asaf Ali Marg, New Delhi

The modification of magnetic oxides and ferrites by SHI got interest since last two decades [1]. Along with SHI, modifications in the structural, electrical and magnetic properties are obtained by introducing a relatively small quantity of rare earth ion [2]. Presently we are reporting the effect of irradiation of 200 MeV Ag<sup>16+</sup> beam on magnetic properties of pure and Ce doped nickel ferrite nanoparticles.

Nanoparticles of pure and Ce doped nickel ferrite were prepared by chemical route and irradiated with 200 MeV Ag<sup>16+</sup> beam at two fluences  $2 \times 10^{12}$  and  $1 \times 10^{13}$  ions/cm<sup>2</sup>. X-ray diffraction (XRD) pattern of pristine samples of NiFe<sub>2</sub>O<sub>4</sub> and NiCe<sub>0.04</sub>Fe<sub>1.96</sub>O<sub>4</sub> show pure spinel phase and no phase change was observed after irradiation. Magnetic hysteresis curves recorded at room temperature show that magnetisation is reduced after doping with Ce. After irradiation, the magnetisation was found to decrease but coercivity increases for both the systems. The change in magnetisation after the irradiation with the fluence of  $2 \times 10^{12}$  ions/cm<sup>2</sup> in nickel ferrite system is more significant than the Ce doped samples. Ce doped samples show significant change at high fluence  $1 \times 10^{13}$  ions/cm<sup>2</sup>.

**Table1: Crystallite size (D), Lattice parameter (a), X-ray density ( $\rho_x$ ), saturation magnetization ( $M_s$ ) and Coercivity ( $H_c$ ) of pristine and irradiated samples**

Parameters	NiFe <sub>2</sub> O <sub>4</sub>			NiCe <sub>0.04</sub> Fe <sub>1.96</sub> O <sub>4</sub>		
	Pristine	Fluence of irradiation (ions/cm <sup>2</sup> )		Pristine	Fluence of irradiation (ions/cm <sup>2</sup> )	
		$2 \times 10^{12}$	$1 \times 10^{13}$		$2 \times 10^{12}$	$1 \times 10^{13}$
<b>D (nm)</b>	36	32	36	17	16	18
<b>a (Å)</b>	8.31	8.32	8.32	8.29	8.29	8.31
<b><math>\rho_x</math> (g/cc)</b>	5.43	5.42	5.42	5.55	5.55	5.51
<b><math>M_s</math> (emu/g)</b>	40	33	32	39	36	31
<b><math>H_c</math> (Oe)</b>	61	174	97	14	28	50

## REFERENCES

- [1] Anjana Dogra, M.Singh, V.V.Siva Kumar, N.Kumar, Ravi Kumar, Nucl. Instr. Meth. B 212, 2003, 184-189
- [2] Lixi Wanga, Jie Song, Qitu Zhang,, Xiaogu Huang, Naicen Xu, J.Alloy & Comp. 481 (2009) 863

### 5.2.20 Evolution of surface topography of gold thin films by MeV Ni ion bombardment

P. Dash<sup>1</sup>, H. Rath<sup>1</sup>, P. Mallick<sup>1</sup>, Jai Prakash<sup>2</sup>, A. Tripathi<sup>2</sup>, D.K. Avasthi<sup>2</sup>, H. P. Lenka<sup>3</sup>, P.V. Satyam<sup>3</sup> and N.C.Mishra<sup>1</sup>

<sup>1</sup>Department of Physics, Utkal University, Bhubaneswar

<sup>2</sup>Inter-University Acceleration Centre, Aruna Asaf Ali Marg, New Delhi

<sup>3</sup>Institute of Physics, Bhubaneswar

Current studies have indicated that in metallic thin films and multi layers, the effects of electronic energy loss of swift heavy ions (SHI) are significantly enhanced as compared to bulk materials. Gupta and Avasthi [1] found an enhanced electronically mediated sputtering in Au thin films compared to the sputtering mediated through nuclear energy loss. Satpati et al [2] found higher sputtering in nano dispersed Au target than in continuous Au thin films when bombarded with 100 MeV Au ions. In the present study we probe into the evolution of surface topography of ultra thin Au (~ 20 nm) films deposited on float glass substrates. These films were bombarded by 58 MeV Ni ions.

Glancing angle X-Ray Diffraction pattern of these films showed that 58 MeV Ni ion irradiation did not cause much variation in the crystallite size. Irradiation roughened the surface at intermediate fluences and smoothed the same at high fluences [3]. The RBS spectra of 20 nm pristine and irradiated films at different fluences are shown in figure 1. The inset shows complete RBS image. Irradiation led to decrease of the of RBS peak height with ion fluence, which indicates that 58 MeV Ni ion irradiation causes sputtering from 20 nm thick Au film. Irradiation also led to tailing of the RBS peak into lower energy region. This tailing indicated irradiation induced diffusion at the film substrate interface. The sputtering yield was found to be 370 atoms per incident ion at lower fluence and at higher fluence it decreased found to 200 atoms per incident ion which was calculated from the fluence dependence of the number of gold atoms remaining in the film after a particular fluence of irradiation (figure 2). The reduced sputtering yield at high fluences may be a consequence of simultaneous occurrence of sputtering and radiation enhanced diffusion of Au in float glass substrate. If the later dominates at high fluences, the sputtering yield would decrease as observed.

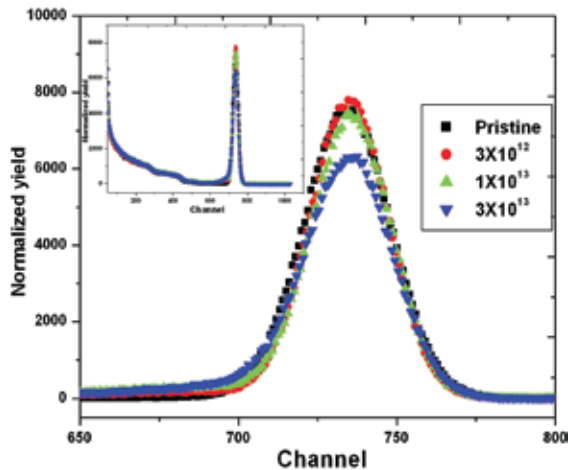


**Fig. 1. RBS spectra of as-deposited and sputtered 20 nm Au film at different fluences bombarded by 58MeV Ni ion**

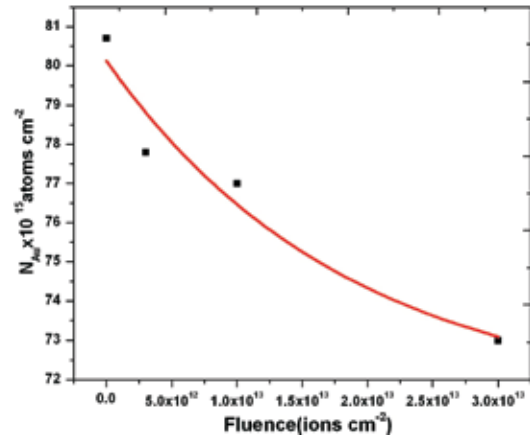


**Fig. 2. Variation of Au atoms in the film with ion fluence**

## REFERENCES

- [1] A. Gupta, D.K. Avasthi Physical Review B 64 (2001) 155407.
- [2] B. Satpati, J.Ghatak, B.Joseph, T.Som, D.Kabiraj, B.N.Dev, P.V. Satyam Nucl. Instrum. Methods Phys. Res. B 244 (2006) 278.
- [3] P. Dash, P. Mallick, H. Rath, A. Tripathi, Jai Prakash, D.K. Avasthi, S. Mazumdar, S. Varma, P. V. Satyam and N. C. Mishra, Appl. Surf. Sci. 256 (2009) 558–561.

### 5.2.21 Analysis of light and heavy ion irradiated Gallium Nitride epilayers grown using MOCVD Technique

S. Munawar Basha<sup>1</sup>, K. Asokan<sup>2</sup>, V. Ramakrishnan<sup>3</sup>, J. Kumar<sup>1</sup>

<sup>1</sup>Crystal Growth Centre, Anna University Chennai

<sup>2</sup>Inter-University Accelerator Centre, Aruna Asaf Ali Marg, New Delhi

<sup>3</sup>Department of Laser studies, Madurai Kamaraj University, Madurai

Gallium Nitride (GaN) is a semiconductor material with outstanding properties having a wide band gap of 3.4 eV and have high breakdown field (3MeV/cm). It is an important material for application in optoelectronics devices operating from red to ultraviolet range. Because of these advantages, it is very useful if these devices can operate at high energy radiation ambient in space. Based on this assumption, considerable amount of work has been carried to understand the effect of different ions like C, O, Fe, Ag etc on this material and to what extent it crystalline nature-survives to high energy ion beams [1]. It is observed that electrical, optical and structural properties of these materials can be modified distinctly with high energy ion beams [2,3]. The interaction of ion beam with material mainly depends

upon their energy, sample temperature, type of ion used and fluences. Depending upon the energy of the incoming ions, it can either displace the atoms by elastic collision or to excite the atoms by inelastic collision [4]. Raman scattering technique has been a powerful tool for studying the lattice dynamic and electronic properties of semiconductor superlattices, to characterize the crystalline quality of epitaxial layers. This article reports about XRD and the micro Raman studies of irradiated MOCVD grown GaN with oxygen  $O^{7+}$  and silver  $Ag^{12+}$  ion beam of energy 100MeV with fluences of  $1 \times 10^{12}$  and  $1 \times 10^{13}$  ions / $cm^2$  at room temperature.

Figure 1 shows the XRD pattern of pristine, light and heavy ions irradiated samples. It confirmed the wurtzite structure of GaN. There is no phase change on irradiation. But the decrease in their XRD intensity is observed due defect creations or *amorphous* nature in the epilayers compared with pristine sample [5]

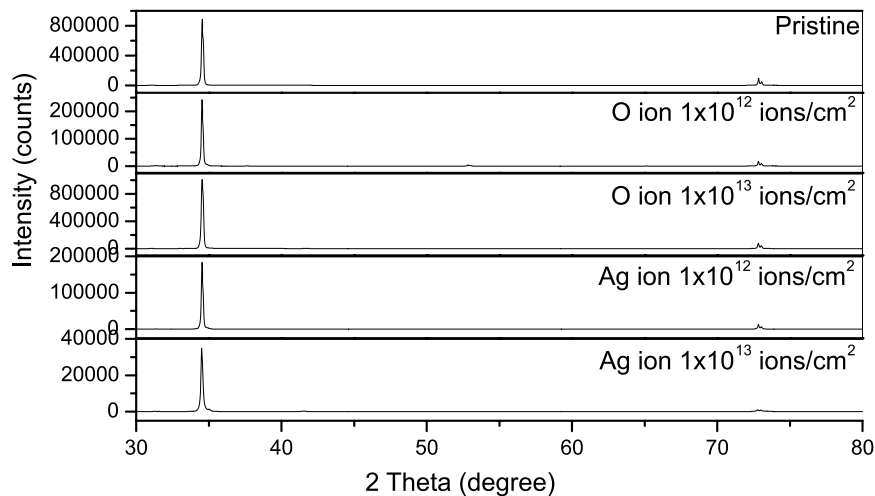


**Fig. 1. XRD pattern of pristine, Oxygen and Silver irradiated GaN epilayer with a fluence of  $1 \times 10^{12}$  and  $1 \times 10^{13}$  ions/ $cm^2$**

We investigated the micro Raman spectra of pristine and 100 MeV swift heavy ions namely oxygen and silver ions, irradiated at fluences of  $1 \times 10^{12}$  and  $1 \times 10^{13}$  ions/ $cm^2$  on MOCVD grown GaN epilayers. Further analysis is in progress.

## REFERENCES

- [1] K. Scherer, H. Fichtner, B. Heber, U. Mall, Space Weather, Lecture Notes in Physics, Springer, 2005, p. 656
- [2] S. O. Kucheyev, J. S. Williams, J. Zou, C. Jagadish and G.Li, Instr. And math.B. 2001;178, 209.
- [3] V Suresh Kumar, M Senthil Kumar, P Puviarasu, J. Kumar, T Mohanty, D Kanjilal, A Camarani, K Asokan, A Tripathi, M Fontana, Semicond. Sci. Technol. 2007 ;22 ,511.
- [4] X. Weng, S.J Clark, W.Yn, S.Kumar, R.S Goldman, A.Danial, R.Clark, J.Appl.Phys.2002, 92, 4012.
- [5] J. Bai, T. Wang, H. D. Li, N. Jiang and S. Sakai, Journal of Crystal Growth, 2001; 231,

## 5.2.22 Swift Heavy Ion Irradiation induced Surface Evolution of TiO<sub>2</sub> thin films

H. Rath<sup>1</sup>, P. Dash<sup>1</sup>, Jai Prakash<sup>2</sup>, D.K. Avasthi<sup>3</sup>, U.P.Singh<sup>4</sup> and N.C. Mishra<sup>1</sup>

<sup>1</sup>Department of Physics, Utkal University, Bhubaneswar, Orissa

<sup>2</sup>Departments of Chemistry, M. M. H College, Ghaziabad

<sup>3</sup>Inter-University Accelerator Center, Aruna Asaf Ali Marg, New Delhi

<sup>4</sup>KIIT University, Bhubaneswar

We show that grain size and surface topography in nanoparticle TiO<sub>2</sub> thin films undergo considerable modification under swift heavy ion (SHI) irradiation. Titanium oxide thin films of thickness  $\sim 100$  nm were deposited by spin coating of gel prepared with titanium isopropoxide [1]. A set of films annealed at 900 °C were irradiated by 200 MeV Ag ions at various fluences in the range  $3 \times 10^{11}$  to  $1 \times 10^{13}$  ions cm<sup>-2</sup> at room temperature using 15 UD Pelletron Accelerator at IUAC New Delhi. The films were studied by glancing angle x-ray diffraction (GAXRD) and atomic force microscopy (AFM). The nano-structured thin films, both pristine and irradiated films show dense granular microstructure with distinct grain boundary. The in-plane grain size distributions were fitted to a lognormal function, yielding the average grain size and the grain size dispersion (figure 1). The pristine film had grains of average size 54 nm with a grain size distribution ranging from 15 nm to 120 nm. Irradiation at the fluence of  $3 \times 10^{11}$  ions.cm<sup>-2</sup> narrowed the grain size distribution from 15 to 60 nm. This observation indicates that the smaller size grains remain unaffected under SHI irradiation while the larger size grains fragment thus decreasing the higher limit of grain size distribution. At this fluence the observed phenomenon is expected to be a consequence of single ion event. Increasing ion fluence to  $1 \times 10^{13}$  ions.cm<sup>-2</sup> leads to broadening of grain size distribution and the average grain size also increases to 66 nm. At high fluences, ion

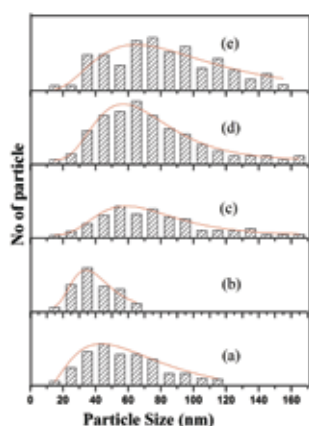


**Fig. 1. Size distributions of the grains after 200 MeV Ag ion irradiation with fluences of (a) 0 (pristine), (b)  $3 \times 10^{11}$  (c)  $1 \times 10^{12}$  (d)  $5 \times 10^{12}$  (e)  $1 \times 10^{13}$  ions cm<sup>-2</sup>**

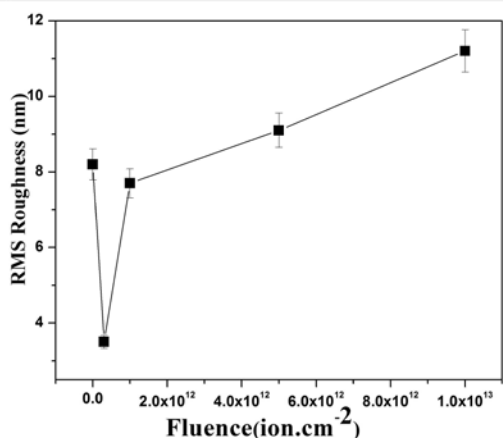


**Fig. 2. Evolution of RMS Roughness of the titanium oxide nanoparticle thin films with 200 MeV Ag ions irradiation fluence**

irradiation seems to induce grain growth as is seen from the increased average grain size and grain size distribution. The rms roughness decreased from 8.2 nm in pristine film to 2.8 nm in the film irradiated at fluence  $3 \times 10^{11}$  ions  $\text{cm}^{-2}$  (figure 2). Increasing irradiation fluence leads to increase of rms roughness as in the case of grain size distribution and average grain size at these fluences. Evolution of these parameters with ion fluence is modeled in terms of the confinement of SHI induced thermal spike in the small volume of a nanoparticle.

## REFERENCE

- [1] H. Rath, P. Dash, T. Som, P. V. Satyam, U. P. Singh, P. K. Kulriya, D. Kanjilal, D. K. Avasthi, and N. C. Mishra *J. Appl. Phys* 105, 074311 (2009)

### 5.2.23 Swift heavy ion induced modification of Gallium Phosphide surface

S. K. Dubey<sup>1</sup>, V. Jadhav<sup>1</sup>, M. D. Kirkire<sup>1</sup>, A.D. Yadav<sup>1</sup>, F. Singh<sup>2</sup> and D. Kanjilal<sup>2</sup>

<sup>1</sup>Department of physics, University of Mumbai, Mumbai

<sup>2</sup>Inter University Accelerator Centre, Aruna Asaf Ali Marg, New Delhi

With rising ion energy the electronic energy loss of the ions increases and at very high energies. It exceeds the nuclear one by two order of magnitude. Therefore the influence of the electronic energy deposition on materials modification needs to be studied systematically. It is well known that high electronic energy deposition during swift heavy ion irradiation in materials leads to the formation of amorphous track around the ion trajectories [1]. Gallium phosphide (GaP) is an indirect band gap (2.26 eV) semiconductor and is a basic material for optoelectronic applications. It also finds applications in photonic crystal devices which operate in the visible range. In present work, single crystal undoped GaP surfaces were irradiated by 200 MeV Ag ions from the 15 UD Pelletron facilities at Inter University Accelerator Centre (IUAC), New Delhi. The samples were irradiated with various ion fluences ranging from  $1 \times 10^{11}$  to  $2 \times 10^{13}$   $\text{cm}^{-2}$  at room temperature. The irradiation energy was chosen on the basis of SRIM calculation, which showed that the electronic energy deposition,  $S_e$ , of 200 MeV Ag ions in GaP is approximately two orders ( $42.81 \text{ eV}/\text{\AA}$ ) of magnitude higher than nuclear energy deposition,  $S_n$  ( $0.1181 \text{ eV}/\text{\AA}$ ). The vacuum inside the irradiation chamber was about  $10^{-4}$  Pa. The surface morphology of non-irradiated and samples irradiated with different fluences was examined using atomic force microscopy from Veeco's Di Innova model with silicon nitride tip. Different areas were scanned in the irradiated and non irradiated samples under ambient conditions in tapping mode. The scanned AFM images had  $256 \times 256$  point resolution. The Raman scattering measurements were performed on LabRAM HR micro-Raman spectrometer at room temperature using the 514.50 nm line of an argon ion laser in the back scattering geometry. Two dimensional and three dimensional AFM images of non irradiated and irradiated gallium phosphide samples for various fluences were recorded. The various parameters such as average roughness, root mean square

roughness, peak height, valley depth, surface skewness, and surface kurtosis have been estimated from the AFM data using SPIP software version 5.03. The positive value of surface skewness showed the predominance of peaks. The surface kurtosis ( $S_{ku}$ ) measure the distribution of spikes above and below the mean line. For spiky surface,  $S_{ku} > 3$  and for bumpy surface  $S_{ku} < 3$  [2]. This implied that the surface of GaP is spiky.

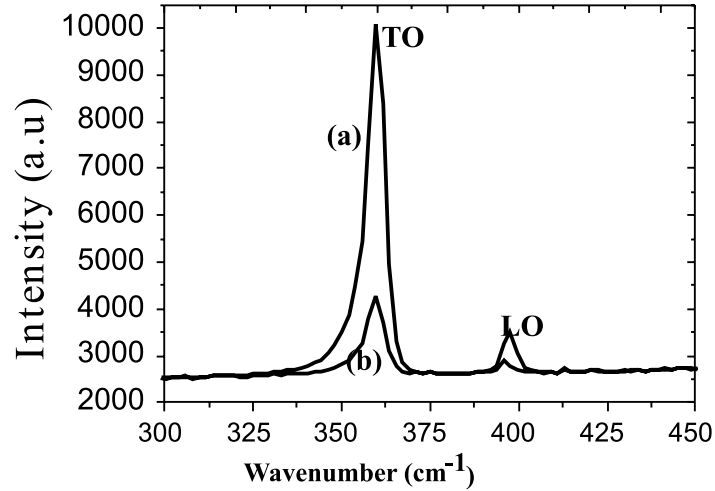


**Fig. 1. Raman spectrum of gallium phosphide; (a) non irradiated and (b) irradiated with 200 MeV with <sup>107</sup>Ag ions for the fluence of  $2 \times 10^{13}$  ions  $\text{cm}^{-2}$**

Raman spectra of the non-irradiated and samples irradiated with various ion fluences were recorded. The representative spectra of GaP irradiated with  $2 \times 10^{13}$  ions  $\text{cm}^{-2}$  along with non irradiated are shown in Fig 1. The spectrum of non-irradiated sample showed two peaks at  $359.85 \text{ cm}^{-1}$  and  $395.74 \text{ cm}^{-1}$ , which correspond to the characteristic LO and TO Raman modes of crystalline gallium phosphide respectively. The spectra obtained from the samples irradiated with various ion fluences showed decrease in the intensity of Raman peak. The peak position shifted towards the lower wave number. The decrease in the intensity indicates appearance of defects after ion irradiation. The shift of peak position indicates the presence of stress in the irradiated samples. The stress ( $\sigma$ ) in the sample irradiated with  $2 \times 10^{13}$  ions  $\text{cm}^{-2}$  estimated from the shift of the LO peak using the following relation

$$\sigma \text{ (MPa)} = -250 \Delta\omega \text{ (cm}^{-1}\text{)} \quad (1)$$

where  $\Delta\omega = \omega_s - \omega_0$ . In this expression,  $\omega_0$  and  $\omega_s$  denote the wave numbers of the non irradiated and irradiated gallium phosphide samples respectively. The value of stress calculated from the equation (1) for the sample irradiated with  $2 \times 10^{13}$  ions  $\text{cm}^{-2}$  was found to be 417.85 MPa.

## REFERENCES

- [1] W.Wesch, A. Kamarou, E. Wendler, Nucl. Instr. and Meth. B 225 (2004) 111.
- [2] Y.P Zhao, I. Wu, C.F. Ching, U. Block, G.C. Wang and T.M. Lu, Journal of Applied Physics 84 (1998) 2571.

### 5.2.24 100 MeV Ag ion irradiation on tin oxide thin films

R.S. Chauhan<sup>1</sup>, Vijay Kumar<sup>1</sup>, A. Gupta<sup>1</sup>, Deepti Pratap<sup>1</sup>, Anshul Jain<sup>1</sup>, D.C. Agarwal<sup>2</sup>, Ambuj Tripathi<sup>2</sup>, D.K. Avasthi<sup>2</sup>

<sup>1</sup> Department of Physics, R.B.S. College, Agra-282 002

<sup>2</sup> Inter University Accelerator centre, Aruna Asaf Ali Marg, New Delhi-110 067

Tin oxide is widely used in opto and microelectronic devices, gas sensing devices and as an oxidation catalyst. These wide varieties of remarkable properties and exciting applications make tin oxide special material for investigation and further modification [1-4]. In the present study, the modifications in structural, optical and surface morphological properties have been investigated on thin films of tin oxide due to the irradiation of 100 MeV Ag ions at different fluences.

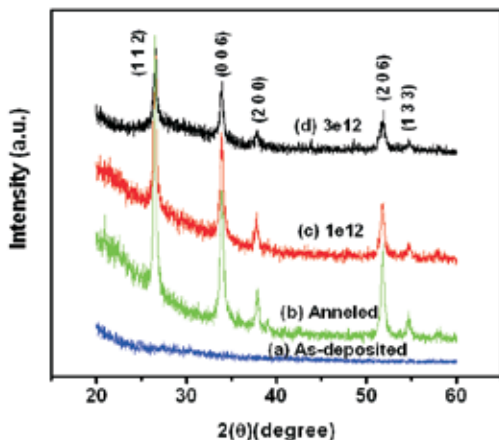
Tin oxide thin films (~100 nm) were deposited on quartz and Si substrates using thermal evaporation method. Some of the as-deposited films were also annealed in oxygen environment at 600°C for two hours. As-deposited and annealed films were irradiated using 100 MeV Ag ions at different fluences. These pre and post irradiated films were examined using X-ray diffraction (XRD), UV-Vis spectrophotometer and atomic force microscopy (AFM) for structural, optical and surface morphological study respectively.

Figure 1 shows the XRD pattern of the as-deposited, annealed and irradiated films. As deposited film is amorphous showing no reflection peaks. Annealing makes the film highly polycrystalline. The peak positions i.e. Bragg's angle( $2\theta$ ) were matched with the JCPDS card no. 78-1063. The observed data matches well with the standard data. All the peaks are attributed to the SnO<sub>2</sub> and there is no presence of Sn or SnO etc. This XRD pattern confirms the formation of orthorhombic tin oxide with cell parameters  $a=4.737\text{\AA}$ ,  $b=5.708\text{\AA}$  and  $c=15.86\text{\AA}$ . The average crystallite size (CS) was calculated using Scherrer formula [5] and was found ~23.26 nm. Irradiation at the fluences  $1\times 10^{12}$  and  $3\times 10^{12}$  ions/cm<sup>2</sup> has decreased the CS to ~22.00 and ~19.75 nm respectively. The decrement in CS implies the amorphization process.

Figure 2 shows the absorption spectra of the as-deposited, annealed and irradiated films. Band gap was estimated using the Tauc's procedure. The band gap of as-deposited film is ~2.5 eV and after annealing band gap has increased upto ~3.2 eV. This annealed film was irradiated at two fluences viz.  $1\times 10^{12}$  and  $1\times 10^{13}$  ions/cm<sup>2</sup>. There is no significant change takes place in band gap after irradiation at the lower fluence whereas it has decreased to ~2.4 eV after higher fluence irradiation.

The surface of as-deposited film is featureless as observed by AFM. The root mean square (rms) roughness is ~4.2 nm. Annealing has developed nanograins of tin oxide in the film. These nanograins are randomly distributed and have noticeable variation in size. The

average grain size and rms roughness is  $\sim 80.4$  nm and 19.9 nm respectively. Irradiation of the as-deposited film was done at  $1 \times 10^{12}$  and  $3 \times 10^{12}$  ions/cm<sup>2</sup>. The rms roughness is 9.3 and 6.4 nm for the  $1 \times 10^{12}$  and  $3 \times 10^{12}$  ions/cm<sup>2</sup> fluence irradiated films respectively. Some self-organized nanostructures have been developed on the surface with average grain size 126 nm and 109 nm at lower and higher fluence respectively.



**Fig.1.** XRD spectra of as-deposited, annealed and irradiated films.

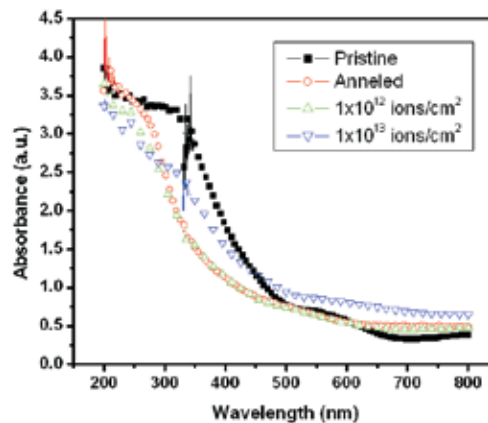


**Fig. 2.** Absorption Spectra of as-deposited, annealed and irradiated films.

## REFERENCES

- [1] R. Saniz, H. Dixit, D. Lamoen, B. Partoens; Appl. Phys. Lett. 97 (2010) 261901.
- [2] C. Kilic, A. Zunger; Phys. Rev. Lett. 88(9) (2002) 095501.
- [3] Z. M. Jarzebski, J.P. Marton; J. Electrochem. Soc. 123 (1976) 199C-205C, 299C-310C, 333C-346C.
- [4] M. Batzil; U. Diebold; Progress in Surface Science 79 (2005) 47.
- [5] A.S. Ryzhikov, R.B. Vasiliev, M.N. Rumyantseva, L.I. Ryabova, G.A. Dosovitsky, A.M. Gilmutdinov, V.F. Kozlovsky, A.M. Gaskov; Materials Science and Engineering B 96 (2002) 268.

### 5.2.25 Investigation of H/He Implantation-Induced Damage in AlN and InP

U. Dadwal<sup>1</sup>, R. Scholz<sup>2</sup>, M. Reiche<sup>2</sup>, D. Kanjilal<sup>3</sup>, P. Kumar<sup>3</sup> and R. Singh<sup>1</sup>

<sup>1</sup>Department of Physics, Indian Institute of Technology Delhi, New Delhi

<sup>2</sup>Max Planck Institute of Microstructure Physics, Weinberg 2, Halle, Germany

<sup>3</sup>Inter University Accelerator Centre, Aruna Asaf Ali Marg, New Delhi

The implantation-induced damage in 100 keV hydrogen and/or helium implanted AlN epitaxial layers and InP substrate was investigated for a fluencies in the range of  $(1-2) \times 10^{17}$  cm<sup>-2</sup>. The post-implantation thermal annealing behaviour of these samples was investigated using Nomarski optical microscopy, atomic force microscopy, stylus profilometry and cross-sectional TEM.

Our investigations showed that AlN samples that were implanted at LN<sub>2</sub> and RT exhibited mostly surface blistering after post-implantation annealing at 800 °C for 1h [1,2]. However, the AlN samples those were implanted at 100 and 300 °C showed large area exfoliation of the implanted surface after post-implantation annealing at same conditions [1]. The implantation-induced damage in AlN was analyzed by cross-sectional TEM, which revealed a damage band inside the AlN layer in all the cases that was decorated with hydrogen-filled nanovoids. These nanovoids showed a greater tendency of agglomerating together to form nanocracks in the as-implanted state for 100 and 300 °C implanted AlN samples leading eventually to the large area exfoliation after high temperature annealing [1].

On the other hand, cross-sectional TEM investigations of the InP samples revealed the formation of damage band incorporated with hydrogen-induced nanocracks and helium filled nanobubbles in the as-implanted state at LN<sub>2</sub> [3]. These helium filled nanobubbles were diffused from the narrow damage band towards the implanted surface [3].

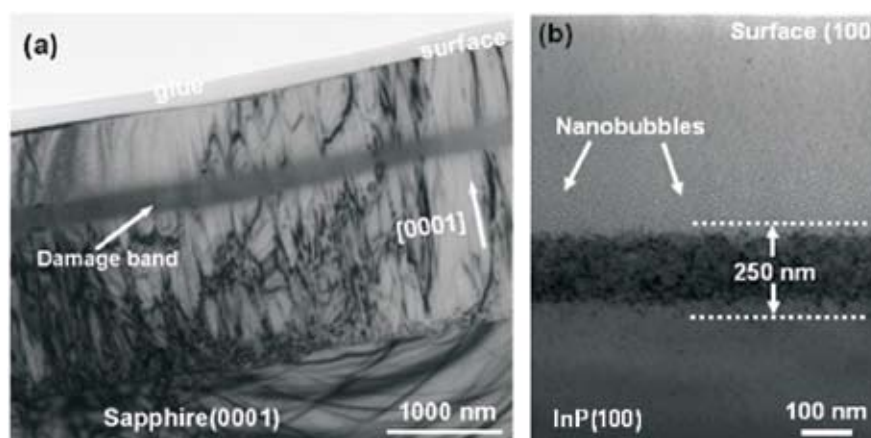


**Fig. 1. Cross-sectional TEM images of the 100 keV (a) H<sup>+</sup> implanted AlN and (b) He<sup>+</sup> implanted InP at LN<sub>2</sub> with a fluence of  $1 \times 10^{17} \text{ cm}^{-2}$  in the as-implanted state [1,3].**

## REFERENCES

- [1] U. Dadwal, R. Scholz, P. Kumar, D. Kanjilal, S. Christiansen, U Gösele and R. Singh, Phys. Stat. Sol. (a) 207, 29 (2010).
- [2] R. Singh, U. Dadwal, O. Moutanabbir, S. Christiansen and U Gösele, Phys. Stat. Sol. (c) 7, 44 (2010).
- [3] U. Dadwal, V. Pareek, R. Scholz, M. Reiche, S. Chandra and R. Singh, J. of Nano.-Electron. Phys. (in press).

### 5.2.26 SHI irradiation effects on properties of manganite based thin film devices

A.B. Ravalia<sup>1</sup>, K. Asokan<sup>2</sup> and D.G. Kuberkar<sup>1</sup>

<sup>1</sup>Department of Physics, Saurashtra University, Rajkot.

<sup>2</sup>Inter-University Accelerator Center, Aruna Asaf AliMarg, New Delhi

Discovery of Colossal Magneto Resistance (CMR) effect in doped mixed valent manganites have attracted the renewed interest due to the interesting interrelated properties exhibited by them [1]. The practical applications of CMR effect in manganites demand the exhibition of significant MR% [ $MR = (R_0 - R_H) * 100 / R_0$ ] in low applied fields at or around room temperature. Based on the possibility of observing large MR, under low fields, in thin film devices, we have fabricated p-type  $\text{La}_{0.6}\text{Pr}_{0.2}\text{Sr}_{0.2}\text{MnO}_3$  (LPSMO) / n-type  $\text{SrNb}_{0.2}\text{Ti}_{0.8}\text{O}_3$  (SNT0) bilayered device using pulsed laser deposition with varying thickness (50, 100 & 200 nm) of p-type manganite layer. [2].

200 MeV  $\text{Ag}^{+15}$  ions with  $5 \times 10^{11}$  and  $5 \times 10^{12}$  ions/cm<sup>2</sup> doses were bombarded on to the devices under study to understand the effect of irradiation on the modifications in structural strain, microstructural defect formation and magneto I-V behaviour of LPSMO/SNT0. XRD studies show that, in 100 nm LPSMO device, the structural strain increases on irradiation with  $5 \times 10^{11}$  ions which is evident from the suppression of the peak intensity while in 200 nm device, the XRD peak intensity ( Fig. 1) increases resulting in the improved crystallinity and hence reduction in strain. These observations are supported by the AFM studies. 100 nm devices exhibit the formation of regular columnar track like features on irradiating with  $5 \times 10^{11}$  ions leading to the structural strain. Resistivity measurements show a large suppression in its value after irradiation.

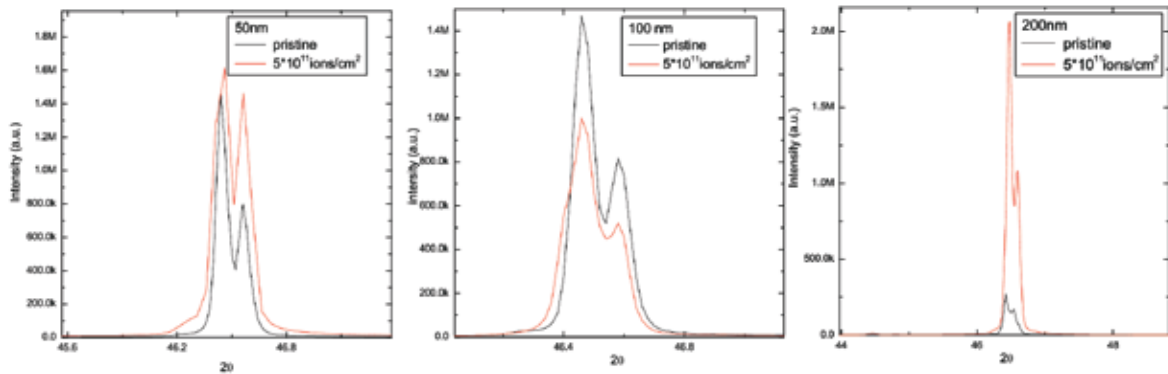


**Fig. 1. XRD pattern of Pristine and irradiated LPSMO/SNT0**

## REFERENCES

- [1] E. Dagotto, T. Hotta and A. Moreo, Phys. Rep. 344, 1 (2001).
- [2] P.S. Vachhani, J.H. Markana, R.J. Choudary, D.M. Phase, D.G. Kuberkar, Appl. Phys. Lett., 92, 043506(2008).

### 5.2.27 Effect of 150 MeV $\text{Ag}^{12+}$ ion beam irradiation on SBN thin films.

V.Mathivanan<sup>1</sup>, K.Asokan<sup>2</sup>, V.V.Sivakumar<sup>2</sup>, R. Mohan<sup>1</sup>

<sup>1</sup>Department of Physics, Presidency College, Chennai-600 005, India

<sup>2</sup>Inter University Accelerator Centre, Aruna Asaf Ali Marg, New Delhi

Strontium barium niobate (SBN)  $\text{Sr}_{0.75}\text{Ba}_{0.25}\text{Nb}_2\text{O}_6$  was synthesized by the conventional solid state reaction process [1]. The substances sintered at temperatures 1350°C, 1375°C, and 1400°C. The powder X-ray diffraction study confirms the single phase formation of SBN crystals at 1400°C. Thus prepared sample is used as target for thin film deposition by RF magnetron sputtering technique on p-type silicon substrates in Ar, O atmospheres. The thin films prepared were irradiated by 150MeV Ag ion beam. The pristine and irradiated samples were subjected to structural and optical characterizations. Atomic force microscopy was used to study morphology of the films.

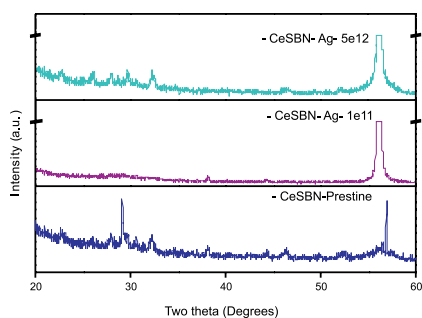


**Fig.1.**

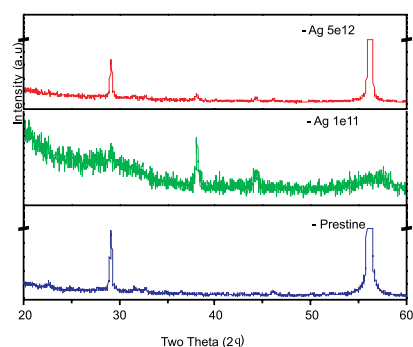


**Fig.2.**

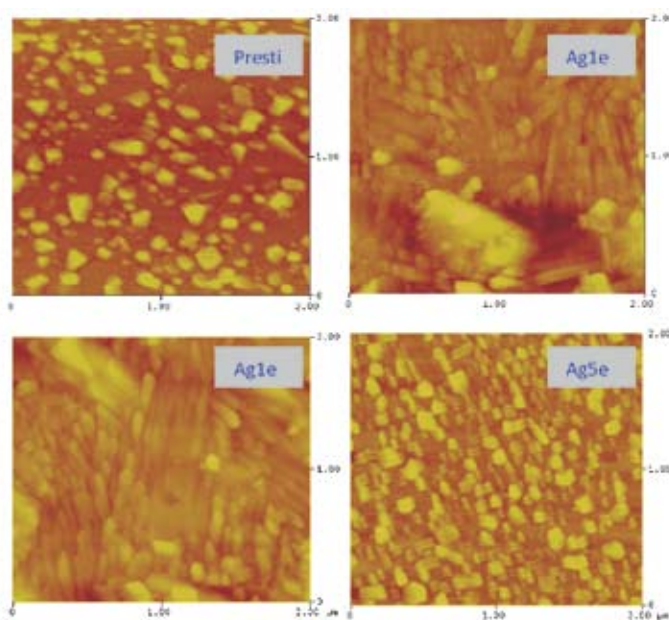


**Fig.3.**

Fig.1 & Fig.2 show the XRD pattern of unirradiated and 150 MeV Ag ion irradiated thin films of pure and Ce doped  $\text{Sr}_{0.75}\text{Ba}_{0.25}\text{Nb}_2\text{O}_6$ . It is seen in both the cases that the intensities of all diffraction peaks decreases with respect to the ion fluence[2]. Films get amorphized for  $10^{11}$  ions/cm<sup>2</sup> itself. As a result of amorphization new peaks emerges in the case of pure SBN films, also peak position shifts towards  $2\theta$  values as result of an enhanced out-of-plane lattice parameter [3]. We can say that there is no structural phase transition, but the ion irradiation only induces texturing which appears at an optimum fluence after complete amorphization.

Surface morphology of the films was investigated with help of atomic force microscopy, it is shown in fig. 3. From the figure it is evident that the surface morphology of the films has changed with respect to ion fluence. In fig. 3 one can find a rod like structures, this is due to radiation induced amorphization. This should not be misinterpreted with structural phase transition.

## REFERENCES

- [1] P.K. Patro. A.R.Lulkarni. C.S. Harendranath. *Ceramics International* 30 (2004) 1405-1409
- [2] Anjana Dogra. Ravi Kumar, V.V. Siva Kumar. N. Kumar. M. Singh. *Nuclear Instruments and Methods in Physics Research B* 225 (2004) 283–290
- [3] Ravi Kumara R. J. Choudhary. S. I. Patil. J. P. Srivastava. S. P. Sanyal. S. E. Lofland J. *Of Appl. Phys.* 96 (2004) 12

### 5.2.28 Effect of SHI Irradiation on Critical Current Density of $Y_{1-x}Ca_xBa_2Cu_3O_{7-\delta}$ Thick Film with $Y_2O_3$ Composite

Arpna Kujur<sup>1</sup>, P. Viswakarma<sup>1</sup>, Alok Banerjee<sup>2</sup>, D. Kanjilal<sup>3</sup> and D. Behera<sup>1</sup>

<sup>1</sup>Department of Physics, National Institute of Technology, Rourkela

<sup>2</sup>UGC-DAE-CSR Indore Centre, University Campus, Khandwa Road, Indore

<sup>3</sup>Inter University Accelerator Centre, Aruna Asaf Ali Marg, New Delhi

$Y_{1-x}Ca_xBa_2Cu_3O_{7-\delta}$  (YCaBCO) +  $Y_2O_3$  thick films were prepared by diffusion reaction technique. These films were irradiated with 200 MeV Ag ions with varying fluences. X-ray diffraction pattern of YCaBCO and YCaBCO+ $Y_2O_3$  composite at varying fluence shows c-axis oriented films. SEM shows sharp grain boundaries with small rounded crystal structure. Magnetization as a function of applied field for both unirradiated and irradiated samples was conducted at 40 K using VSM. Both in Ca doped and  $Y_2O_3$  composite films the intergrain critical current density  $J_c$  was calculated from Beans critical state Model [1], increases inspite of marginal lowering of  $T_c$  [2] But  $J_c$  decreases in YCaBCO +  $Y_2O_3$  composite with increasing irradiation doses. Interesting observation shows that unirradiated YCaBCO/ $Y_2O_3$  composite has the biggest magnetization width and thus the highest  $J_c$ . However, YCaBCO/ $Y_2O_3$  thick film irradiated with highest fluence of  $5 \times 10^{11}$  ions/cm<sup>2</sup> has the smallest magnetization width. Hence,  $J_c$  decreases in irradiated composite samples. Thereby giving a strong evidence that the synergetic effect of  $Y_2O_3$  creating defects and SHI producing columnar defects have resulted in degradation of superconducting volume fraction. Pinning force  $F_p = J_c \times H$  is calculated.  $F_p$  at certain low field has the maximum value and then starts decreasing with the increase in field. The highest flux pinning is exhibited by unirradiated YCaBCO/ $Y_2O_3$  composite sample ( $\sim 0.09$ GN/m<sup>3</sup>). For YCaBCO system,  $F_p$  increases immensely after irradiation with 200 MeV of Ag ions and is the maximum for fluence  $5 \times 10^{11}$  ions/cm<sup>2</sup>. Upon irradiation,  $F_p$  starts decreasing for YCaBCO/ $Y_2O_3$  system and attains the lowest value 0.012GN/m<sup>3</sup> for fluence  $5 \times 10^{11}$  ions/cm<sup>2</sup>, which is lower than YCaBCO pure system.

The defects around the latent track (columnar defects) generated due to secondary electrons emanating radially from the track play the dominant role over the pinning mechanism. Due to synergetic effect of Ag ions and  $Y_2O_3$  inclusions large number of

defects are introduced in YCaBCO/Y<sub>2</sub>O<sub>3</sub> composite due to which J<sub>c</sub> is observed to decline. Pinning force is the maximum for YCaBCO unirradiated. As the defects generated due to Y<sub>2</sub>O<sub>3</sub> and with columnar defects due to irradiation are more, the interaction energy between vortex and defects dominate over the pinning energy. Thus, the pinning sites are not used effectively thus, J<sub>c</sub> decreases with irradiation.

## REFERENCES

- [1] V.P.S. Awana, A. Vajpaye, M. Mudgel, H. Kishan, V. Ganesan, A.M. Awasthi, G.L. Bhalla. J. Euro. Phys. B. 62 (2008) 281
- [2] D. Behera, S.K. Dash, N.C. Mishra, Indian J. Phys. 77 ( 2003) 133.

### 5.2.29 Morphological and Photoelectrochemical Properties of 100MeV Si<sup>8+</sup> Ion irradiated Electrodeposited Iron Oxide Thin Films

Praveen Kumar<sup>1</sup>, Poonam Sharma<sup>2</sup>, Ambuj Tripathi<sup>3</sup>, Rohit Shrivastav<sup>2</sup>, Sahab Dass<sup>2</sup>, Vibha R. Satsangi<sup>1</sup>

<sup>1</sup>Department of Physics & Computer Science, Dayalbagh Educational Inst, Dayalbagh, Agra

<sup>2</sup>Department of Chemistry, Dayalbagh Educational Institute, Dayalbagh, Agra

<sup>3</sup>Inter University Accelerator Center, Aruna Asaf Ali Marg, New Delhi

Swift heavy ion irradiation is one of the possible methods to modify the material properties with respect to photoelectrochemical response (PEC) [1-2]. In search of better and efficient PEC material, present study was focused on the effect of 100 MeV Si<sup>8+</sup> ion irradiation on the PEC properties of electrodeposited iron oxide thin films. Undoped iron oxide thin films deposited over conducting glass substrate were irradiated with 100 MeV Si<sup>8+</sup> ions at fluence 1×10<sup>12</sup>, 5×10<sup>12</sup>, 1×10<sup>13</sup> and 2×10<sup>13</sup> ions/cm<sup>2</sup>. All the unirradiated/irradiated samples were used as photoelectrode in PEC cell and photocurrent were measured with respect to external electrode potential. 1M NaOH was used as electrolyte in the cell. Structural, optical and electrical properties were also studied using XRD, SEM, UV-Vis absorption spectroscopy.

XRD pattern of pristine sample confirmed the exclusive formation of hematite phase and no major change in the phase was observed after irradiation. Relative intensity of all hematite peaks was observed to increase up to ion fluence up to 5× 10<sup>12</sup> ion/cm<sup>2</sup>, indicating improvement in the crystallinity of the material due to irradiation. SEM micrograph of unirradiated sample exhibited the granular, dense and uniform morphology. Irradiation of material at lower fluence up to 5× 10<sup>12</sup> ion/cm<sup>2</sup> resulted in an increase in the grain size, whereas at higher fluence grain fragmentation occurred, leading to reduction in grain size from 48 nm to 19 nm. UV-Vis spectroscopy indicated a marginal red shift in the absorption edge upon irradiation.

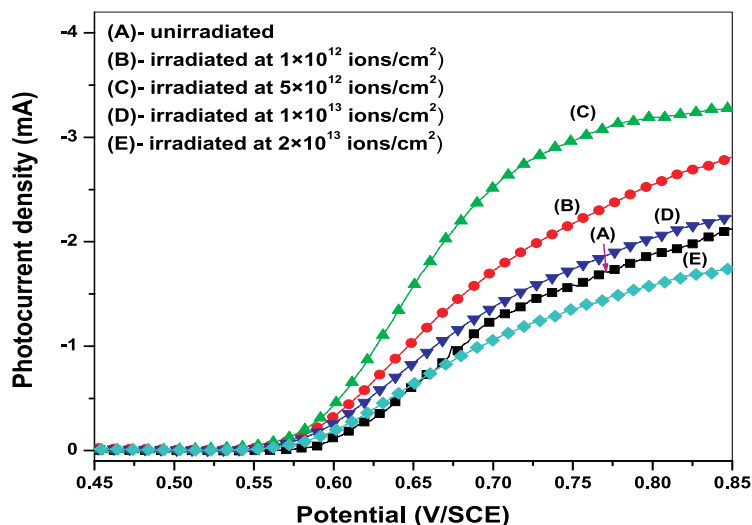


**Fig. 1. Photocurrent densities versus applied potential curve for various thin films**

Photocurrent density versus applied electrode potential curves for all the samples has been presented in Fig 1. With increase in ion fluence up to  $5 \times 10^{12}$  ions/cm<sup>2</sup>, photocurrent density was observed to increase, afterward it decreased. The sample irradiated at fluence  $5 \times 10^{12}$  ions/cm<sup>2</sup> exhibited the maximum photocurrent density of 3.0 mA/cm<sup>2</sup> at 0.75 V/ SCE. This improvement in the photoresponse may be attributed to better crystallinity of the material, and red shift of absorption edge due to irradiation.

## REFERENCES

- [1] A.P. Singh, S. Kumari, R. Shrivastav, S. Dass, Vibha R. Satsangi, Improved photoelectrochemical response in hematite by high energy Ag<sup>9+</sup> ions irradiation, *J. Phys. D: Applied Physics*. 42 (2009) 085303-085308.
- [2] Y.S. Chaudhary, S.A. Khan, R. Shrivastav, V.R. Satsangi, S. Dass, S. Prakash, U.K. Tiwari, D.K. Avasthi, N. Goswami, S. Dass, Modified structural and photoelectrochemical properties of 170 MeV Au<sup>13+</sup> irradiated hematite, *Thin Solid Film*. 492 (2005) 332-336

### 5.2.30 Swift heavy ions beam induced modifications in thin films of Ba(Fe<sub>0.5</sub>Nb<sub>0.5</sub>)O<sub>3</sub> (BFN) relaxor dielectrics

Bhagwati Bishnoi<sup>1</sup>, Devang Shah<sup>1</sup>, P.K. Mehta<sup>1</sup> and Ashokan<sup>2</sup>

<sup>1</sup>Department of Physics, The M.S. University of Baroda, Vadodara

<sup>2</sup>Inter-University Accelerator Center, Aruna Asaf Ali Marg, New Delhi

A complex ceramic compound Ba(Fe<sub>0.5</sub>Nb<sub>0.5</sub>)O<sub>3</sub> (BFN) having double perovskite structure is widely studied due to its vast application area in modern electronic industries like; capacitor industries, wireless communication, sensor applications, etc. [1-3]. This compounds exhibit point defect dependent dielectric parameters providing good opportunity

to study substitution effects on its physical parameters. It is well known that materials properties are mainly controlled by the inherent defects or charge carriers produced during processing itself. Swift Heavy Ion irradiation can create defects in controlled way when material is subjected to irradiation by selected radiation of appropriate energy and fluence [4]. Further, thin film devices made of Relaxor dielectrics are characterized by charge transport and dielectric relaxation phenomenon, for both practical and scientific reasons. We would like to correlate structural modifications by swift heavy ion irradiation with phase variation effects in dielectric and transport measurements as a function of temperature.

We synthesized BFN thin films using PLD technique on ITO coated glass substrate. The As deposited films were annealed in air atmosphere at 600 °C up to 1 hour for better crystallinity [5]. The SHI irradiation study was performed using Pelletron accelerator at IUAC, New Delhi. Films were irradiated at room temperature using  $O^{+7}$  ions having energy of 98 MeV for three different fluences viz.  $1 \times 10^{12}$ ,  $5 \times 10^{12}$  and  $1 \times 10^{13}$  ions per  $cm^2$ . The structural properties and surface morphologies of pristine film (BFN-2P) along with irradiated films BFN-2A (fluence  $1 \times 10^{12}$  ions per  $cm^2$ ), BFN-2B (fluence  $5 \times 10^{12}$  ions per  $cm^2$ ), and BFN-2C (fluence  $1 \times 10^{13}$  ions per  $cm^2$ ) were studied using XRD and AFM measurements. X-ray diffraction measurements were done at CSR Indore, using Bruker D8 advance X-ray diffractometer. The UV-Vis spectroscopic measurements of the films were done at room temperature in the range of 300 nm to 850 nm. Further, the electrical characterization of films were done using SOLARTRON 1260 impedance analyzer in the frequency range of 1 Hz to  $1 \times 10^7$  Hz with temperature variation from 20 °C to 450 °C.

In BFN films, with single cubic phase, the crystallite size drastically falls to ~13 nm compared to bulk (~113 nm). Swift Heavy Ion (SHI) irradiation on BFN of  $O^{+7}$  ions up to fluence of  $1 \times 10^{13}$  ions per  $cm^2$  does not show any crystal or morphological structural changes in the film, signifying material's stability up to the above ion dose. BFN compound exhibit its band gap in wide band semiconductor region (3.53eV). A prominently large NTCR to PTCR transitions at 350 °C whose origin is a temperature dependent structure linked electrical/magnetic phase transition rather than a local fluctuating defects makes BFN film a promising candidate as switching device. Further, the switching temperature can also be modified using appropriate SHI irradiation fluence.

## REFERENCES

- [1] Z. Wang, X. M. Chen, L. Ni, and X. Q. Liu, *App. Phys. Lett.* 90, (2007) 022904.
- [2] I.P. Raevski, S.A. Prosandeev, A.S. Bogatin, M.A. Malitskaya, L. Jastrabik, *J. Appl. Phys.* 93, (2003) 4130.
- [3] Z. Wang, X.M. Chen, L. Ni, X.Q. Liu, *Appl. Phys. Lett.* 90, (2007) 022904.
- [4] M. G. Blamire, J. L. MacManus-Driscoll, N. D. Mathur, and Z. H. Barber, *Adv. Mater.* 21, (2009) 3827.
- [5] S. T. Tan, B. J. Chen, X. W. Sun, W. J. Fan, H. S. Kwok, X. H. Zhang and S. J. Chua, *J. Appl Phys.* 98, (2005) 013505.

### 5.2.31 AC Conduction and Dielectric Relaxation in Polypyrrole Irradiated with SHI of $\text{Ag}^{8+}$

Amarjeet Kaur<sup>1</sup>, Anju<sup>1</sup>, D.K. Avasthi<sup>2</sup>

<sup>1</sup>Department of Physics and Astrophysics, University of Delhi, Delhi

<sup>2</sup>Inter University Accelerator Center (IUAC), Aruna Asaf Ali Marg, New Delhi

The mechanism of ac conduction in these SHI irradiated conducting polymers have been thoroughly investigated for the first time. Polypyrrole (PPY) irradiated with 100 MeV  $\text{Ag}^{8+}$  shows remarkable changes in its dielectric values. Huge increases in static dielectric constant have been observed for 100MeV  $\text{Ag}^{8+}$  SHI beam irradiated polypyrrole as shown in Fig 1.

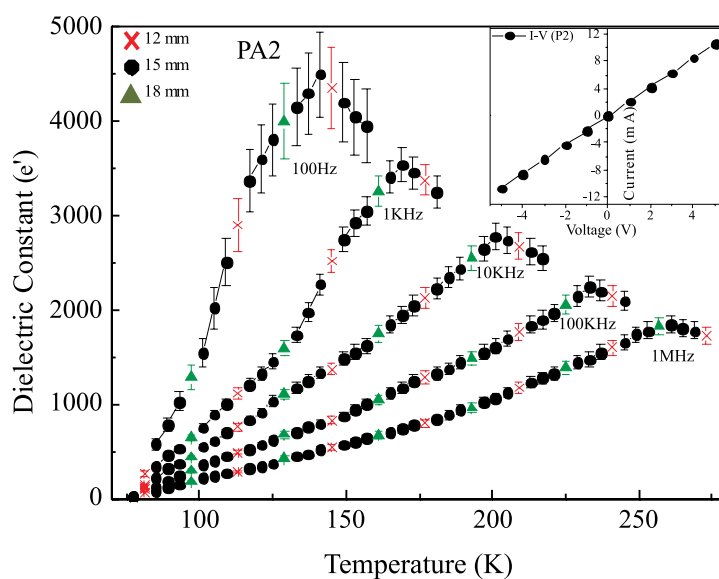


**Fig. 1.** Dielectric constant  $\epsilon'(\omega)$  as a function of temperature at five fixed frequencies) for 100 MeV  $\text{Ag}^{8+}$  ion beam irradiated PPY (ion fluence at  $10^{11}$  ions /  $\text{cm}^2$ ) at the three different thicknesses of 12, 15 and 18  $\mu\text{m}$ . The vertical bars represent uncertainty.

The dielectric behaviour is true bulk type and Ag ion beam modifies polypyrrole by introducing the large number of defects. These defects are responsible for mechanism of ac and dc conduction which originate from same hopping process. The variation of ac conductivity with temperature of 100 MeV  $\text{Ag}^{8+}$  ion beam irradiated at the fluence of  $10^{11}$  ions/ $\text{cm}^2$  is given in Fig 2. The measured ac conductivity and dielectric constant in the temperature region 77-300K show two distinct mechanisms. In low temperature region polaronic hopping is based on a linear dependence of conductivity on frequency. At higher temperatures the mechanism contributes to distribution of relaxation times giving rise to broad dielectric loss peaks. In the temperature region where  $\sigma_m(\omega)$  approaches  $\sigma_{dc}$  the variation of dielectric constant with temperature and frequency gives the estimate of the

characteristic relaxation frequency  $f_0$ . Such materials having giant dielectric constant find their place in semiconductor industry for the development of high density random access memories (RAMs) based on capacitors.

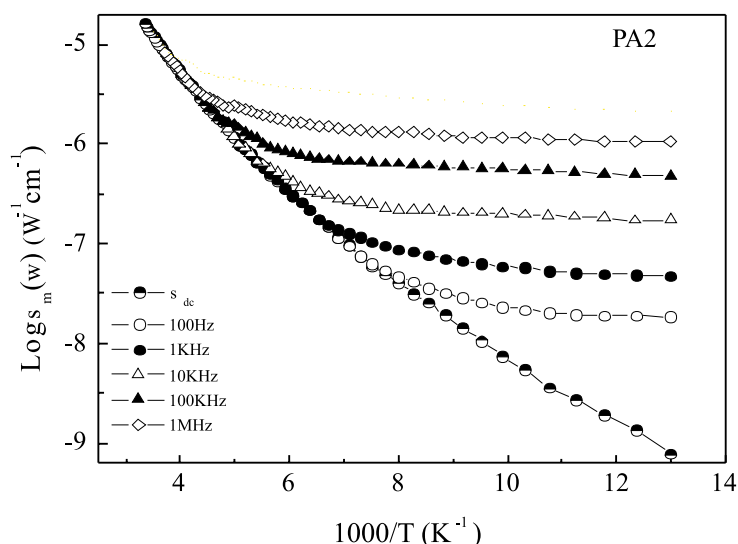


**Fig.2. Measured AC conductivity  $\sigma_m(\omega)$  as a function of reciprocal temperature at five fixed frequencies for 100MeV  $\text{Ag}^{8+}$  SHI beam irradiated PPY (PA2).**

### 5.2.32 Effect of Ar ion implantation on structural and optical properties of $\text{WO}_3$ thin films

Sunita Keshri and Ashutosh Kumar

Dept. of Applied Physics, Birla Institute of Technology, Mesra, Ranchi, Jharkhand

We have prepared  $\text{WO}_3$  thin films on unheated corning glass and silicon substrates by physical vapour deposition method using e-beam; followed by annealing at temperatures 300°C and 500°C for 1 h in oxygen atmosphere. The as grown  $\text{WO}_3$  film is amorphous whereas after annealing at 300°C and 500°C in oxygen atmosphere the crystallinity of the film gets improved. After annealing, the  $\text{WO}_3$  films show monoclinic phase that is described by space group  $P_{21}/C$  (14) and lattice parameters are:  $a=5.2610\text{Å}$ ,  $b=5.1358\pm 0.0189\text{Å}$ ,  $c=7.6500$  and  $\beta=92.051$ , as calculated by ‘Checkcell’ software. It has been observed that the film annealed at 300°C present good adhesion to both glass and Si substrates. The films show semiconducting behaviour, as confirmed by temperature dependent conductivity experiment.

The  $\text{WO}_3$  thin films, annealed at 300°C have been irradiated by Ar ion with fluences ranging between  $3\times 10^{15}$  to  $1\times 10^{17}$  ions/cm<sup>2</sup>, using LEIBF. The structural, optical transmittance and photoluminescence (PL) properties of the films have been thoroughly studied before and after irradiation. The films grown on glass substrate show high optical

transmittance (upto 78%) in the visible-infrared spectral range. Large increase of PL has been observed in the sample irradiated with  $1 \times 10^{16}$  ions/cm<sup>2</sup>. The Raman Spectroscopy of the samples has been carried out at IUAC. Thorough analysis of these results as well as some more studies on irradiated films are under process. We believe that these preliminary characteristic observations on the irradiated WO<sub>3</sub> films will be helpful to explore the device performance of the films for electrochromic and smart window applications.

### **5.2.33 Corrosion study of surface modified Ti by ion implantation in stimulated body fluid**

Suresh Kadam<sup>1</sup>, Kailash R. Jagdeo<sup>2</sup>, D. Kanjilal<sup>3</sup>, Pravin Kumar<sup>3</sup>, M. R. Nair<sup>4</sup>

<sup>1</sup>Dept. of Physics, KET's V. G. Vaze College, Mumbai (MS)

<sup>2</sup>Dept. of Physics, DSPM's K. V. Pendharkar College, Dombivli (MS)

<sup>3</sup>Inter University Accelerator Centre, Aruna Asaf Ali Marg, New Delhi

<sup>4</sup>Principal, Model College, Dombivli (MS)

Titanium and titanium alloys are widely used as surgical and dental materials for their excellent mechanical and physical properties. However, the application of Ti alloys is limited by their relatively low wear and chemical resistance in biological environment. The release of particles or elements from the alloy into the surrounding cells or tissues can cause inflammation. Therefore, surface engineering is required for improving the functional properties of these materials. In this study, Nitrogen was implanted by process of ion implantation at 60 keV with different fluences of  $1 \times 10^{16}$ ,  $5 \times 10^{16}$  and  $1 \times 10^{17}$  ions/cm<sup>2</sup>. Corrosion resistance of Ti and ion implanted Ti were investigated by an electrochemical test, at 37°C temperature in Normal Saline and Ringer Lactate solution. Tafel extrapolation method was used for calculating corrosion rate. As fluences increase corrosion resistance increases in stimulated body fluid.

The direct Nitrogen ion implantation was done at LEIBF, IUAC, New Delhi, India. Nitrogen ion implantation on NiTi, Ti6Al4V, Pure Ti and 316L stainless steel at energy of 60KeV was carried out at different fluences of  $1 \times 10^{16}$ ,  $5 \times 10^{16}$  and  $1 \times 10^{17}$  ions/cm<sup>2</sup>. Before ion implantation, samples were ultrasonically cleaned with acetone.

Corrosion resistance of all ion implanted samples was investigated by Tafel extrapolation method. Tafel curves were obtained through Gamry-Potentiostat/Galvanostat (reference 3000).  $I_{\text{corr}}$ ,  $E_{\text{corr}}$ ,  $\beta_a$ ,  $\beta_c$  and corrosion rate was obtained by Tafel fit and DC corrosion software. The electrochemical measurements were performed in a standard three-electrode cell with platinum counter electrode and a saturated calomel electrode (SCE) as reference electrode with scan rate of 1mV/s. The electrochemical tests were carried out at 37° C in Ringer Lactate solution and Normal Saline solution (0.9% NaCl). Surface

characterization using XRD, EDAX/SEM of some samples is completed. ICPAES study is going on.

### 5.2.34 140 MeV Silicon Ion Irradiation Effects on the I-V Characteristics of NPN RF Power Transistors

N. Pushpa<sup>1</sup>, K. C. Praveen<sup>1</sup>, A. P. Gnana Prakash<sup>1</sup>, Ambuj Tripathi<sup>2</sup>, S.K.Gupta<sup>3</sup> and D. Revannasiddaiah<sup>1</sup>

<sup>1</sup>Department of Studies in Physics, University of Mysore, Manasagangotri, Mysore

<sup>2</sup>Inter University Accelerator Centre, Aruna Asaf Ali Marg, New Delhi

<sup>3</sup>Technical Physics Division, Bhabha Atomic Research Centre, Mumbai

The present technology evolves toward the creation of faster and less power consuming radiation-resistant semiconductor devices for different radiation environments like space and large hadron collider (LHC). The semiconductor devices need to have exposure to ionizing radiation and need to be radiation hardened from 10's of krad to 100's of Mrad of total dose. Testing the devices using conventional gamma and proton sources are time consuming and expensive. Alternatively, one can irradiate devices with high energy ions which reduces the irradiation time and cost. In the present work, we have irradiated silicon NPN *RF* Power transistors (BEL 2N 3866) with 140 MeV Si<sup>10+</sup> ions in the total dose ranging from 100 krad to 100 Mrad. The different electrical characteristics like gummel characteristics, excess base current ( $\Delta I_B$ ), DC current gain ( $h_{FE}$ ), damage constant (K), transconductance ( $g_m$ ) and output characteristics were studied before and after ion irradiation. Figure 1 illustrates the DC current gain ( $h_{FE}$ ) for 140 MeV Si<sup>10+</sup> ion irradiated transistors. From the figure it is clear that the  $h_{FE}$  of the irradiated transistors reduces almost to a negligible value after a total dose of 100 Mrad. The  $h_{FE}$  degradation of the transistor occurs in two ways, one is bulk degradation and the other is ionization in the passive oxide layer. The bulk degradation occurs due to atomic displacement in the bulk of the transistor when incoming energetic ion transfers momentum to the atoms of the target silicon. If sufficient energy is transformed, the silicon atom can be ejected from its location, leaving a vacancy or defect. The generation-recombination (G-R) centers in the base region of the transistors reduce the minority carrier lifetime and this in turn increase the  $I_B$  and decrease the  $h_{FE}$ . From Figure 2, it can be seen that  $g_m$  decreases with increase in Si<sup>10+</sup> ion dose. The  $I_C$ - $V_{CE}$  characteristics of 140 MeV Si<sup>10+</sup> ion irradiated transistors measured at  $I_B = 0.75$  mA is shown in Figure 3 up to a total dose of 100 Mrad. From this figure it can be seen that the  $I_C$  at saturation region decreases with increase in ion dose. The degradation in the electrical characteristics of the transistors is mainly due to generation-recombination centers created in E-B spacer oxide (SiO<sub>2</sub>) and displacement damage in the bulk of the transistor structure.

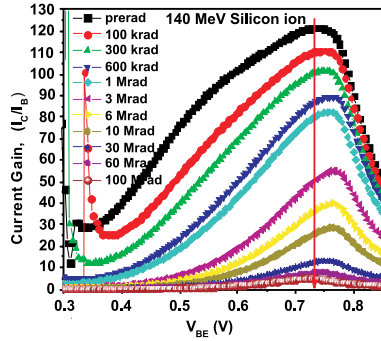


Fig. 1. The variation in  $dc$  current gain

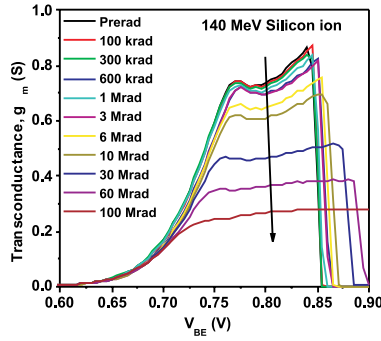


Fig.2. Variation of transconductance ( $g_m$ ) with base emitter voltage ( $V_{BE}$ )

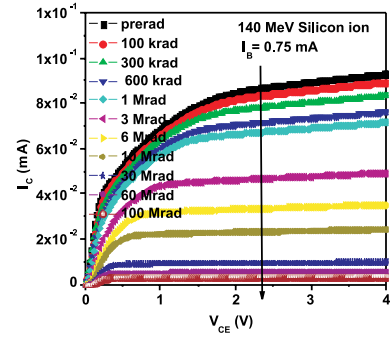


Fig. 3. The collector-emitter voltage versus collector current at  $I_B = 0.75$  mA

## REFERENCE

- [1] N. Pushpa *et. al* 2010, Nucl. Instrum. Meth. A. Vol.620, pp 450-455, 2010.

### 5.2.35 The effect of 140 MeV Silicon Ion Irradiation on Subthreshold and Transconductance Characteristics of N-channel Depletion MOSFETs

N. Pushpa<sup>1</sup>, K. C. Praveen<sup>1</sup>, A. P. Gnana Prakash<sup>1</sup>, Ambuj Tripathi<sup>2</sup>, S.K.Gupta<sup>3</sup> and D. Revannasiddaiah<sup>1</sup>

<sup>1</sup>Department of Studies in Physics, University of Mysore, Manasagangotri, Mysore

<sup>2</sup>Inter University Accelerator Centre, Aruna Asaf Ali Marg, New Delhi

<sup>3</sup>Technical Physics Division, Bhabha Atomic Research Centre, Mumbai

The N-channel metal oxide semiconductor field effect transistors (3N187 MOSFETs) considered for the present work are used in military and communication equipments. Therefore understanding the radiation effects on these devices is important. In present work we have studied the effects of 140 MeV  $Si^{10+}$  ion irradiation on various electrical characteristics of the MOSFETs. It is well known that MOSFETs are sensitive to radiation and prone to parametric and even functional failure up on exposure. The basic damage effects of ionizing radiation in MOS devices results from the generation of interface and oxide trapped charge in the gate oxide. These trapped charge degrades the important parameters of MOSFETs such as threshold voltage ( $V_{TH}$ ), transconductance ( $g_m$ ) and mobility of carriers ( $\mu$ ) in the channel. Several literatures have addressed the Co-60 gamma, electron and proton irradiation effects on MOSFETs but the high energy ion irradiation effects on MOS devices is sparse, especially total dose effects. High energy ions have higher LET than Co-60 and electrons and create defect complexes in addition to ionization. In present work we have tried to understand the effects of large LET difference of Co-60 gamma and  $Si^{10+}$  ion irradiation on N-channel MOSFETs at

higher total doses. The main objective of this work is to investigate the effects of 140 MeV  $\text{Si}^{10+}$  ion on  $V_{\text{TH}}$ ,  $g_m$  and the mobility ( $\mu$ ) of carriers in the channel and compare with the Co-60 gamma irradiated MOSFETs. Figure 1 shows the subthreshold ( $I_D$ - $V_{\text{GS}}$ ) characteristics of 140 MeV  $\text{Si}^{10+}$  ion irradiated MOSFETs at  $V_{\text{DS}} = 1$  V. It can be seen from the figure that  $I_D$  swings towards negative voltage with increase in dose. This means  $V_{\text{TH}}$  decreased with increase in total dose. Also it can be seen that the leakage current is found to increase with increase in total dose. Figure 2 shows the variation in peak transconductance ( $g_{m \text{ peak}}$ ) for MOSFETs irradiated with 140 MeV  $\text{Si}^{10+}$  ions and Co-60 gamma radiation for different total doses. It can be observed that there is a significant decrease in  $g_{m \text{ peak}}$  after irradiation. The mobility of carriers in channel is directly proportional to  $g_m$ , therefore one can say mobility of electrons are also decreased after irradiation.

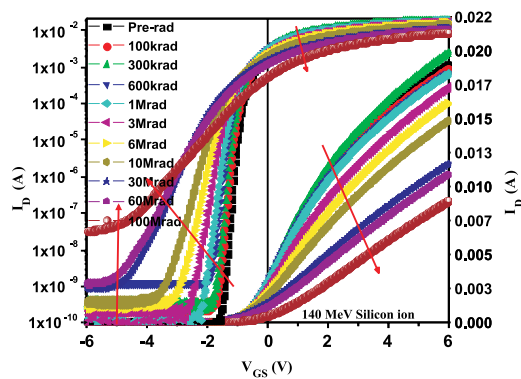


**Fig. 1. Subthreshold characteristics of 140 MeV  $\text{Si}^{10+}$  ion irradiated MOSFET**

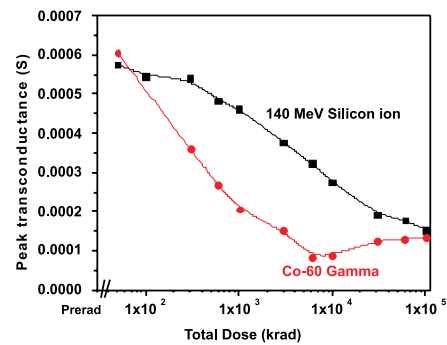


**Fig. 2. Peak transconductance versus total dose for  $\text{Si}^{10+}$  ion and Co-60 Gamma irradiated MOSFETs.**

## REFERENCE

- [1] N. Pushpa *et. al* 2010, Nucl. Instrum. Meth. A 613(2) 280

### 5.2.36 Assessment of 50 GHz SiGe HBTs for Harsh Radiation Environment by Heavy Ion Irradiation

K. C. Praveen<sup>1</sup>, N. Pushpa<sup>1</sup>, John D Cressler<sup>3</sup>, Ambuj Tripathi<sup>2</sup> and A. P. Gnana Prakash<sup>1</sup>

<sup>1</sup>Department of Studies in Physics, University of Mysore, Manasagangotri, Mysore

<sup>2</sup>Inter University Accelerator Centre, Aruna Asaf Ali Marg, New Delhi

<sup>3</sup>School of Electrical and Computer Engineering, Georgia Inst. Tech. Atlanta, USA

This work aims at the assessment of first generation (50 GHz) Silicon-Germanium Heterojunction Bipolar Transistor for harsh radiation environment. The SiGe HBTs are

considered for the up-gradation of front end readout electronics of ATLAS detector in LHC, CERN, Geneva, Switzerland. Therefore in order to assess the tolerance of radiation, 50 GHz SiGe HBTs were irradiated with 50 MeV  $\text{Li}^{3+}$  ions with the total dose ranging from 600 krad to 100 Mrad. The various I-V characteristics of SiGe HBTs were studied before and after ion irradiation using computer interfaced Agilent 4155 Semiconductor Parameter Analyzer. Different emitter area devices were considered for the irradiation studies and results of the device with emitter area  $0.5 \times 2.5 \mu\text{m}^2$  are shown for brevity. Figure 1 illustrates the forward mode Gummel characteristics of  $\text{Li}^{3+}$  ion irradiated SiGe HBTs. The forward mode base current ( $I_B$ ) of the ion irradiated SiGe HBTs increases at lower  $V_{BE}$  with increasing  $\text{Li}^{3+}$  ion total dose. The degradation in  $I_B$  is the result of increased generation of generation-recombination (G/R) traps in the emitter-base (EB) spacer oxide. These radiation induced G/R traps increase recombination current in EB diode increase the  $I_B$ . The inverse mode Gummel characteristics of SiGe HBTs irradiated with 50 MeV  $\text{Li}^{3+}$  ions is shown in Figure 2. Radiation induced traps in Collector-Base (CB) space charge region were verified by inverse-mode Gummel characteristics of the devices. In this case, the radiation induced traps in the CB junction now act as G/R centers in the inverse EB junction and can be easily identified after a total dose of 100 Mrad.

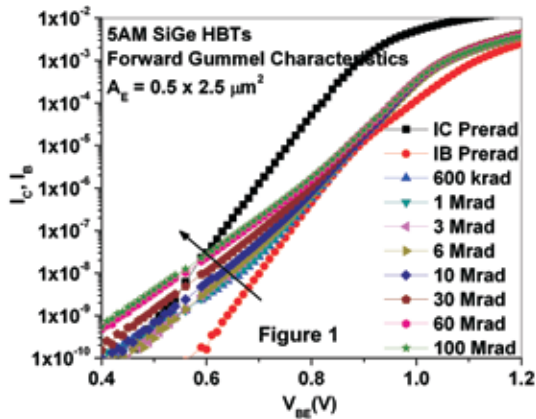


Fig. 1. Forward mode Gummel characteristics

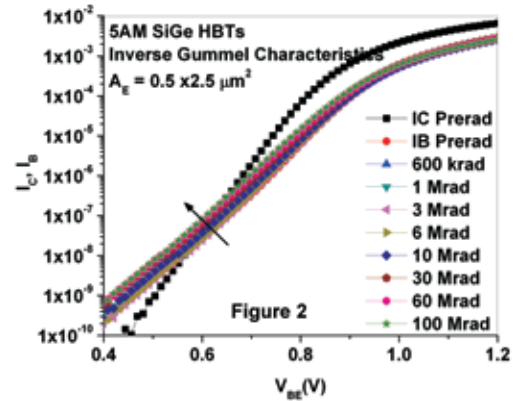


Fig.2. Inverse mode Gummel characteristics

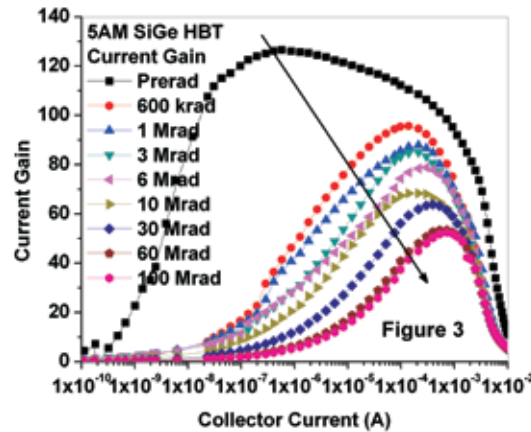


Fig. 3. Current gain

Figure 3 shows the degradation in forward mode current gain ( $\beta$ ) with increasing  $\text{Li}^{3+}$  ion total doses. Since  $I_B$  increases after irradiation and  $I_C$  is almost constant, hence  $\beta$  decreases with increase in ion dose. We have also studied the neutral base recombination (NBR) and avalanche multiplication (M-1) of carriers in CB junction after  $\text{Li}^{3+}$  ion irradiation. From the NBR studies we could conclude that very displacement was observed in SiGe HBT base region even after 100 Mrad of total dose. Avalanche multiplication of carrier's show that a few displacement damages created have decreased the impact ionization with lattice atoms. It is reported that the current gain of about 50 is required for the efficient circuit design of bipolar front-end readout for silicon detectors. Hence the 50 GHz SiGe HBTs are eligible for electronics used in intense radiation environments.

## REFERENCE

- [1] K.C. Praveen, N. Pushpa, Y.P. Prabhakara Rao, G. Govindaraj, J.D. Cressler, A.P. Gnana Prakash, *Solid State Electronics*, 54, 1554 (2010).

### 5.2.37 Performance of Photoanode in CdSe-sensitized solar cells with nitrogen implanted $\text{TiO}_2$ mesoporous electrodes

P. Sudhagar<sup>1</sup>, K.Asokan<sup>2</sup> and Yong Soo Kang<sup>1</sup>

<sup>1</sup>Center for Next Generation Dye-sensitized Solar Cells, WCU Program Department of Energy Engineering, Hanyang University, Seoul 133-791, South Korea

<sup>2</sup>Inter-University Accelerator Centre, Aruna Asaf Ali Marg, New Delhi

Major advancements have been made in  $\text{TiO}_2$  based semiconductor sensitized solar cells (SSC) in terms of developing compatible electrolytes, novel anode morphologies, fixing suitable counter electrodes and fusing with co-sensitizers. The oxygen deficient centers in anatase  $\text{TiO}_2$  photoanode is one of the major issues wherein the oxygen deficiency could create electron-hole pairs. The oxidizing holes can react with the quantum dots (QDs) or be scavenged by electrolyte. Those deficiencies result in shortening of the lifetime of the SSCs, and doping nitrogen into the  $\text{TiO}_2$  crystal structure may possibly reduce the oxygen deficiency and improve optical properties. Hence, nitrogen doped  $\text{TiO}_2$  are investigated for photovoltaic and photocatalytic applications since it can retard charge recombination by occupying oxygen vacancies. In this report, we describe the photoanode performance of 100 keV N ion implanted  $\text{TiO}_2$  electrodes.

Mesoporous  $\text{TiO}_2$  layer was prepared on fluorinated tin oxide (FTO) substrates by electrostatic spray technique and uniformly implanted by 100 keV N ions of fluences in the range of  $1 \times 10^{16}$  ions  $\text{cm}^{-2}$ . Figure 1(a) shows the response of visible-light on  $\text{TiO}_2$  and exhibit the fundamental absorption edge at 380nm. This is extended to 400-500nm in N ion implanted  $\text{TiO}_2$ . Such optical response in visible-light is attributed to N ions to band

splitting in  $\text{TiO}_2$  where  $\text{TiO}_2$  absorbs only 5% of the solar spectrum under visible wavelength range, due their wide band gap (3.2eV). This limitation was overcome by band splitting phenomena through N ion implantation. In Fig. 1(b), incident photon to current conversion (IPCE) tendency clearly reveal that the CdSe SSCs show high external quantum efficiency ( $\sim 35\%$ ) comprise with N-ion implanted  $\text{TiO}_2$  photoanode than that of pristine  $\text{TiO}_2$  device ( $\sim 14\%$ ). Under similar QDs loading environment, N- $\text{TiO}_2$  anode results higher conversion efficiency may explain the efficient charge injection at  $\text{TiO}_2/\text{CdSe}$  interface by retarding charge recombination.

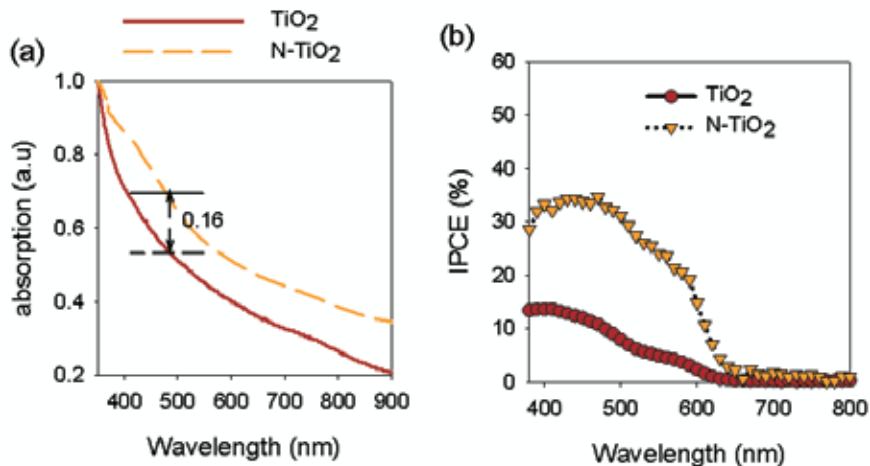


**Fig.1. (a) optical absorption spectra of pristine and N-implanted  $\text{TiO}_2$  mesoporous electrodes and ; (b) IPCE spectra of CdSe-sensitized solar cells using pristine and N-implanted  $\text{TiO}_2$  mesoporous photoanodes.**

CdSe quantum dots were directly assembled on resultant N implanted  $\text{TiO}_2$  photoanodes by chemical bath deposition and their photovoltaic performance was tested under polysulfide electrolyte with Pt counter electrode.

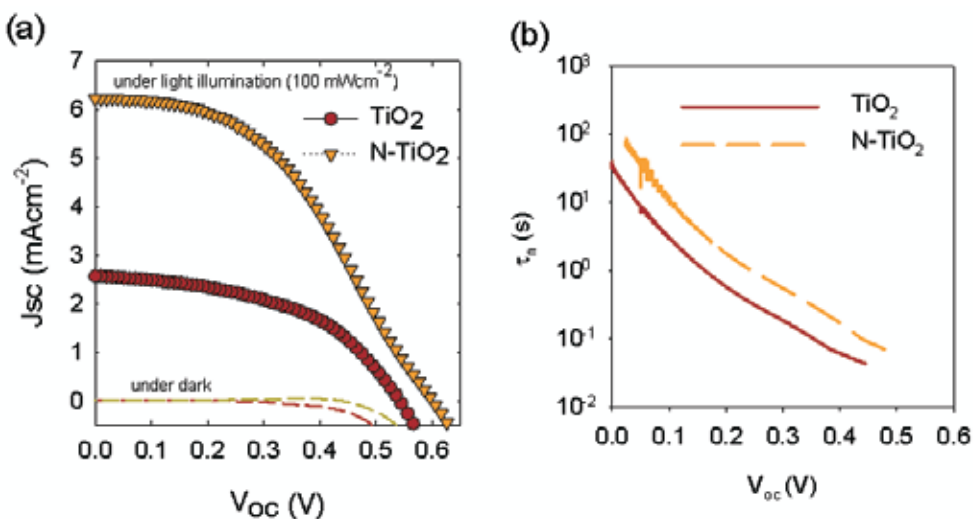


**Fig. 2. (a) JV measurements and; (b) open-circuit voltage decay measurement plots of CdSe-sensitized solar cells using pristine and N-implanted  $\text{TiO}_2$  mesoporous photoanodes.**

The photovoltaic parameters of pristine and N ion implanted  $\text{TiO}_2$  electrodes were studied and shown in Fig. 2(a). As evident from the figure, the nitrogen implanted  $\text{TiO}_2$  photoanodes show significant improvement in photoconversion efficiency,  $\eta=1.64\%$  compared to the pristine  $\text{TiO}_2$  photoelectrode ( $\eta=0.67\%$ ). Fig. 2(b) show the life time of electron at pristine and N ion implanted  $\text{TiO}_2$  QD-SSCs estimated from photovoltage decay measurements. This clearly reveals that life time of the electrons were apparently improved by N ion implantation, due to N-ions occupying oxygen vacancies of  $\text{TiO}_2$  resulting in retardation of the charge recombination centers.

### 5.3 RADIATION BIOLOGY

Works with cancer cells like HeLa, CHAGO and A549 have been started and in order to provide exposure to research scholars to real life experiments, initial cell survival studies using gamma ray and C and O beam has been carried out.

Works have been initiated to study the interaction of gold nano particles with HeLa cells using SEM, TEM and Surface Enhanced Raman spectroscopy. Substantial amount of work has been done to study the interaction of gamma ray with gold nano particle treated HeLa cells.

University projects from MMC College Ghaziabad and Kalyani University to study high LET radiation action on cancer cells are continuing. Efforts on BARC-IUAC collaboration have been initiated.

#### 5.3.1 RBE evaluation in Human cervical cancer cell line exposed to Gamma radiation and Carbon Beam (LET 290 KeV/ $\mu\text{m}$ )

Harminder Kaur, Geetanjali Pujari, A. Sarma

An attempt has been made to study the survival fraction of Human cervical cancer cell line HeLa, as a function of dose, irradiated with two different quality of radiation. The objective of the experiment is to evaluate Relative Biological Effectiveness (RBE) to determine and compare the effect on cell killing by two different radiations.

HeLa cells were procured from National Centre for Cell Science (NCCS), Pune. The cells were grown in Dulbecco's Modified Eagles Medium (DMEM) supplemented with 10% Foetal Bovine Serum (FBS) and 1% antibiotic Penicillin Streptomycin.

Confluent cells were exposed to Gamma Radiation and carbon beam (LET 290 KeV/ $\mu\text{m}$ ). The  $\gamma$ -irradiation was carried out at Army Referral Hospital, New Delhi using Theratron 1000E Telecobalt machine. For carbon ion irradiation of cells, ASPIRE system at BIO Beam line was used. The ion energy incident on cell surface was calculated to be 62 MeV by TRIM. The Linear Energy Transfer (LET) is determined to be 290 keV/ $\mu\text{m}$ .

Clonogenic Survival assay: In order to study the survivability of irradiated cells, soon after irradiation, the cells were trypsinized and reseeded at definite numbers in culture flasks. Colonies were allowed to form with 10-12 days of incubation. Colonies were stained with 0.25% of methylene blue. Visible colonies were counted with a criterion that colony must have at least 50 cells. The survival fraction was determined by dividing the number of colonies in the irradiated cells to that of the control cells.

The dose used for  $\gamma$ -irradiation and carbon ion is shown in Table below. The respective survival fraction of HeLa cells with dose is also tabulated (Table 1).

**Table 1**

Gamma Dose [Gy]	Survival Fraction	Particle Dose [Gy]	Survival Fraction
0	1	0	0.99
1	0.76	0.93	0.66
2.5	0.41	2.78	0.21
5	0.09	4.64	0.51
7.5	0.02	5.57	0.27
		6.5	0.02
		7.42	0.01
		8.35	0.044

The result shows that there is significant reduction in survival fraction of carbon beam exposed HeLa cells to that of Gamma irradiated cells. The experimental survival fraction  $[S/S_0]$  data points are fitted with Linear Quadratic dose  $[D]$  dependent relation given by  $S/S_0 = \exp -[\alpha D + \beta D^2]$  (Figure 1).

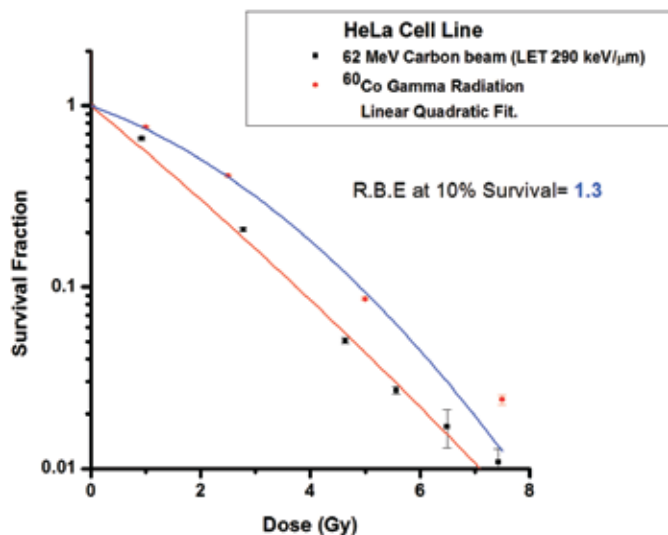


**Fig. 1. Fitted curve of Survival Fraction of HeLa cells exposed to Gamma Radiation and Carbon beam (LET 290 keV/μm)**

It is seen from the graph that to achieve 90% cell killing by Gamma radiation, the dose required is 4.9 Gy. Whereas, 90% cell killing is achieved by 3.8 Gy of carbon beam (LET 290 KeV/m). Relative Biological Effectiveness (RBE) is determined by ratio of dose required by gamma radiation for 90% cell killing and dose required by carbon beam for 90% cell killing. RBE is calculated to be 1.3.

### 5.3.2 Study of Radiosensitivity of Human Cervical Cancer cell line on treatment with Glucose stabilized Gold Nanoparticle

Harminder Kaur, Geetanjali Pujari, A. Sarma and D.K. Avasthi

In the present study, we show the enhancement of  $\gamma$ -radiation (from  $^{60}\text{Co}$ ) effect on Human cervical cancer cell line, HeLa, which are pre-treated with Glucose stabilized Gold nanoparticle (Glu-AuNP). It is seen that  $\gamma$ -radiation of Glu-AuNP treated HeLa cells lead to a steeper survival curve as compared to that of irradiation of untreated cells. The result suggests an enhancement of radio-sensitization.

The Glu-AuNP were synthesized by the method proposed by Liu et al 2006, using  $\text{HAuCl}_4 \cdot 3\text{H}_2\text{O}$  (from Sigma) as the gold particle source and  $\gamma$ -D-Glucose (S,D-fine Chem.) as reducing agent. The synthesized Glu-AuNP was characterized by UV-Vis Spectroscopy and Transmission Electron Microscopy (TEM). The cross sectional TEM of Glu-Au NP treated cancer cell and the TEM of Glu-AuNP were performed using JEOL 2100 F at Advance Instrumentation Research Facility (AIRF), Jawaharlal Nehru University, New Delhi (Figure 3, 4).

The absorbance at 540 nm in UV-vis spectrum shown in figure 1, is characteristic surface plasmon resonance of Au nanoparticles, providing an evidence of Au nanoparticles. The TEM image of the Glu-AuNP is shown in Figure 2. Energy-dispersive X-ray spectroscopy (EDX) was performed to confirm the existence of Au.

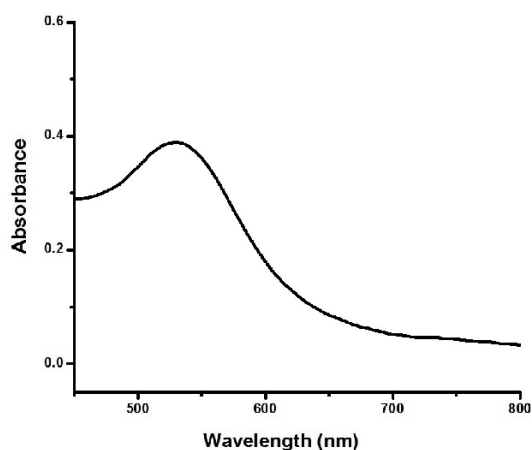


**Fig. 1. UV-Vis spectrum showing SPR at 540 nm**

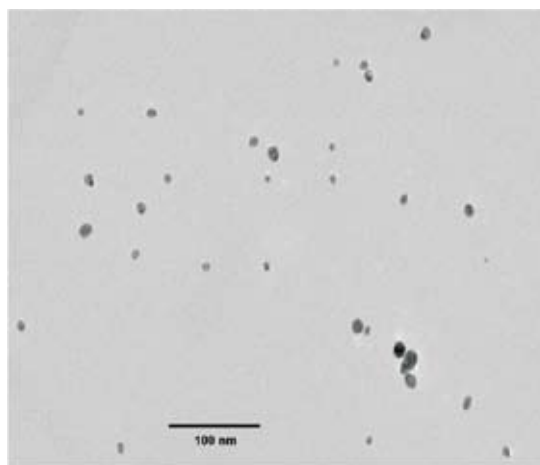


**Fig. 2. TEM image of Glu-AuNP**

The TEM image of fixed cell is shown in Figures 3 and 4. The AuNP are clearly seen in the image of HeLa cancer cell.

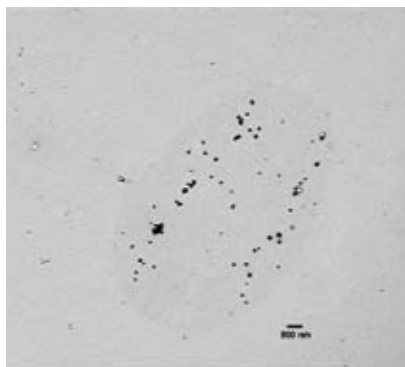


**Fig. 3. TEM of whole cell incubated with Glu-AuNP**

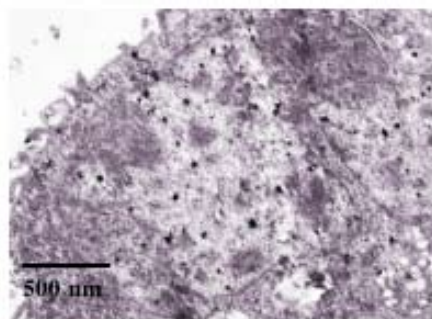


**Fig. 4. TEM of ultrathin cross section of HeLa cells incubated with Glu-AuNP**

The clonogenic assays were performed to study the effect of  $\gamma$ -radiation of HeLa cells with and without treatment of Glu-AuNP treatment. The cells were treated with Glu-AuNP with concentrations of  $5.7 \times 10^{10}/\text{ml}$  and  $1.1 \times 10^{11}/\text{ml}$  and each is incubated for 3 h and 6 h respectively. After incubation, the medium was decanted in order to discard the unabsorbed Glu-AuNP. These were then subjected to  $\gamma$ -radiation at Dose rate of 0.5 Gy/min with doses of 1, 2.5, 5 and 7.5 Gy. The cells after treatment were incubated for 10-12 days to form colonies.

Results of colony forming assay of  $\gamma$ -irradiated HeLa cells with Glu-AuNP pretreatment in form of a survival curve are shown in Figure 5. The experimental survival fraction  $[S/S_0]$  data points were fitted with Linear Quadratic dose  $[D]$  dependent relation given by  $S/S_0 = \exp -[\alpha D + \beta D^2]$ , where  $\alpha$  and  $\beta$  are constant. We observe that there is a significant decrease in survival fraction on combined treatment of Glu-AuNP and  $\gamma$ -radiation in comparison to the cells exposed to only  $\gamma$ -radiation.

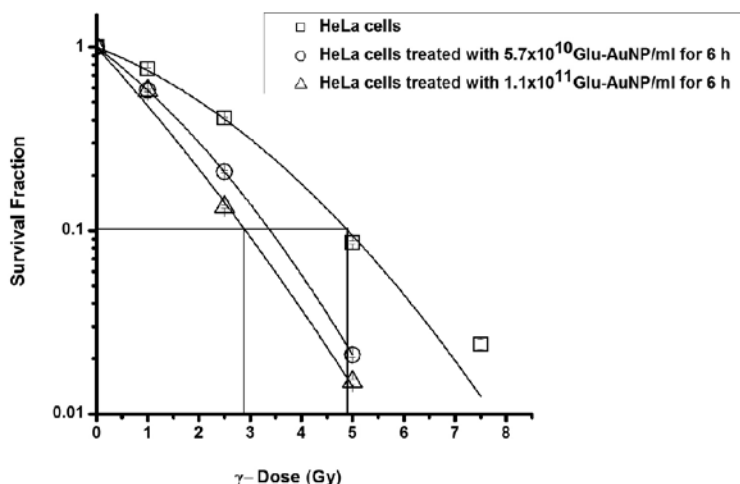


**Fig. 5. Fitted curve of Survival Fraction of HeLa cells and the  $\gamma$ -irradiated HeLa cells pretreated with Glu-AuNP**

The  $\gamma$ -irradiation of Glu-AuNP treated HeLa cancer cells result in significantly enhanced effect of irradiation in term of cell killing as compared to those of without Glu-AuNP treatment. Thus by carrying the AuNP to cancer cells, the tumour cell killing efficiency during radiation therapy can be enhanced.

### 5.3.3 Surface Enhanced Raman Spectroscopy (SERS) Study of Human Cervical Cancer and Lung Cancer Cell Line

Geetanjali Pujari, Harminder Kaur, D.K. Avasthi and A. Sarma

Raman microscopy is a well-established technique that provides information on the vibrational frequencies of molecules. We confirm the attachment of AuNP with cancer cells by carrying out Raman spectroscopy. Gold nanoparticle (AuNP) is synthesized by Tri Sodium Citrate method. The synthesis process consisted of reduction of boiling 0.01% solution of Tetrachloroauric acid with 1% solution of tri sodium citrate with constant stirring while heating till the color of gold solution changes from yellow to deep wine red.

Charaterization of the nanoparticles have been done by UV-Vis spectroscopy (Fig 1) and Transmission Electron Microscopy (Fig 2). The size of AuNP is determined to be 20 nm.

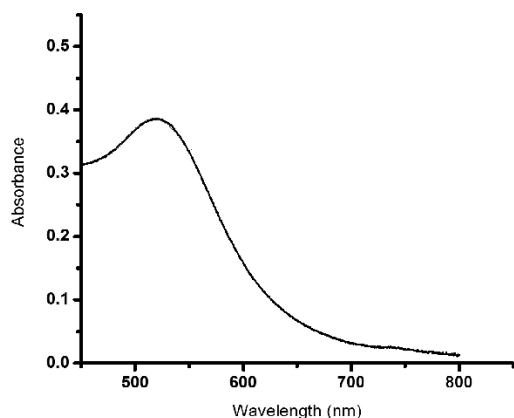


**Fig. 1. UV-Vis absorbance spectra of AuNP**

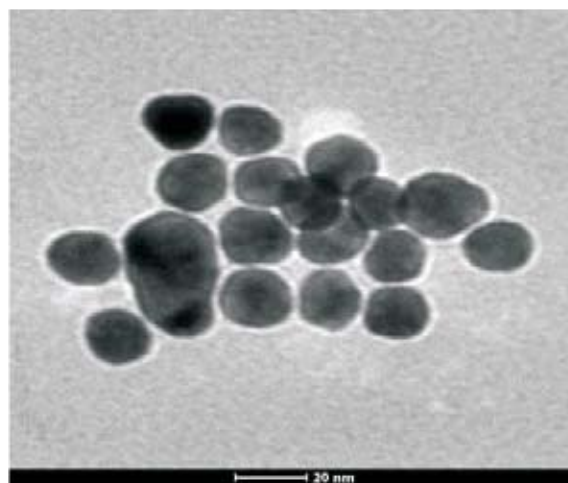


**Fig. 2. TEM image of AuNP**

Human cervical cancer cell line, HeLa, and lung cancer cell line, A549, are routinely cultured in Dulbecco's modified eagles medium (DMEM) and 10% serum. The cultured cells are incubated with synthesized AuNP for 24 hrs. In order to study the attachment of AuNP with the cells, Scanning Electron Microscopy was carried out (Fig 3 and 4).

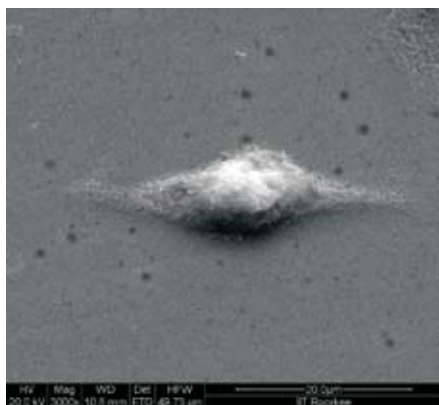


**Fig. 3. SEM of HeLa cell after incubation with AuNP for 24 hrs**



**Fig. 4. SEM of A549 cell after incubation with AuNP for 24 hrs**

In order to confirm the attachment of AuNP with the cancer cell lines, Raman spectroscopy is done (Renishaw Raman Microscope from IUAC). The cells after incubation with AuNP for 24 hrs were fixed with aceto-methanol. Raman spectroscopy of the fixed cells was carried out. We could observe a strong enhancement of Raman mode in cells treated with AuNP when compared with untreated cells (Figure 5 and 6). Interesting observation is that the enhancement in the Raman signature was more in the nucleus region as compared to the cytoplasm.

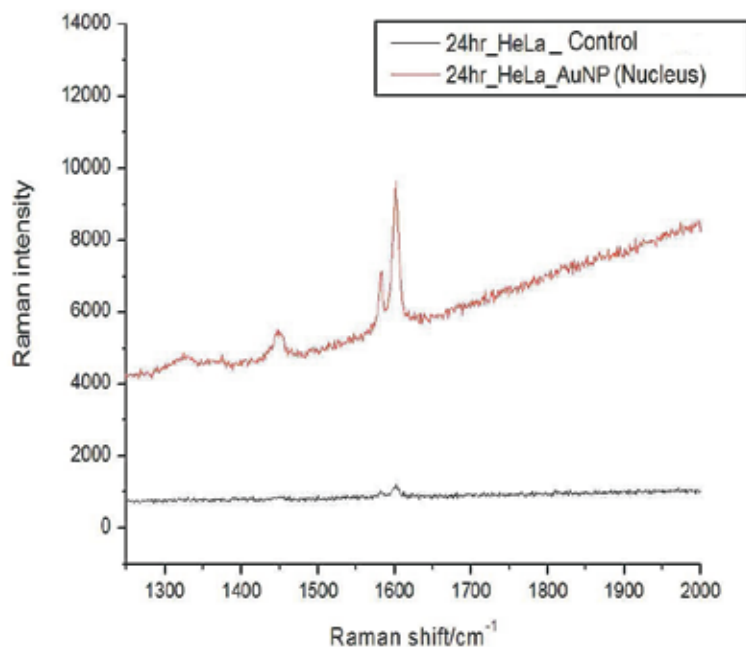


**Fig. 5. SERS of HeLa cells on incubation with AuNP for 24 hours**

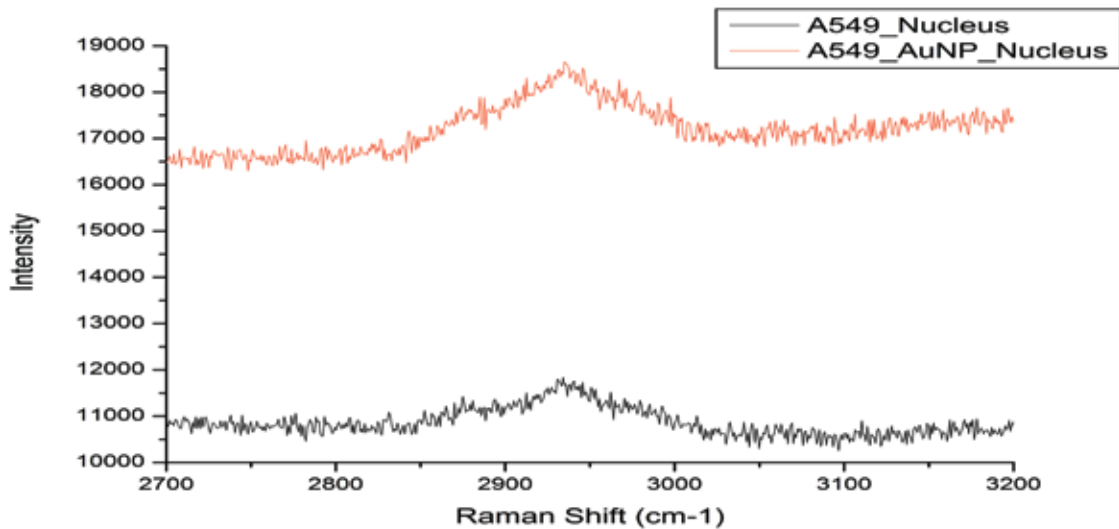


**Fig. 6. SERS of A549 cells on incubation with AuNP for 24 hours**

Work on enhanced Raman signal from cancer cell lines due to the presence of noble nanoparticle will provide information on mechanistic behaviour of cellular uptake of nanoparticle. Such studies are also important for providing information about the use of gold nanoparticles for early detection of cancer by SERS.

## 5.4 ATOMIC PHYSICS

Effort is continued to understand better the unusual features observed in the beam-foil spectra. In recent past we observed x-ray spectra from projectile like ions produced in nuclear reaction. This month we performed an experiment along this line. This time we took an attempt to prove that the nuclear products are originally fully stripped ions. Besides this innovative experiment, we carried out investigations on inner shell ionization by heavy ion impact also.

Atomic and molecular physics experiments in the low energy ion beam laboratory have been yielding interesting results as in previous years. Position sensitive multi-hit time-of-flight measurement system is used to study the fragmentation dynamics of complete and incomplete fragmentation process at high velocities (presented below).

### 5.4.1 Formation of fully stripped ions in multi-nucleon transfer reaction and the study of the reaction $^{56}\text{Fe}, ^{58}\text{Ni} (^{12}\text{C}, \alpha\alpha)$

T. Nandi<sup>1</sup>, Akhil Jhingan<sup>1</sup>, B.J.Roy<sup>2</sup>, V. Jha<sup>2</sup>, D.C. Biswas<sup>2</sup>, R.K.Choudhury<sup>2</sup>, Biraja Mohanty<sup>3</sup>, Mumtaz Oswal<sup>3</sup>, Sunil Kumar<sup>3</sup>, V. Singh<sup>3</sup>

<sup>1</sup>Inter-University Accelerator Centre, Aruna Asaf Ali Marg, New Delhi

<sup>2</sup>Nuclear Physics Division, Bhabha Atomic Research Centre, Mumbai

<sup>3</sup>Department of Physics, Panjab University, Chandigarh

In an recent work [1] the atomic physics group of IUAC has shown that the projectile like ions are most likely formed in the fully stripped charged state. Also in an another study [2] we got hint that the ions do capture up to circular Rydberg states while passing through the target. Surprisingly in these studies Rydberg states were observed only with the H-like ions. It can be noted here that no Rydberg states can survive while the ions passing a solid matrix indicating that they can only be formed at the exit surface [1,2]. This requires that the starting ion must be a fully stripped ion. In order to have a further understanding on this and to confirm our previous observation that the fully stripped ions are indeed formed in the nuclear reactions, we have carried out very recently several measurements at UAC, Delhi using the general purpose scattering chamber GPSC.

$^{12}\text{C}$  beams of energies in the range of 45-70 MeV were bombarded on enriched target of  $^{56}\text{Fe}$  and  $^{58}\text{Ni}$ . The nuclear reaction products were detected using silicon surface barrier detectors in  $\Delta E$ -E telescope configuration while X-ray spectra from the atomic transitions were recorded by suitable HpGe detector. As is seen in a typical X-ray spectrum (Fig. 1a), one can see that the iron  $K_a$  and  $K_b$  lines appeared due to the vacancy creations by ion impact. Most remarkably however the x-ray lines observed due to target like nuclear products such as Ni and Ga originated from Ly- $\alpha$  and Ly- $\beta$  structure. It clearly implies that primarily nuclear

reaction gives rise to fully stripped ions and the electron capture events later lead to x-ray emissions from the H-like ions. It was observed that the targets contain small amount of impurities W and In and the X-ray spectrum from these impurities smears out the region of x-ray lines of present interest. In order to overcome this problem we also have collected data in the inverse kinematic condition i.e., 175 MeV  $^{58}\text{Ni}$  bombarding on carbon target and a typical X-ray spectrum obtain from such experiment is shown in Fig.1b. This spectrum displays x-ray lines from H- and He-like Zn and As ions corresponds to alpha-transfer reaction and p-evaporation reaction, respectively. Present data clearly hint the formation of fully stripped ions via nuclear reactions and we believe that such type of experiment may have long term interest in atomic physics.

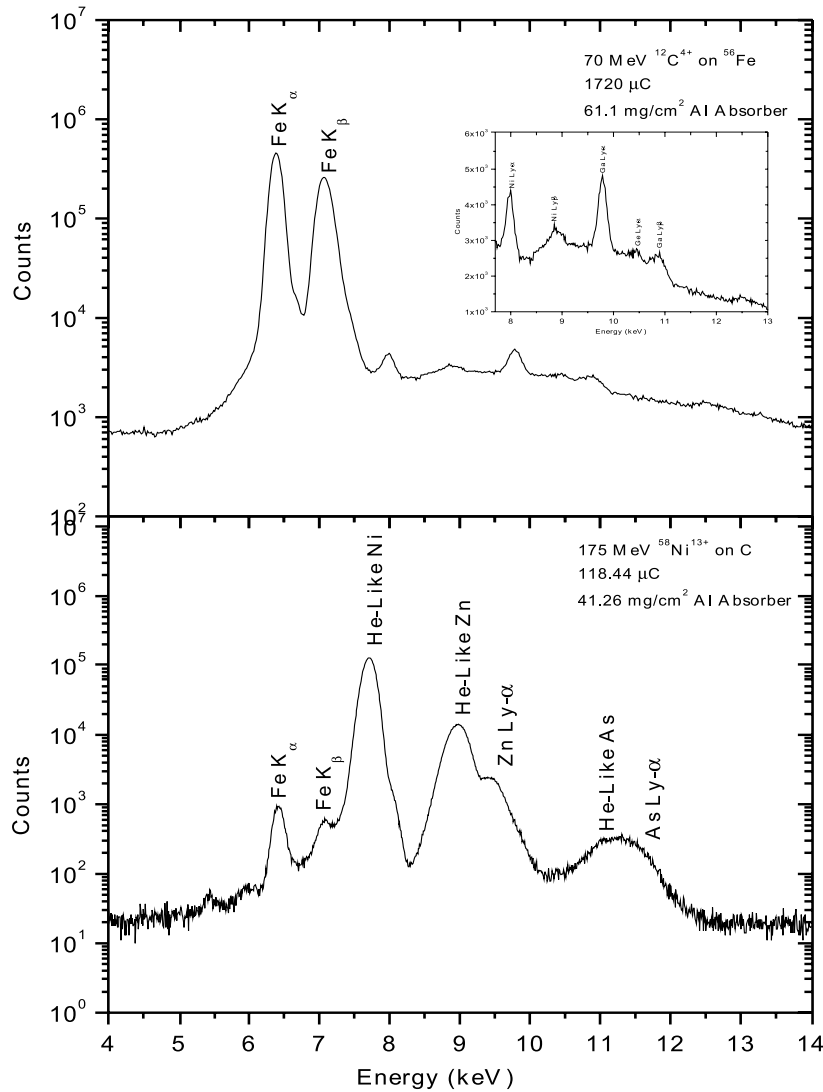


**Fig1. X-ray spectrum obtained with a Canberra GUL 0055 detector and an Al absorber in the front (a) for 60 MeV  $^{12}\text{C}$  beam on  $^{56}\text{Fe}$  target and (b) 175 MeV  $^{58}\text{Ni}$  beam on the natural carbon target. Fe X-rays are due to impurities in carbon target.**

The other aim of the experiment was to measure the coincidence reaction ( $^{12}\text{C}, \alpha\alpha$ ). Multi-nucleon transfer between heavy ions represents an important reaction mechanism to understand correlation among nucleons. Our earlier study of multi-nucleon transfer reaction ( $^{18}\text{O}, \text{X}$ ) indicates a large enhancement of two neutron and two neutron correlated transfer [3, 4]. Such transfer reactions leading to specific states of residual nuclei and a detailed coupled reaction channel analysis in terms of microscopic form factors for two neutrons transfer will allow us to gain information on the two neutron correlations and to understand detailed reaction mechanism aspects. This may be interesting in view of large transfer cross sections measured for reactions involving the radioactive nuclei such as  $^6\text{He}, ^8\text{He}$  etc. In addition, the four nucleon transfer reaction ( $^{12}\text{C}, ^8\text{Be}$ ) is not so well studied due to the complexity involved in detection of the unstable  $^8\text{Be}$  nucleus which decays into two alphas. On the other hand, cross section for this channel is expected to be large (as compared to the single and/or two nucleon transfer reactions) due to Q-value effect. The reaction mechanism is interesting in order to understand the role of one step alpha transfer vis-à-vis multi step sequential transfer. In our earlier study on  $^{12}\text{C} + ^{56}\text{Fe}$  system at 60 MeV [5] and a detailed Coupled Reaction Channel calculation indicate a significant contribution from multi-step sequential process for the two and three nucleon stripping reactions. In the present experiment at IUAC, Delhi we have measured coincidence between the two alphas originating from  $^8\text{Be}$  decay using two ( $\Delta\text{E}$ -E) Telescope detectors and a silicon pad detector. A very good charge and mass separation has been achieved for projectile like products and a typical  $\alpha$ - $\alpha$  coincidence spectrum (online TAC spectrum) is shown in Fig.2. Detailed analysis is in progress.

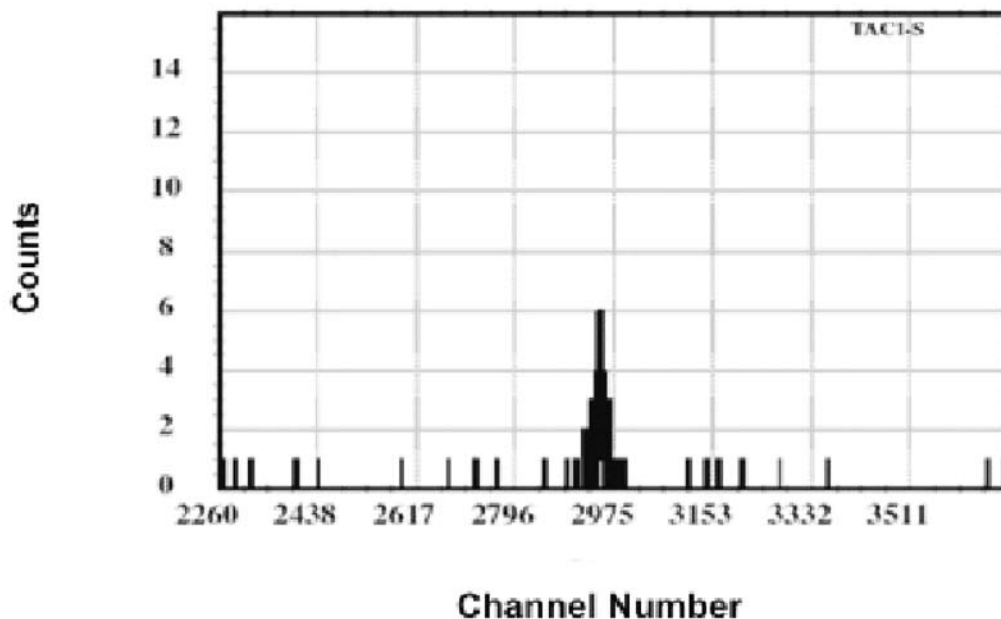


**Fig. 2. A typical  $\alpha$ - $\alpha$  coincidence spectrum obtained in a geometry where the two detector telescopes were placed at 6 deg. apart and the reaction used was 60 MeV  $^{12}\text{C}$  beams on  $^{58}\text{Ni}$  target.**

## REFERENCES

- [1] T. Nandi, J. Phys. B 42 (2009) 125201.
- [2] T. Nandi, Astro. Phys. J. Lett 673 (2008) L103.
- [3] V. Jha et al., *Eur. Phys. J. A19* (2004) 347.
- [4] V. Jha et al., *Eur. Phys. J. A* 15 (2002) 389.
- [5] Hari S Patel et al., *Pramana J. Physics.* 53 (1999) 843.

### 5.4.2 L x-ray production cross sections for high-Z elements by $F^{+6,7,8}$ ions

S. Kumar<sup>1</sup>, M. Oswal<sup>1</sup>, G. Singh<sup>1</sup>, S.C. Bedi<sup>1</sup>, N. Singh<sup>1</sup>, D. Mehta<sup>1</sup>, G. Lapicki<sup>2</sup>, A. Jhingan<sup>3</sup> and T. Nandi<sup>3</sup>

<sup>1</sup>Department of Physics, Panjab University, Chandigarh

<sup>2</sup>Department of Physics, East Carolina University, Greenville, North Carolina, USA.

<sup>3</sup>Inter-University Accelerator Centre, New Delhi

The inner-shell ionization by charged particles is an important field of the ion-atom collisions [1]. The possible mechanism of vacancy production in the target atom is the direct ionization (DI) and electron capture (EC) processes. Many theoretical efforts, namely, the Plane Wave Born Approximation (PWBA) [2], Binary Encounter Approximation (BEA) [3], Oppenheimer-Brinkman-Kramer (OBK) formulas of Nikolaev [4], First Born Approximation (FBA) [5], ECPSSR theory [6] have been mainly focused on description of the ion-atom collisions. The experimentally measured cross sections are found to deviate from the theoretical ones due to increase in target inner shell binding energies and also due to the multiple ionization of the target inner shell by heavy ions.

The increase in the binding energies of the target electrons changes due to the presence of the projectile and this effect was included in the ECUSAR [7] theory. Also, the heavy ions create multiple vacancies in the target atom due to simultaneous ejection of electrons. The multiple ionization effect reduces Coster-Kronig transitions and enhances the fluorescence yield. Therefore, the L x-ray production cross sections for high-Z elements by  $^{19}\text{F}$ -ion have been studied for the deeper understanding of the ion-atom interaction processes.

The experiment was performed using  $^{19}\text{F}$  ion beams (Energy = 76-114 MeV) from the 15 UD Pelletron accelerator at Inter-University Accelerator Center (IUAC), New Delhi. The elemental targets of the  $_{78}\text{Pt}$ ,  $_{79}\text{Au}$ ,  $_{82}\text{Pb}$  and  $_{83}\text{Bi}$  (thickness  $\sim 120 \mu\text{g}/\text{cm}^2$ ) elements were prepared on the  $20 \mu\text{g}/\text{cm}^2$  carbon backing using vacuum deposition technique. The  $^{19}\text{F}$  beam of different charge states ( $q = +6, +7, +8$ ) has been focussed on the target. The

L x-ray emitted from the elemental targets were detected using Si(Li) detector (thickness = 5 mm, diameter = 10 mm, 25  $\mu\text{m}$  Be window, Ortec US) placed outside the vacuum chamber at an angle of 125° to the beam direction. The data was acquired using PC based CANDLE software specially developed for the data acquisition and analysis at IUAC, New Delhi. In the present measurements the peak areas were evaluated using the computer program CANDLE.

The present measured cross sections are compared with those calculated using  $L_i$  subshell ionization cross sections based on different theories, viz., FBA, ECPSSR and ECUSAR. The fluorescence and Coster-Krpnig (CK) yields, [8], were corrected for

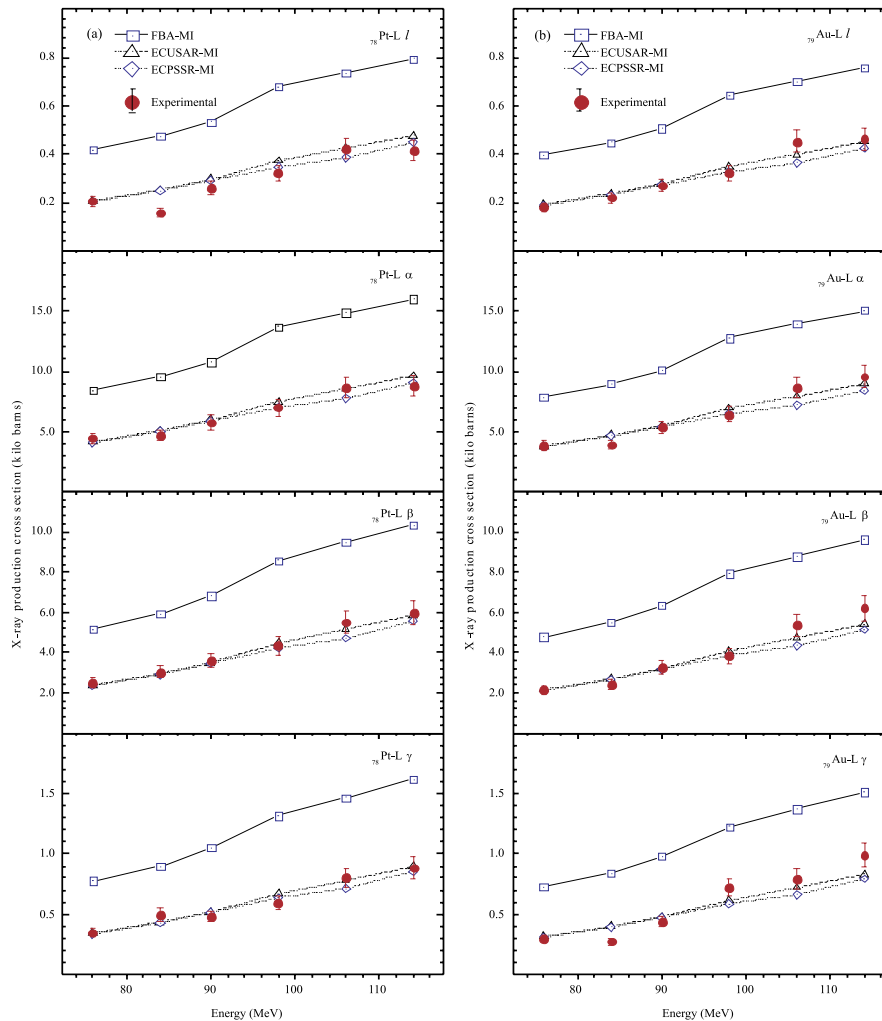


**Fig. 1.** The deduced values for the  $L_i$ ,  $L\alpha$ ,  $L\beta$  and  $L\gamma$  x-ray production cross section for (a)  $^{78}\text{Pt}$  target and (b)  $^{79}\text{Au}$  target, as a function of the beam energy. The different symbols shows the cross sections obtained from ECUSAR, ECPSSR and FBA models along with the experimental results. The circular files symbols are the experimental results along with the error bars.

multiple ionization using a simplified model prescribed by Lapicki *et al.* [9]. For the same projectile energy, the primary  $L_i$  ( $i = 1-3$ ) subshell ionization cross sections are calculated to be higher by  $\sim 10\%$  for the  $8^+$  charge state due to electron capture as compared to the  $7^+$  charge state. The deduced values for the  $L$  x-ray production cross section for (a)  $_{78}\text{Pt}$  target and (b)  $_{79}\text{Au}$  target, as a function of the beam energy is plotted in Fig 1. The measured values were found to obey the ECUSAR and ECPSSR theories and were about 2 times lower than FBA. Preliminary results reflect that at all the incident beam energies, multiple ionization reduced the CK yields, and enhanced the  $L_3$  subshell fluorescence yields compared to the  $L_1$  and  $L_2$  subshell fluorescence yields. Furthermore, the applications of heavy ions are not fully developed to date, possibly due to the inaccuracies found in the understanding of the basic processes and the possible damage to samples. The use of heavy ions in PIXE applications provides better sensitivity than the usual arrangement of protons with 2-3 MeV energies. Further, critical evaluation of the present data is in progress.

## REFERENCES

- [1] Atomic Inner Shell Processes, edited by B. Craseman (Academic Press, New York, 1978).
- [2] E. Merzbacher, H.W. Lewis, *Handbuch der Physik*, edited by S. Flugge (Springer, Berlin, 1958), Vol. 34, p. 166; R. Rice, G. Basbas, F. D. McDaniel, *At. Data Nucl. Data Tables* 20 (1977) 503.
- [3] J. D. Garcia, *Phys. Rev. A* 1 (1970) 280; J. S. Hansen, *ibid.* 8 (1973) 822.
- [4] V.S. Nikolaev, *Zh. Eksp. Teor. Fiz.* 51 (1966) 1263; [*Sov. Phys. JETP* 24 (1967) 847].
- [5] B.-H. Choi, E. Merzbacher, G.S. Khandelwal, *At. Data* 5 (1973) 291.
- [6] W. Brandt, G. Lapicki, *Phys. Rev. A* 23 (1981) 1717.
- [7] G. Lapicki, *Nucl. Instrum. Meth. B* 189 (2002) 8.
- [8] J.L. Campbell, *At. Data Nucl. Data Tables* 85 (2003) 291; *At. Data Nucl. Data Tables* 95 (2009) 115.
- [9] G. Lapicki, R.Mehta, J.L. Duggan, P.M. Kocur, J.L. Price, F.D. McDaniel, *Phys. Rev. A* 34 (1986) 3813.

### 5.4.3 L sub-shell ionization for high Z elements by $\text{Si}^{+8,12}$ ions

M.Oswal<sup>1</sup>, S. Kumar<sup>1</sup>, G. Singh<sup>1</sup>, R. Kaur<sup>1</sup>, D. Mehta<sup>1</sup>, K.P Singh<sup>1</sup>, A. Jhingan<sup>2</sup> and T. Nandi<sup>2</sup>

<sup>1</sup>Department of Physics, Panjab University, Chandigarh

<sup>2</sup>Inter-University Accelerator Centre, New Delhi

Varieties of measurements of K and L x-ray production cross sections by incident ions have been carried out during the past two–three decades, most of the measurements are done by light ion impact. Results of K- and L-shell ionization cross-sections by protons and  $\alpha$ -particles show generally good agreement with the ECPSSR theory. Less frequent

measurements of *L*-sub shell cross-sections induced by heavy ions further expose deviations. Such deviations are traced to methods of extraction of ionization cross-sections from x-ray production measurements. These methods can give inconsistent results because fluorescence yields and other parameters required for extraction of ionization cross sections are strongly affected by the prevalence of multiple ionization by heavy ions [1-3]. So, K-shell and L sub shell ionization cross-sections for high *Z* elements have been studied using  $^{28}\text{Si}$  beam for deeper understanding.

Experiment was conducted at Atomic Physics Beam Line in Beam Hall II at Inter University Accelerator Centre (IUAC), New Delhi. Experimental setup is shown in figure 1.  $^{28}\text{Si}$  beam, energy ranging between 3-5 MeV/u was used. Elemental targets  $_{78}\text{Pt}$ ,  $_{79}\text{Au}$ ,  $_{82}\text{Pb}$  and  $_{83}\text{Bi}$  (thickness  $\sim 120 \mu\text{g}/\text{cm}^2$ ) were prepared on the  $20 \mu\text{g}/\text{cm}^2$  carbon backing using vacuum deposition technique at the target laboratory, IUAC. L x-rays emitted were detected using SiLi detector (thickness = 5 mm, diameter = 10 mm,  $25 \mu\text{m}$  Be window, Ortec USA) placed at an angle of  $125^\circ$  to the beam direction and HPGe detector (thickness = 5 mm, diameter = 10 mm,  $25 \mu\text{m}$  Be window, Canberra USA) at an angle of  $135^\circ$  to the beam direction. Data were acquired in the form of LIST mode using software CANDLE developed at IUAC, New Delhi. Some of the spectra are shown in the figure 2. Peak areas were also fitted using the same routine.

To determine detector efficiency, calibrated sources  $^{241}\text{Am}$ ,  $^{137}\text{Cs}$  and  $^{155}\text{Eu}$  have been used and to extrapolate the efficiency curve, XRF technique has been used. In that technique a point source of  $^{241}\text{Am}$  was used with some standard foils of  $_{26}\text{Fe}$ ,  $_{27}\text{Co}$ ,  $_{29}\text{Cu}$ ,  $_{30}\text{Zn}$ ,  $_{34}\text{Se}$ ,  $_{48}\text{Cd}$ ,  $_{50}\text{Sn}$ ,  $_{47}\text{Ag}$  and  $_{78}\text{Pt}$ . These foils were placed at the target ladder and source was at the position of beam. X-ray spectrum was obtained using both the detectors. Some of the spectra are shown in figure 3. Preliminary results in the form of intensity ratios have been already calculated

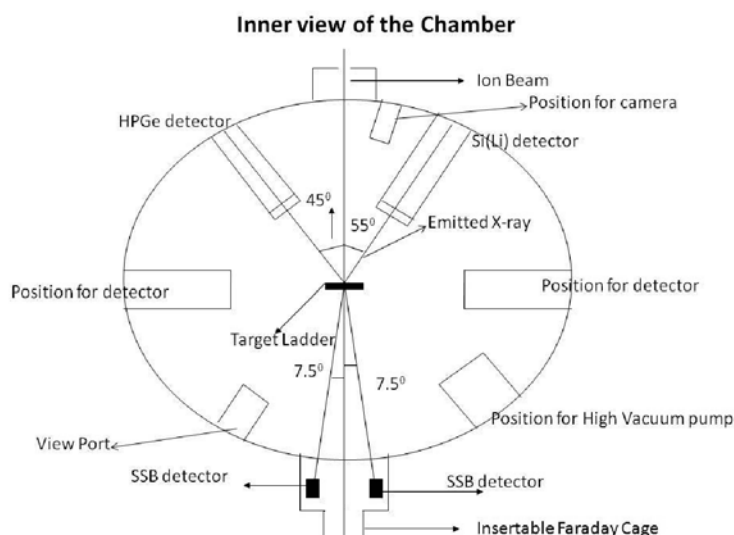


**Fig. 1. Experimental Setup at Atomic Physics Beam Line, Beam Hall II**

and cross- section calculations are in progress. After calculating experimental cross-sections, comparison will be done using different models like ECPSSR, FBA and ECUSAR [3].

## REFERENCES

- [1] P. Wang, J.J. MacFarlane and G.A. Moses. Laser and Particle Beams, 13,191(1995).
- [2] M. Pajek et al., Phys Rev A. 68, 022705 (2003).
- [3] G. Lapicki et al., Phys. Rev. A 70, 062718 (2004).

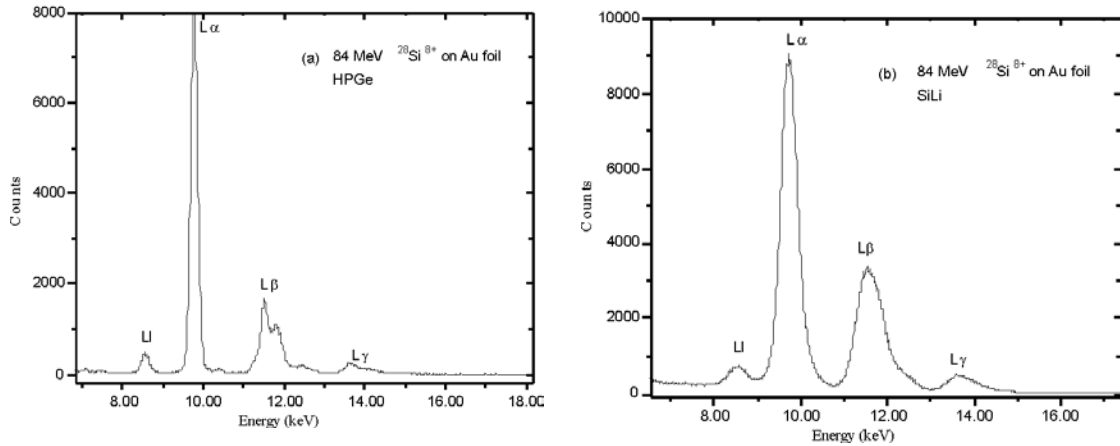


**Fig. 2. X-ray spectrum obtained from Au foil with  $^{28}\text{Si}$  beam of energy 84 MeV using (a) HPGe (b) SiLi detector.**

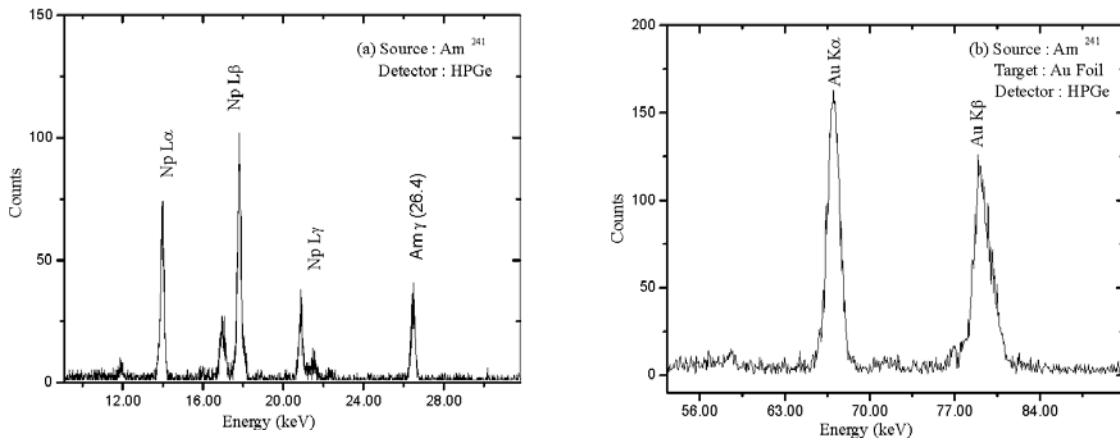


**Fig. 3. X-ray spectrum of (a) Am-241 Source from HPGe detector and (b) Au foil using Am-241 point source.**